This is to certify that the
dissertation entitled

STRAIN ANALYSIS AT THE HETEROINTERFACES OF III-V TERNARY ALLOYS:ULTRA-THIN GaAsP/GaAs SUPERLATTICES

presented by

WONJAE CHANG

has been accepted towards fulfillment
of the requirements for the

PH.D. degree in ELECTRICAL ENGINEERING

Terence Brown
Major Professor's Signature

8/24/2010
Date

MSU is an Affirmative Action/Equal Opportunity Employer

STRAIN ANALYSIS AT THE HETEROINTERFACES OF III-V TERNARY ALLOYS: ULTRA-THIN GaAsP/GaAs SUPERLATTICES

By

WONJAE CHANG

A DISSERTATION

Submitted to
Michigan State University
In partial fulfillment of the requirements
for the degree of

DOCTOR OF PHILOSOPHY

Electrical Engineering

2010

ABSTRACT

STRAIN ANALYSIS AT THE HETEROINTERFACES OF III-V TERNARY ALLOYS: ULTRA-THIN GaAsP/GaAs SUPERLATTICES

By

WONJAE CHANG

The principal objective of this research was to characterize heterointerfaces of III-V ternary alloys consisting of ultra-thin GaAsP/GaAs superlattices grown by Molecular Beam Epitaxial (MBE). The area of application for these materials is in optical devices, operating under the visible and IR spectrum. The characterization of heterointerfaces using high-resolution transmission electron microscopy (HRTEM) is divided into two parts: 1) Strain analysis using advanced methodologies known as phase techniques, and 2) Evaluation of chemical contrast, along with minimization of artifacts on HRTEM images, using the Composition Evaluation by Lattice Fringe Analysis (CELFA) method.

Phase techniques for stain analysis on HRTEM images can be divided into two types: Geometric Phase Analysis (GPA) and Computational Fourier Transform Moiré (CFTM) method. This research exploits the CFTM method and deals with demonstration of the Computational Fourier Transform Moiré (CFTM) method for strain analysis with monolayer accuracy in terms of theoretical implementation. In addition, experimental results using ultra-thin GaAsP/GaAs superlattices are obtained. The CFTM method has not been previously demonstrated for the strain analysis of ternary alloys using HRTEM.

Characterization of strain information on HRTEM images at heterointerfaces of ternary alloys has limitations due to artifacts from the phase technique used for strain analysis. In particular, small lattice-mismatched systems ($f<3\%$) such as GaAsP/GaAs superlattices pose additional challenges. From the methodology point of view, the phase

technique generates error at heterointerfaces due to the leakage effect, and it has been shown that the error dominates for small-strained systems (f<3%) with low image resolution. Hence, this research effort was pursued to overcome the leakage effect at heterointerfaces and to minimize error from the phase technique, allowing quantitative structural analysis. Mask-size optimization to suppress the leakage effect at heterointerfaces was proposed and led to a quantitative value of measured strain at a $GaAs_{0.86}P_{0.14}$/GaAs superlattice. A simulation method using Matlab® for determining the error of the strain values as we exploit the phase technique was proposed such that we can evaluate the reliability of the phase technique with monolayer accuracy. Finally, minimization of artifacts on HRTEM images was conducted and chemical contrast was investigated using Composition Evaluation by Lattice Fringe Analysis (CELFA).

To my family. This could never have been written without your extreme sacrifices and wonderful support.

ACKNOWLEDGMENTS

First of all, I give thanks to the Creator God for providing me with encouragement, wisdom, and strength through my work on this dissertation. He is the Almighty and my Comforter. I praise the God.

Words would not be sufficient to express my gratitude to Dr. Brown, chairman of my dissertation committee, for his guidance and financial support. Growth of Group III-Nitride films using Molecular Beam Epitaxy will be the most valuable asset in my life.

I owe a debt of gratitude to Dr. Reinhard and Dr. Hogan. Their guidance and comments on my research were very helpful. I also appreciate Dr. Fan and Dr. Cramp for discussions related with microscopy work. Without their support, I would not produce this outcome.

I would like to express my sincere appreciation to Dr. Hong, assistant professor in the Mechanical Engineering Department at Michigan State University, for discussions of the computational Fourier Transform moiré method. I also thank Dr. Goldman, professor in Material Science and Engineering at the University of Michigan, for the opportunity of growth of compound semiconductors using Molecular Beam Epitaxy.

I am deeply grateful to Karl Dersch for supporting clean room facilities in the Electrical and Computer Engineering Department.

TABLE OF CONTENTS

LIST OF TABLES

LIST OF FIGURES

CHAPTER 1

INTRODUCTION

The growth of heterostructures by molecular beam epitaxy (MBE) provides significant advantages in band gap engineering. An important class of commercial semiconductor materials that cover the visible and IR spectrum is the III-V ternary alloys based on alloying GaAs and GaP, which are denoted as gallium arsenide phosphide ($GaAs_{1-x}P_x$). When $x<0.45$, the alloy $GaAs_{1-x}P_x$ is a direct bandgap semiconductor and the wavelength ranges from about 630nm, red, for $x=0.45$ ($GaAs_{0.55}P_{0.45}$) to 870 nm for $x=0$, GaAs for the application of visible and IR detectors and emitters. When $x>0.45$, the alloy $GaAs_{1-x}P_x$ is an indirect bandgap semiconductor. However, if we add isoelectronic impurities such as nitrogen (also group V element) into the semiconductor, then some of these N atoms substitute for P atoms. Nitrogen doped indirect bandgap $GaAs_{1-x}P_x$ alloys are widely used in inexpensive green, yellow, and orange LEDs while indium arsenide phosphide (InAsP) can be used within 1.3 - 3.0 μm. Recently, strain balanced GaAsP/InGaAs quantum well solar cells on GaAs were reported by Ekins-Daukes *et al.* with increased cell efficiencies over standard GaAs single junction solar cells [1]. Figure 1.1 summarizes some typical wavelengths for a few selected semiconductor materials over the range from 0.4 to 1.7μm.

The GaAsP and InAsP III-V ternary alloys are examples of mixed anion materials, which are of current interest in the development of advanced devices. Mixed anion materials composed of a few monolayers are used to form heterointerfaces and are synthesized as strained layers on binary substrates such as GaAs and InP.

Mixed anion layers, having thicknesses of a few monolayers, exhibit fascinating electrical and optical properties. The molecular beam epitaxy (MBE) growth technique plays a vital role in making compositionally abrupt interfaces at mixed anion layers. Therefore, the characterization of a few monolayers or heterointerfaces is essential to the development of novel device structures. However, very few techniques have been established to investigate strain with monolayer accuracy on High-Resolution Transmission Electron Microscopy (HRTEM) images. Furthermore, the strain analysis of heterointerfaces has been a challenge due to artifacts on HRTEM images.

The objective of this research includes four aspects. First, theoretical implementation of the CFTM method on HRTEM images for strain analysis is performed, where the CFTM method was originally developed on solder ball connect (SBC) assemblies [2]. Second, strain analysis is investigated at the heterointerfaces of small lattice-mismatched systems ($f<3\%$) such as $GaAs_{0.86}P_{0.14}$ /GaAs superlattices, where the theoretical strain between $GaAs_{0.86}P_{0.14}$ and GaAs is around one percent. For reliable strain analysis at heterointerfaces of $GaAs_{0.86}P_{0.14}$/GaAs, this research addresses several challenges and demonstrates the solutions to minimize errors resulting from the phase technique. Third, the error of the CFTM method is quantified when two strained layers is analyzed for strain information. Fourth, chemical contrast was investigated using the Composition

Evaluation by Lattice Fringe Analysis (CELFA) method and energy-filtered TEM (EFTEM). Another advantage of the CELFA method is that it can be used to minimize errors resulting from the electron microscope.

In Chapter 2, a brief review of MBE research is provided, along with details of the installation of an MBE at Michigan State University. The basic principles of TEM, EELS, energy-filtered TEM (EFTEM), and HRTEM are summarized from Chapter 2 to Chapter 5. A literature review with previous techniques for strain analysis is introduced at Chapter 6. Previously, there was a technique known as regressional analysis that was demonstrated for a few monolayers with small lattice-mismatched materials. However, a large error occurred for Si-doped GaAs and additional Gaussian smoothing was applied to reduce this large error. Hence, strain analysis using the regressional techniques has major challenges in dealing with a few monolayers.

The primary advantage of the phase technique is speed, the phase technique is much faster than regressional analysis, because it can be implemented with digital image processing from start to finish, and provides 2D strain mapping, while regressional analysis provides only 1D mapping. The phase technique is summarized in Chapter 7.

Experimental results are addressed in Chapter 8. Simulations are described in Chapter 9 to understand the source of errors in the experimental results. The Composition Evaluation by Lattice Fringe Analysis (CELFA) method is provided with experimental results in Chapter 10. Conclusions are provided in Chapter 11.

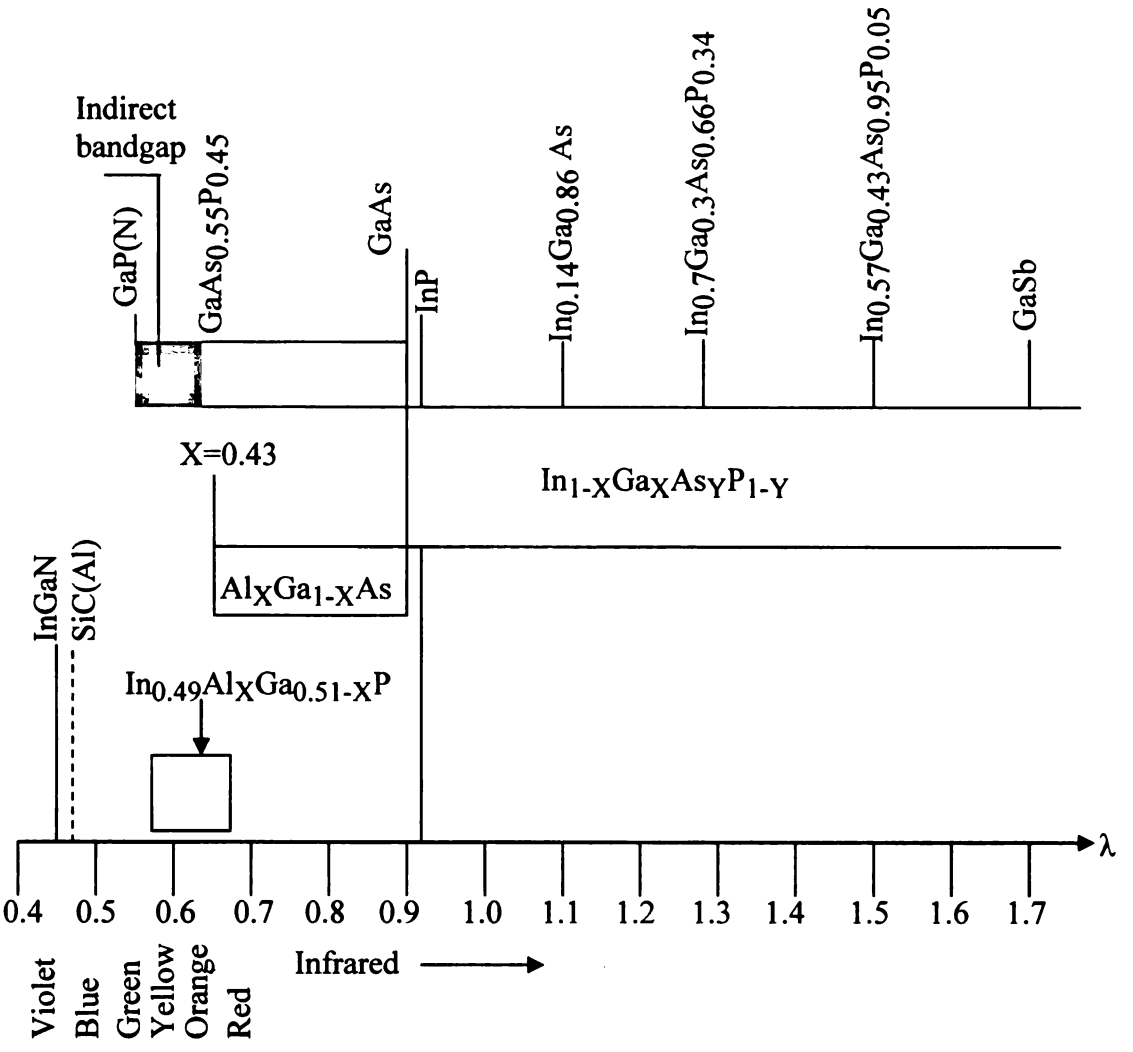

Figure 1.1: Wavelength coverage by different LED materials from the visible spectrum to the infrared. Shadowed and dashed lines are indirect E_g materials [3].

CHAPTER 2

MOLECUAR BEAM EPITAXY

2.1 Current Status of MBE growth for compound semiconductors

Molecular Beam Epitaxy (MBE) is an epitaxial growth process that involves chemical and physical reactions between atomic or molecular beams and a heated substrate under ultra-high-vacuum (UHV). The primary advantage of MBE is the capability of growing high-quality films under ultra-high-vacuum (UHV) pressure with atomic layer control over the epitaxial process. With the MBE process, ultrathin and abrupt layers, as well as, continuous doping profiles can be obtained.

Thin-film epitaxial crystal growth of compound semiconductors by MBE has been explored in many attractive applications, including optoelectronics such as light-emitting diodes (LEDs), Solar cells, and Laser Diodes; novel sensors; and transistors such as high electron mobility transistors (HEMTs) and single electron transistors (SETs). This section begins with a brief review of devices developed using the MBE technique and a description of the GEN-II MBE system is provided in Chapter 2.2.

LEDs and Laser diodes convert electrical energy into incoherent or coherent optical radiation by electrical injection into the junction region of the p-n diode. Recent research in high-brightness blue and green LEDs [4] [5] and LDs [6] using wide bandgap materials have brought rapid development of white-light LEDs and blue-violet LDs for blue-ray discs. Significant progress has been achieved even though the exact mechanism

responsible for radiative recombination in the presence of high threading dislocation densities is under debate. Current research on LEDs and LDs is primarily concerned with minimizing dislocations in order to achieve high intensity light output. For most devices, the epitaxial layers have different crystal lattice parameters, leading to a lattice mismatch between the two crystal structures. This causes dislocations, resulting in crystal defects. Such crystal defects cause recombination of electron-hole pairs (EHPs). Progress in the nitride research area has been achieved via insertion of a buffer layer grown at low temperature between a GaN layer and a sapphire substrate, resulting in high quality (0001)-oriented GaN layers [7] [8]. After that, the growth of high quality ternary alloys InGaN [9] [10] and AlGaN [11] [12] on GaN were developed, leading to high quality heterostructures, including quantum well (QW) structures [13] [14]. In order to increase the intensity of light output for optical devices, a heterostructure device (HD) [15], e.g. InGaN/GaN quantum well [16], or quantum dots (QDs) [17] have been used. Generally, QDs inherently contain a lower density of structural defects due to a built-in strain field; however, QDs reduce radiative lifetime. Also, InGaN nanowire LEDs [18] and InGaN dot-in-a-wire heterostructures [19] have been investigated. In addition, AlGaN/GaN heterostructures have been studied for UV optoelectronics [20].

A photovoltaic device, also known as a solar cell, converts sunlight directly into electricity by generating electron-hole pairs at a junction via internal photovoltaic effects. For a given solar spectrum, conversion efficiency depends on the semiconductor materials properties and the device structure [1] [21]. GaAs and Si solar cells have comparable efficiencies, though theoretically GaAs with a higher bandgap is supposed to have a better efficiency. The largest factor reducing the efficiency of a Si solar cell is the

unabsorbed photons with $h\upsilon < E_g$ and short wavelength photons absorbed near the surface. Both of these factors are improved if we use a tandem cell structure or heterojunctions. The AlGaAs window layer overcomes the surface recombination limitation and improves cell efficiency. Tandem or cascaded cells use two or more cells in tandem or in cascade to increase the absorbed photons from the incident light. The first cell is made from a wider bandgap material and only absorbs photons with $h\upsilon > E_{g1}$. The second cell absorbs photons that pass through the first cell and have $h\upsilon > E_{g2}$.

Progress in the growth technique for GaN materials has led to intense research of AlGaN/GaN heterostructures for high electron mobility transistor (HEMT) applications, particularly in the area of high power and high frequency devices [22]. Demonstration of a two-dimensional electron gas (2DEG) in AlGaN/GaN heterostructures [23] was an important result for achieving HEMT devices. Moreover, wide bandgap materials exhibit high thermal stability and device operation at an elevated temperature (600°C) is possible. Silicon based devices have typically been limited to 350°C. Also, heterostructures with GaN materials have been focused on the area of sensor applications such as gas, liquid, and pressure sensors due to the chemical inertness of the nitrides. For example, the interaction of gaseous species with the Pt electrode leads to a change in the electronic properties of the Pt-GaN [24] Schottky contact. Also, a liquid sensor [25] for bio-applications, pressure sensors, and strain sensors [26] have been demonstrated using AlGaN/GaN heterostructures.

Several emerging areas of research that utilize heterostructures include: SET (Single Electron Transistors), single-electron memory devices using QDs (Quantum Dots) [27],

II-VI and III-V based dilute magnetic semiconductors for spin transistors and MRAM (Magnetic Random Access Memory) that records information with electron spin [28]. One of the challenges that must be addressed for MRAM applications is the discovery of materials that have acceptable room temperature ferromagnetism.

2.2 Veeco GEN-II MBE system

The GEN II MBE System at Michigan State University is configured with two separate chambers, the main vacuum chamber for growth and an intro/transfer chamber. The system layout is shown in Figure 2.1 (a) and (b). Each of these chambers is equipped with an ultra-high-vacuum (UHV) pumping system and isolated by means of gate valve. The growth chamber's center axis for film layer deposition is oriented horizontally and the substrate is held facing the source flange. The vacuum chambers are made of stainless steel due to its low chemical reactivity. All system components should be able to withstand baking at 200°C. The growth chamber contains a RHEED system and beam flux monitoring.

2.2.1 Transfer chamber

Substrates are mounted in a non-indium-bonded substrate holder, including UNI-Block™ Plus series for use in the 3" diameter sample and loaded on the cassette trolley as shown in Figure 2.2. Once loaded onto the trolley, the transfer chamber is then pumped down first by the pumping station (to 10^{-6} Torr) and then by an ion pump. Substrates are individually transferred from the trolley to the heated station of the CAR (Continuous

Azimuthal Rotation) manipulator using a transfer arm. Care should be taken to avoid crashing or dropping of substrates since this is a very delicate process.

2.2.2 Growth chamber

The CAR assembly shown in Figure 2.3 is mounted horizontally in the growth chamber (see Figure 2.4 (b)). Heater assembly should be faced down or up during installation of the CAR assembly into the growth chamber since the opening in the cryopanel is rectangular in shape (see Figure 2.4(a)). The substrate holder at the CAR assembly can be rotated 300° about the main shaft. This rotational head movement allows for aligning to the growth position, transfer, and flux measurement position. The growth position is also the correct position for Reflection High Energy Electron Diffraction (RHEED) analysis.

The CAR assembly provides substrate heating by means of a wire wound heater (see Figure 2.3(c)) with an integrated type C (W-26%Re/W-5%Re) thermocouple for feedback. Desorption of native oxides can be carried out using the CAR assembly while in the growth chamber. One advantage of desorption of the native oxide in the growth chamber is that epitaxial growth can immediately start after the native oxide has been eliminated. This helps to minimize surface contamination that might be introduced if sample cleaning is done in a separate chamber.

Abrupt film layers are achieved using shutters placed between the effusion cells and the substrate as shown in Figure 2.5. Continuous changes in chemical composition via flux control are achieved by programmed variation of the temperature of effusion cells.

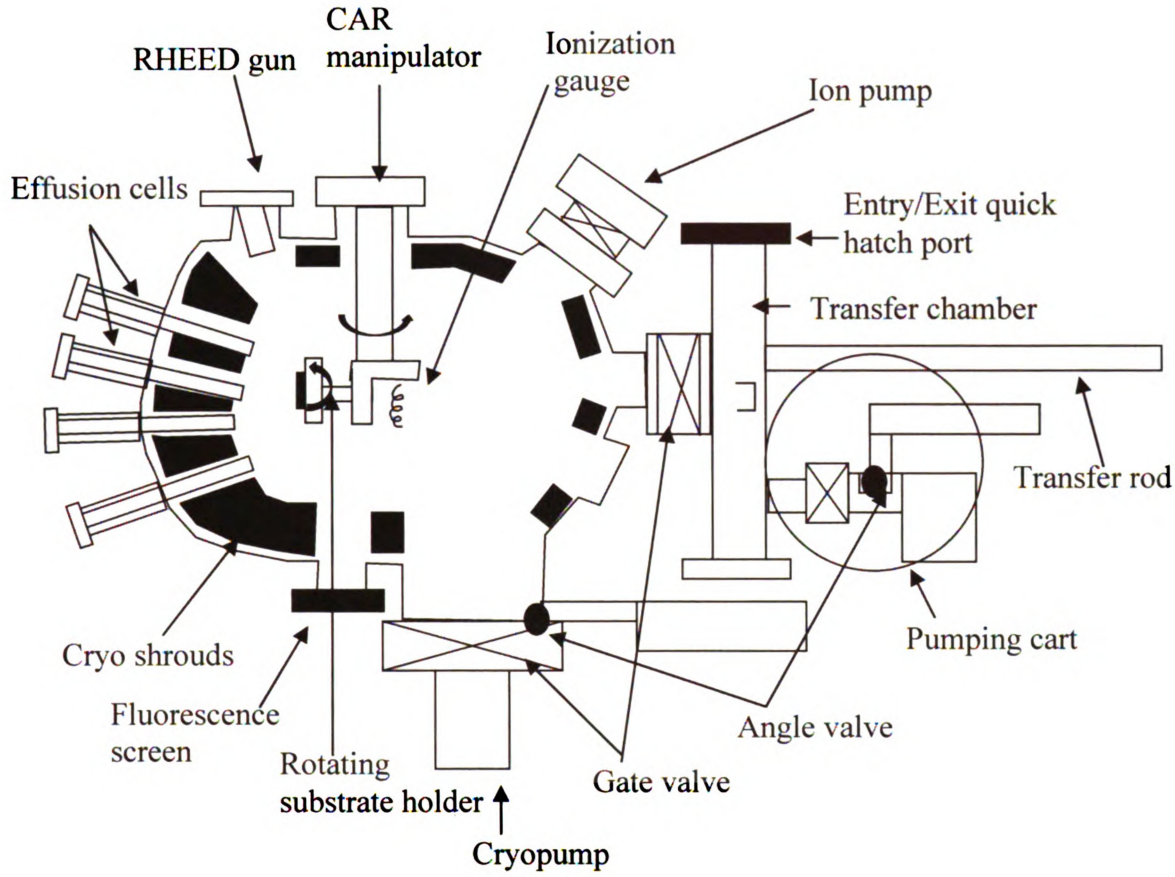

(a)

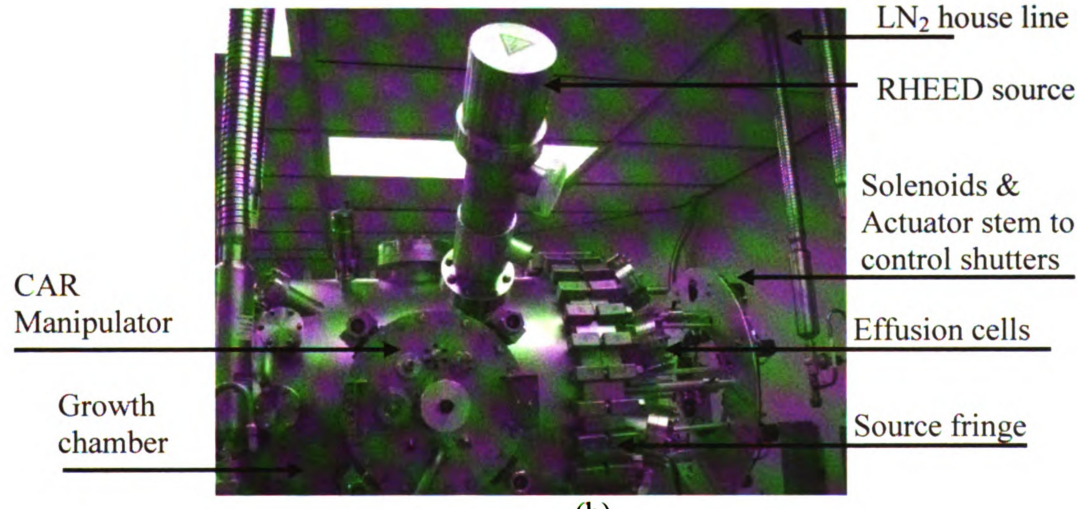

(b)

Figure 2.1: Gen II MBE system (a) Layout and (b) Gen II MBE system (CAR side)

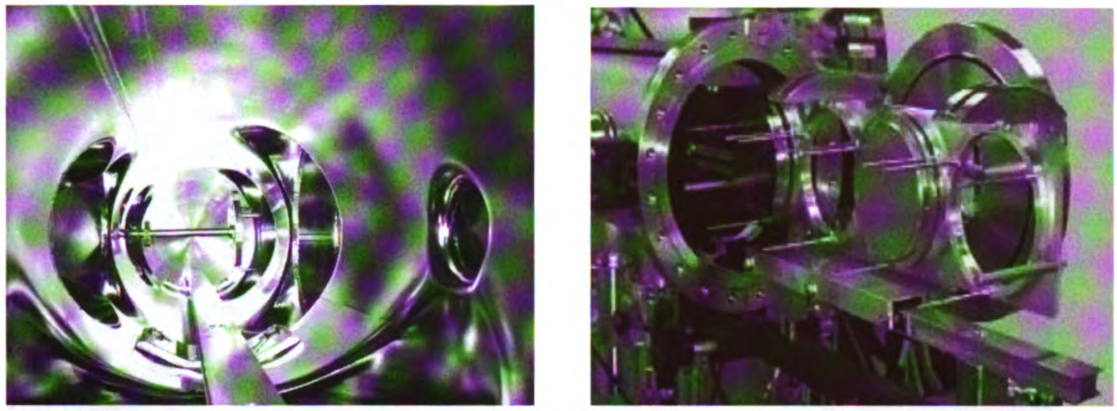

Figure 2.2: Transfer chamber (a) Inside transfer chamber (b) Trolley in transfer chamber

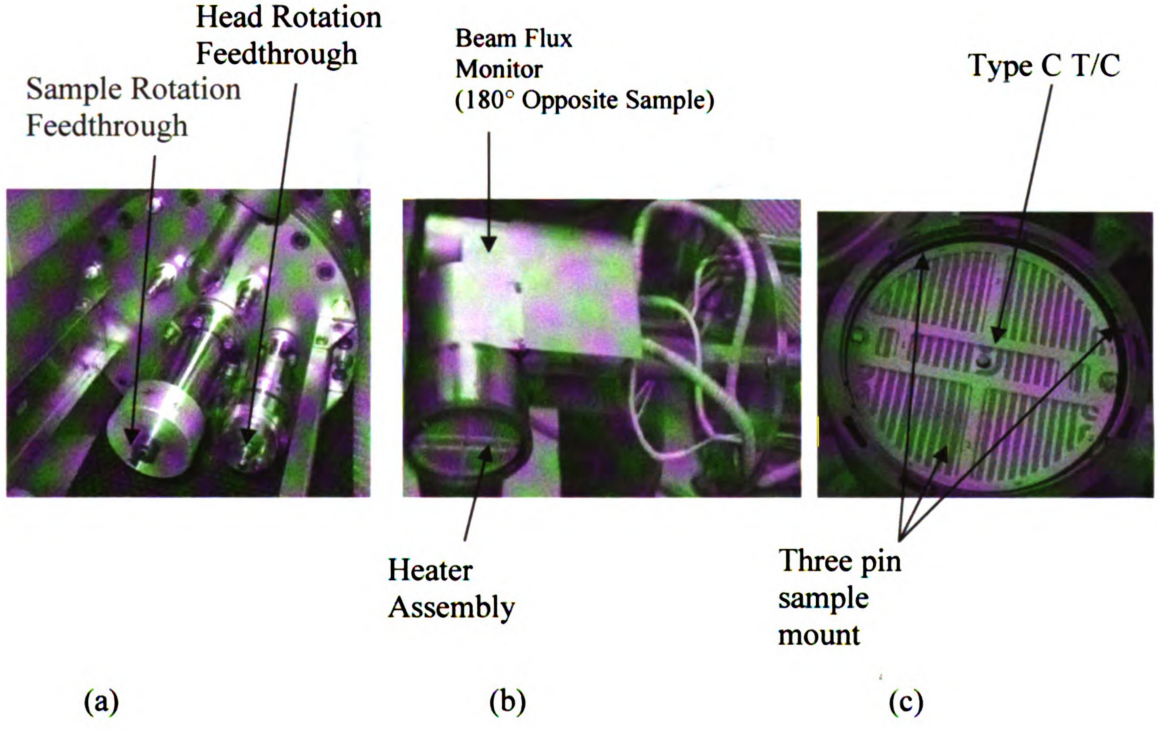

Figure 2.3: Continuous Azimuthal Rotation (CAR) assembly. (a) Sample and Head rotation feedthrough (b) Rotation-shielded head assembly (c) Heater assembly

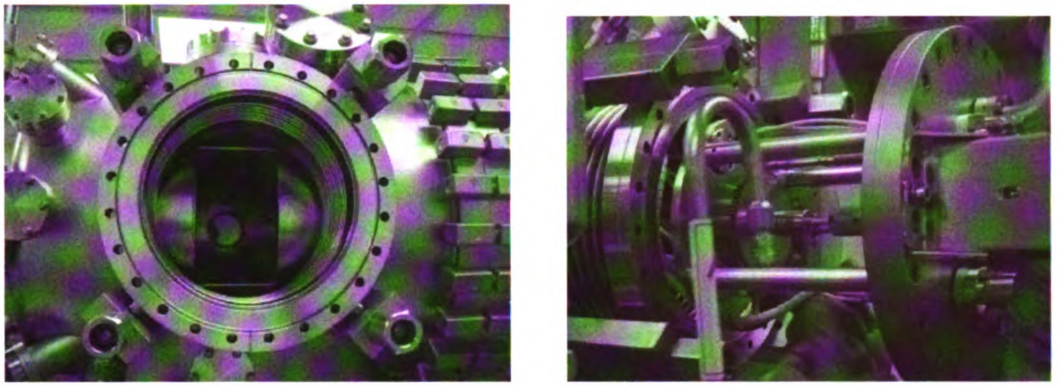

(a) (b)

Figure 2.4: CAR side of Gen II MBE system. (a) Opening for CAR manipulator (b) Installation of CAR into growth chamber

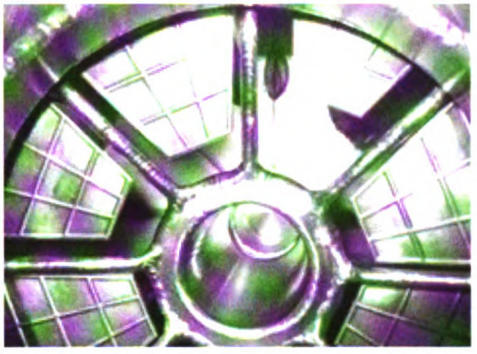

Figure 2.5: Shutters placed between effusion cells and a substrate.

2.3 Vacuum system

A very low ($<10^{-10}$ Torr) or ultra high vacuum base pressure is essential for high quality MBE growth. Under UHV conditions, the surface of a substrate can be maintained clean and free of any contaminants. The beams of atomic particles for growth do not suffer from momentum loss through collision with residual gas molecules. In order to achieve the UHV condition, there is not a single pump that reaches ultra high vacuum

from atmosphere; instead several pumping stages are used including sorption pumps, ion pumps, and a cryogenic pump.

2.3.1 Sorption pump

A triple system of sorption pumps linked with a scroll-type roughing pump is shown in Figure 2.6. Before operating the sorption pumps, the roughing pump is used to bring the growth and transfer chambers from atmosphere to ~10^{-3} Torr. Then an LN_2 trap (not shown in Figure 2.6) can further pump down ~5* 10^{-4} Torr. The sorption pumps with liquid nitrogen for the GEN II MBE system are sequentially operated to bring the growth and transfer chamber from ~5*10^{-4} Torr to 10^{-6} Torr. The sorption pumps remove molecules inside the chamber by trapping them on the surface of the sorbent. The sorbent is a solid porous material with large surface area and is typically made of a synthetic zeolite material known as molecular sieve. When the sorption pump is cooled by liquid nitrogen, the molecular sieve can absorb molecules until the pressure of the chamber reaches ~10^{-6} Torr. After several pumping cycles, the pores of the molecular sieve materials will become clogged with water vapor and the pumping efficiency will deteriorate. Water vapor is removed by baking the pump up to 300°C for 2~4 hours while pumping on the molecular sieve. The bakeout heater is shown in Figure 2.6.

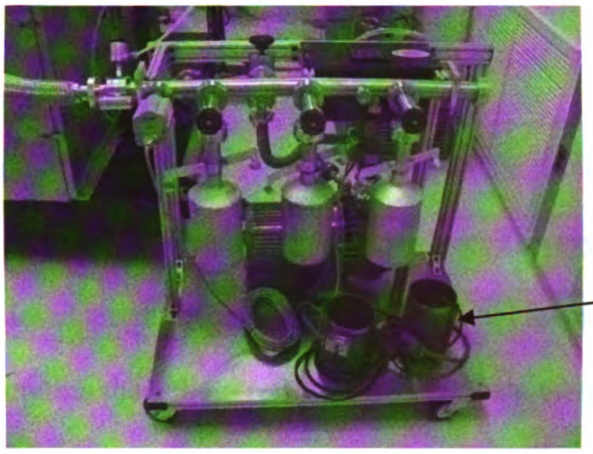

Figure 2.6: The pumping system with a roughing pump and three sorption pumps.

2.3.2 Ion pump

Ion pumps do not use oil, in contrast to diffusion pumps, providing contaminant free Ultra High Vacuum pumping (UHV). An ion pump ionizes gases and employs a strong electrical potential, typically 3kV to 7kV between a stainless steel anode and a titanium cathode. When a strong electrical potential is placed across the electrodes, a discharge is initiated by field emission. A magnetic field is utilized to confine the discharge within the pump. Pumping action is achieved when gas molecules are ionized in the discharge, and accelerated into the cathode with sufficient kinetic energy that they are permanently buried. In addition, this ion bombardment of the cathode, results in titanium being sputtered off the cathode and deposited on the pump walls. Active gases are chemisorbed by the titanium, contributing to the pumping action. Inert and lighter gases, such as He and H_2 do not effectively sputter and are absorbed by physisorption. Our system also uses a Ti sublimation pump. The active titanium surface is produced by electrically heating a filament to evaporate titanium, which in turn condenses on the walls of the vacuum chamber.

2.3.3 Cryopump

The operation of a cryopump relies primarily on the principle that any surface will act as a pump for a gas that condenses on a cold surface. The cryopump in our MBE system incorporates a closed circuit helium refrigerator to cool its active surfaces. A compressor is utilized to compress the helium refrigerant. The main advantage of cryopumps is that they provide efficient, oil-free pumping of all gases in the 10^{-3} to 10^{-10} Torr range, achieving high pumping speed. One disadvantage is that the trapped gases remain in the pump, hence, the pump needs to be regenerated periodically, by allowing it to warm to room temperature while pulling vacuum on the cryopump using a separate vacuum system in order to pump out all the adsorbed gases. Another disadvantage is that if the cryopump fails unexpectedly, the adsorbed gases will be released into the vacuum chamber, possibly damaging the MBE system. Hence, in the event of a power outage, the high vacuum side gate valve should be closed immediately, before the pump starts warming up.

CHAPTER 3

TRANSMISSION ELECTRON MICROSCOPY

Transmission electron microscopy (TEM) has been the technique most widely used for the observation of dislocations and other crystal defects, such as stacking faults, twins, grain boundaries, and voids. Static arrangements of defects are usually studied, but in some cases, miniaturized tensile devices have been used to deform specimens (less than 3mm in length) within a microscope, thus providing direct observation of dislocation interactions and multiplication processes. TEM is applicable to a wide range of materials, subject only to the condition that the specimen can be prepared in a very thin section, and that they remain stable when exposed to a beam of high-energy electrons within a high vacuum system. A schematic of a conventional transmission electron microscope is shown in Figure 3.1.

3.1 Functions of Each Lens and Aperture

3.1.1 Condenser Lens and Aperture.

The condenser lens consists of two lenses (C1 and C2). The C1 and C2 lenses are adjusted to illuminate the specimen with parallel beams of electrons from the gun as shown in Figure 3.2. The C1 lens first forms a de-magnified image of the gun crossover while the C2 lens controls illumination (converged or parallel beam) and the beam's

intensity on a specimen. We call the C2 brightness. If we want to increase the intensity of the beam on a specific area of a specimen, we focus the beam more. In other words, when we intend to slightly minimize the area of the specimen that we are illuminating, we simply change the C2 (brightness) lens so that it is focused. For normal image mode we underfocus C2 (brightness) until the illuminated area on the specimen fills the viewing screen. This is also the case for several alignments (*i.e.* Z-height correction, condenser astigmatism, centering of current, and centering of voltage etc.). The Z-height correction is to fix the specimen's height on the optic axis to allow us to obtain the same objective lens current and thus a fixed objective lens magnification. The centering of the current involves the objective lens rotation alignment to ensure that the objective lens field is centered on the optic axis. As a result, direct electrons leaving from the specimen see a symmetric field as they pass through the lens. The voltage centering should be preformed when a varying voltage is applied to the gun and the objective lens is aligned to ensure the electrons remain on axis through the lens as their energy varies. Also, we need to deliberately create a focused convergent beam on the specimen for the convergent-beam mode. The convergent beam is a probe. We use such a probe to get a signal from only a localized area of the specimen. For example, defect analyses with EDX or EELS, scanning of the beam via STEM, or convergent-beam diffraction.

On the other hand, the condenser aperture excludes stray electrons. However, if we use a smaller aperture, the angle of the beam convergence is decreased, which makes the beam more parallel as shown in Figure 3.2 (b).

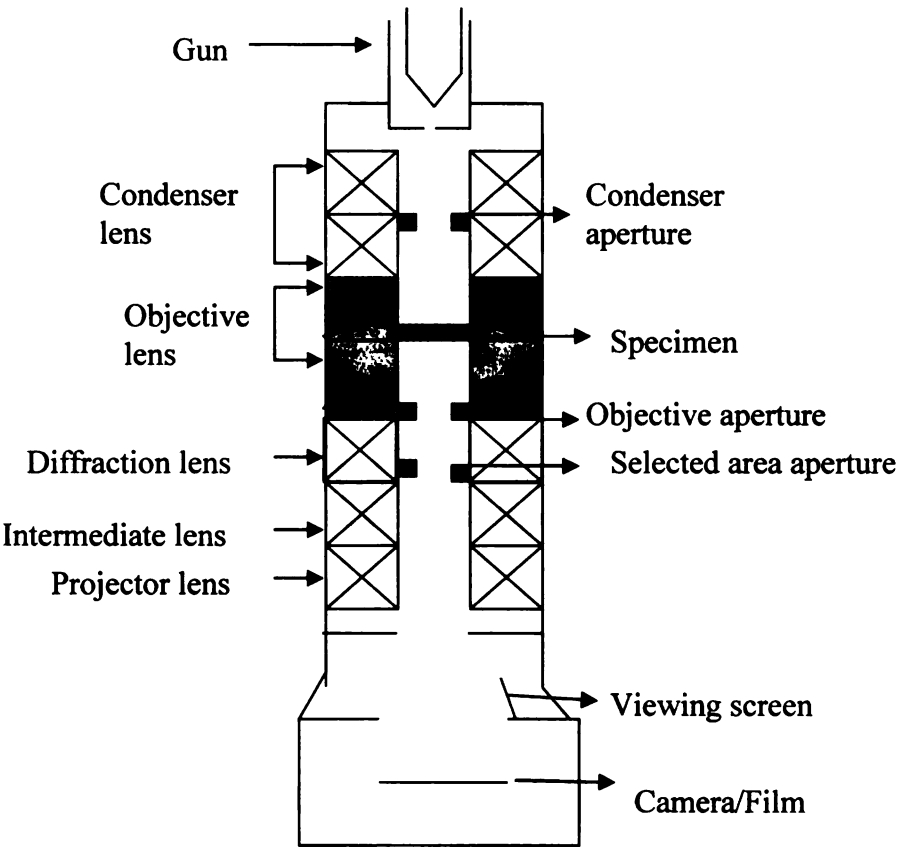

Figure 3.1: Schematic diagram of a TEM system

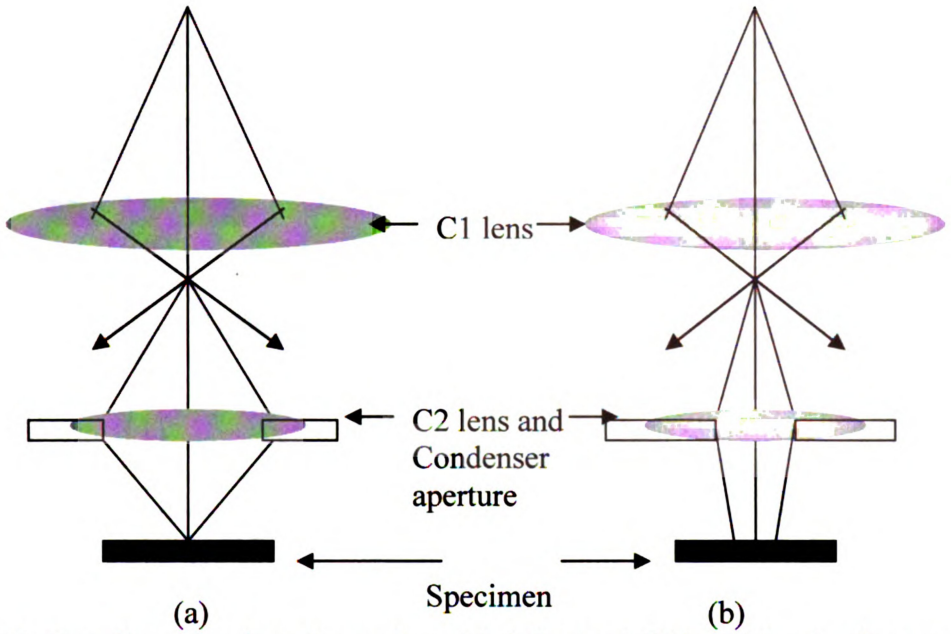

Figure 3.2: Ray diagram of condenser lens (a) A focused C2 lens illuminating a small area of the specimen. (b) Effect of condenser aperture on the parallel nature of the beam: a smaller aperture creates a more parallel beam[29].

3.1.2 Objective lens

The objective lens is the most important component of the TEM since it creates the image on the image plane and diffraction patterns on the back focal plane. The ray diagram from specimen to viewing screen is shown in Figure 3.3. Notice that switching between diffraction pattern and image is conducted by the objective aperture and the selected area aperture.

The objective lens takes the electrons leaving from the exit surface of the specimen and disperses them to create a diffraction pattern in the back focal plane. It then recombines them to form an image in the image plane (see Figure 3.4). If we divide infinitesimal points on the object, each infinitesimal point is converged on the same point of the image plane no matter how the scattering events occur in the specimen (see Figure 3.4).

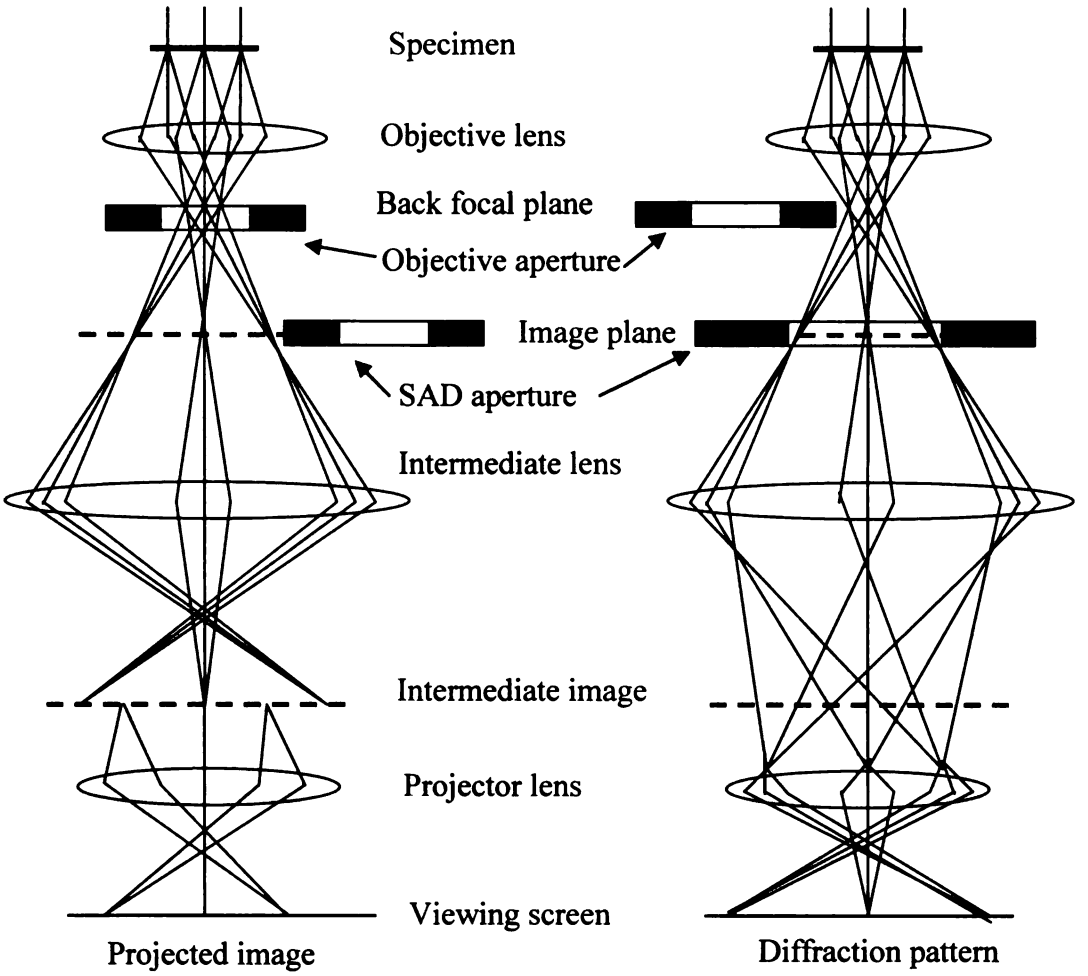

Figure 3.3: Two basic operations of the TEM imaging system. (a) Projected image on the viewing screen (b) Diffraction pattern on the viewing screen.

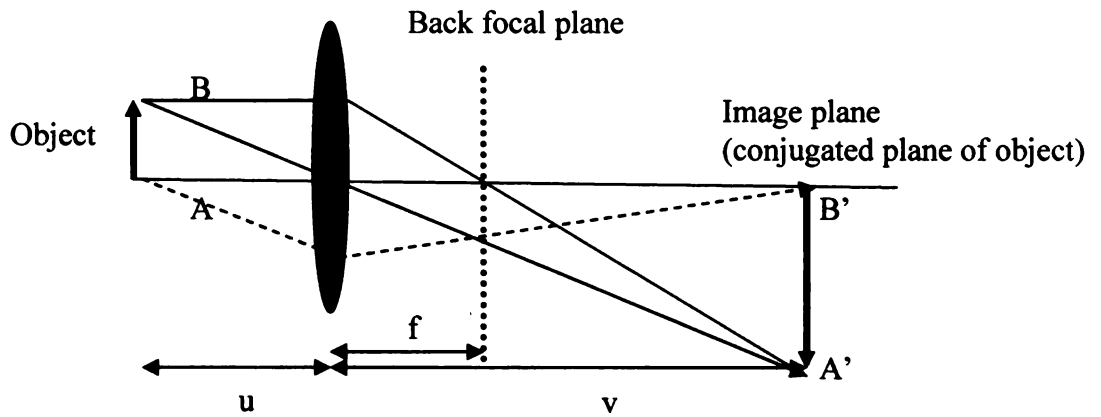

Figure 3.4: Ray diagram of an objective lens. The distance from the object plane to the lens (u), the distance from the lens to the image plane (v), and the distance from the lens to the back focal plane (f).

From the Figure 3.4, any parallel beams from the object are converged at the same point on the back focal plane. That is the principle behind the diffraction pattern. Another process occurring between the object and image plane is magnification. From the Newton's lens equation, the relationship between the relative positions is:

$$\frac{1}{u}+\frac{1}{v}=\frac{1}{f}$$

And the magnification of a convex lens is given by:

$$M=\frac{A'B'}{AB}=\frac{v}{u}$$

Therefore, a high magnification can be realized by putting the object close to the lens, making u small and M large. Otherwise, if we make the lens weaker, then the focal length is increased. If f is enlarged but u is unchanged, then v must be correspondingly longer, and the image magnification is larger. This magnification is the major role of the intermediate lens and projector lens as shown in Figure 3.3.

3.1.3 Selected Area Aperture

The selected area aperture is an essential component for obtaining a diffraction pattern. This operation is called selected-area diffraction (SAD). The position of the selected area aperture is the conjugate plane of the specimen since we cannot insert the selected area aperture in the specimen position. The conjugate plane is the image of the objective lens as shown in Figure 3.4. The SAD aperture is inserted into the image plane of objective lens. Then any electron that hits the specimen outside the area defined by the virtual aperture will hit the real diaphragm as shown in Figure 3.5. Thus, it will be excluded from contributing to the diffraction pattern. By choosing a specific small area,

we can protect the camera from the high intensity of the electron beam. After inserting SAD aperture, we can obtain diffraction patterns by turning on the diffraction mode of the diffraction lens of Figure 3.1, which switches the back focal plane of the objective lens as its object. As shown in Figure 3.3, objective aperture should be taken out before inserting the SAD aperture in order to select the back focal plane as an object. To convert to image mode, we have to remove the SAD aperture and switch into image mode of the diffraction lens.

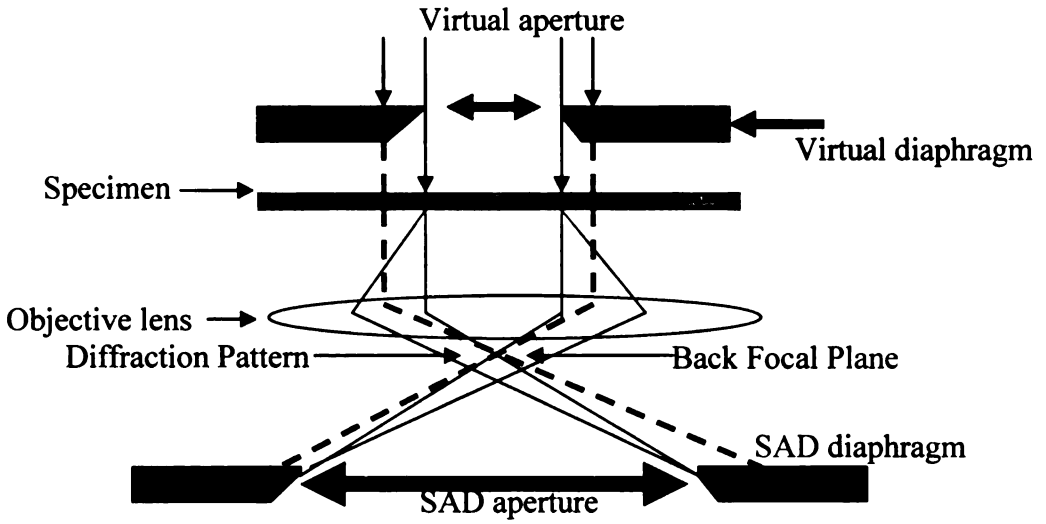

Figure 3.5: Ray diagram of SAD aperture. Insertion of an aperture in the image plane results in the creation of a virtual aperture in the plane of the specimen.

3.1.4 Objective aperture

An additional principle of TEM operation is the bright-field (BF) image and dark-field (DF) image. These two modes are created by the objective aperture. The bright-field (BF) image is generated by allowing only the forward beam to pass through the objective aperture. On the contrary, the dark-field (DF) image is generated by allowing any of the diffracted beams to pass through the objective aperture. The contrast in BF and DF

images is called the diffraction contrast. Figure 3.6 shows the optical ray diagram of bright-field from a specimen to the image plane. The forward beam is converged at the back focal plane on the optic-axis and forms the image on the image plane.

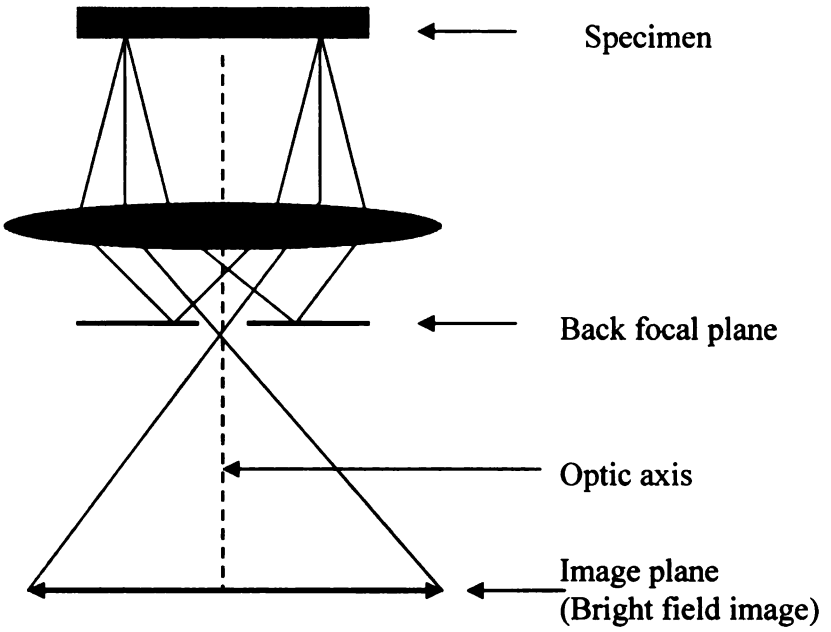

Figure 3.6: Optical ray diagram of bright-field (BF) from a specimen to image plane. An aperture is placed in the back focal plane of the objective lens which allows only the direct beam to pass

When the electron beam encounters a specimen, many electrons are strongly scattered due to mass-thickness or specimen orientation difference. By choosing only the direct beam, we can improve contrast of the image. This is shown in Figure 3.7.

The other mode is the dark-field (DF) image. The dark field is formed by choosing a diffracted beam of many diffracted beams. The DF image provides high contrast image with low intensity while BF image provides low contrast image with high intensity.

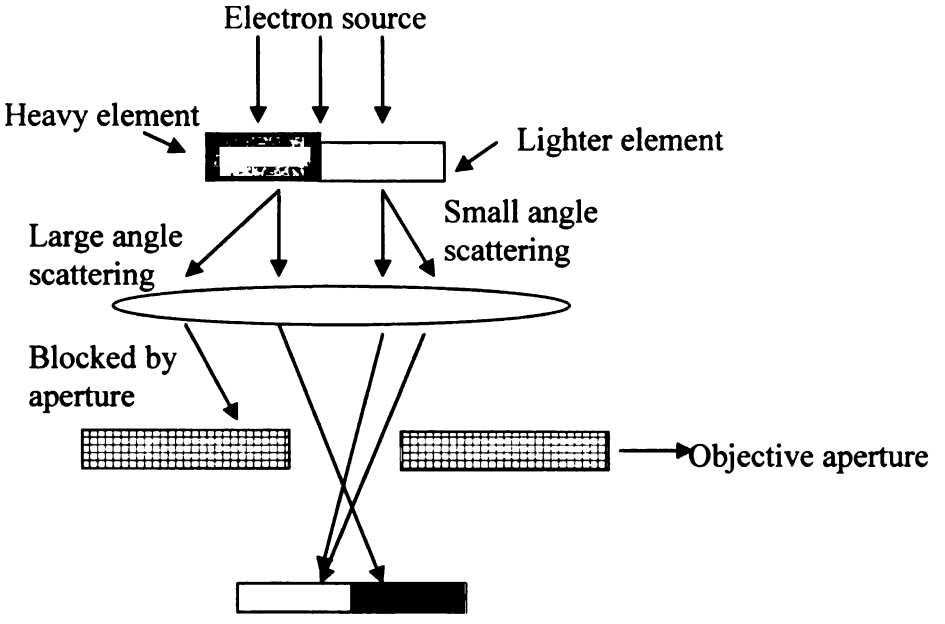

Figure 3.7: Ray diagram of a bright-field image. Thicker or higher-Z area of the specimen (gray area) will scatter more electrons off axis than thinner or lower-mass (white area). Thus fewer electrons from the gray region fall on the equivalent area (black area) of the image plane, which improves contrast relative to without the objective aperture.

CHAPTER 4

ELECTRON ENERGY-LOSS SPECTROSCOPY AND ENERGY-FILTERED TEM

4.1 Electron Scattering Theory

When a uniform intensity of electrons encounters a thin sample, the intensity is modified and corresponds with the sample's mass and thickness. In addition to the intensity, scattering events change the angular distribution as shown in Figure 4.1. When we consider scattering events, the simplest process is single scattering (*i.e.* an electron undergoes either a single scattering event or no scattering) through the sample. If a second scattering event happens, the electron could go back into the direct beam so that it appears to have experienced no scattering. The single scattering assumption is often very reasonable if the sample is thin.

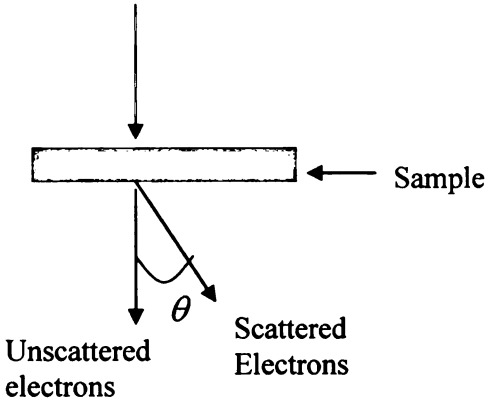

Figure 4.1: Diagram for unscattered and scattered electrons

The scattering causes an angular distribution of electrons and can be mainly divided into elastic and inelastic scattering (see Figure 4.2). The term elastic means that there is no change in energy, but there is a change in the deflection angle. Inelastic scattering refers to the beam of electrons that are scattered such that there is a change in energy which involves the inner or outer shell atomic electrons. Inelastic interactions carry information about the nature of the atoms, their electronic structure, and their bonding with surrounding atoms.

Figure 4.2 (a) shows two mechanisms by which an incident electron is scattered by an isolated atom. Coulombic interaction within the electron cloud results in low-angle (θ) elastic scattering, while Coulombic attraction by the nucleus results in backscattering. Note that the potential within the electron cloud is always positive. Figure 4.2 (b) shows inelastic scattering resulting from interaction between inner-shell electron (core electron) and an incident electron beam. Figure 4.2 (c) shows inelastic scattering due to interaction between outer-shell (valance electron) and an incident electron beam. Therefore, different energies involved in inner and outer-shell scattering occupy different parts of the EELS spectrum. This will be discussed further in Section 4.2.

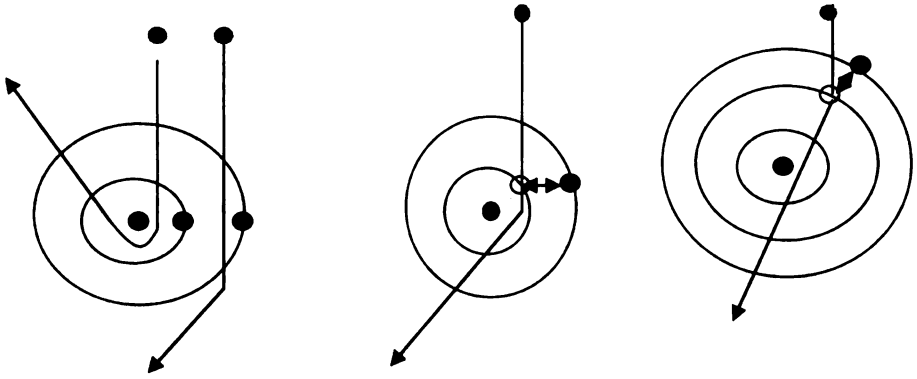

(a) (b) (c)

Figure 4.2: Two mechanisms where an incident electron is scattered by an isolated atom. (a) Elastic scattering (b) Inelastic scattering (inner-shell ionization) (c) Inelastic scattering (outer-shell ionization)

4.2 Electron Energy-Loss Spectroscopy (EELS)

Electron energy loss spectroscopy (EELS) measures the energy loss of the electrons that interact with the sample. It measures the energy transfer between the electrons in the incident beam and atomic electrons. Information regarding the local environment of the atomic electrons and nearest neighbor atoms can be obtained. The method used for separating electrons of different energy involves a magnetic prism mounted above the intermediate lens, since the magnetic prism is compact and provides sufficient energy resolution to distinguish all the elements in the periodic table.

When electrons pass through a uniform magnetic field, they are deflected by the magnetic field. The amount of deflection is determined by the energy loss that the

electrons experienced. The greater the energy loss of the electron, the further it is deflected. Therefore, electrons with different energies can be physically separated. This is the operation principle of EELS.

The EELS can be mainly divided into three parts on the spectrum: zero-loss peak, low-loss spectrum, and high-loss spectrum. First, the zero-loss peak is the most intense spectrum and contains the elastic forward-scattered electrons that experienced very small energy loss. Hence, these electrons have approximately the same energy as the incoming electron beam. Second, the low-loss spectrum appears close to the zero-loss peak and is much lower in intensity than the zero-loss peak. It contains electrons that interacted with the weakly-bound outer shell electrons, plasmons, or phonons of the sample, resulting in low energy losses. The low-loss spectrum is generally located below 50eV. Third, the high-loss spectrum contains electrons that interacted inelastically with tightly bound inner-shell (core) electrons, and it appears above 50eV.

4.2.1 Low energy loss range (<50eV) and Plasmons

The plasmon process is the most common inelastic interaction (see Figure 4.3). The plasmons are longitudinal wave-like oscillations of weakly bound electrons. When an electron beam passes through the free electrons of the conduction band, plasmon (*i.e.* collective oscillations of the free electrons of the conduction band) occurs. Hence, the plasmons can happen in any material with weakly bound or free electrons and occurs most often in metals.

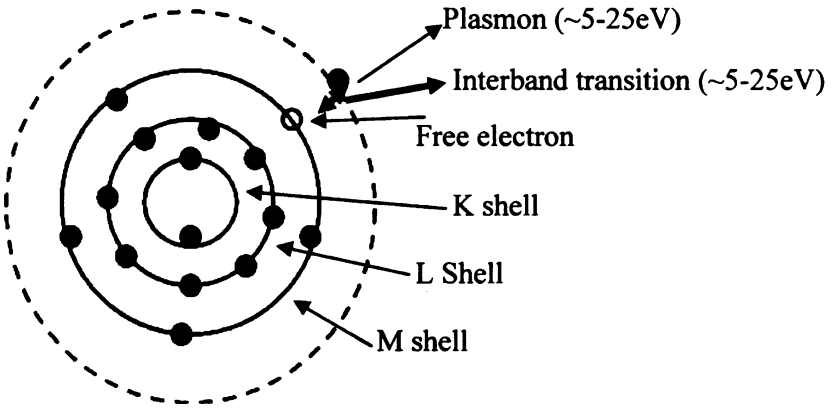

Figure 4.3: Inelastic scattering at phosphorous

The energy *Ep* lost by the beam of electrons as it generates a plasmon of resonance frequency ω_p is given by:

$$E_p = \frac{h\omega_p}{2\pi} = \frac{h}{2\pi}\left(\frac{ne^2}{\varepsilon_0 m}\right)^{\frac{1}{2}} \quad [29]$$

where ω_p is the resonance frequency of the plasmon. The excited plasmon peak absorbs the energy *Ep* for low loss EELS. We call the second spectrum a plasmon peak (see Figure 4.4). Plasmon is the second most dominant peak of the energy-loss spectrum. Note that the plasmon peak could include inter-intra band transition or lattice vibrations (phonon). Generally, the plasmon peak includes all possible outer-shell interactions of

scattering events. However, there are times when we cannot distinguish the second spectrum with plasmon, phonon, inner transition, or intra transition, since their energies are close to each other. As a result, we generally call the second spectrum a plasmon spectrum. The principal energy loss processes due to scattering are listed in Table 4.1.

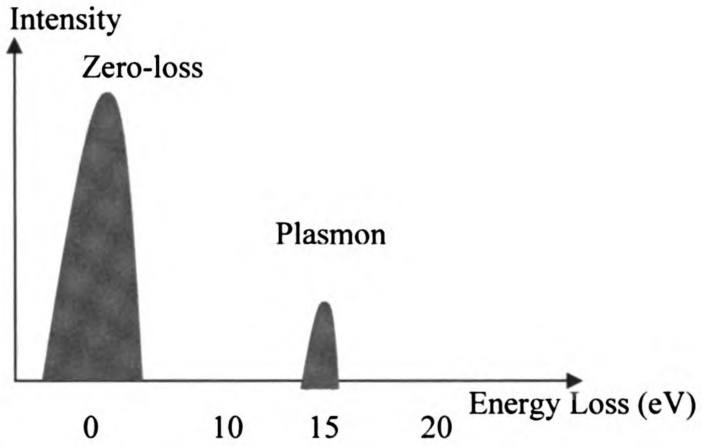

Figure 4.4: Zero-loss and plasmon peaks in energy-loss spectrum.

Table 4.1: Characteristics of the principal energy-loss processes

Process	**Energy Loss (eV)**
Phonons	~0.02
Inter/Intra-band transitions	5-25
Plasmons	~5-25
Inner-shell ionization	~10-1000

4.2.2 Thickness measurement of a sample

The plasmon excitation is a useful way to measure the thickness of a TEM sample. A typical value of the plasmon mean-free path λ_p is listed in Table 4.2. The λ_p is about a few hundred nanometers. Hence, it is reasonable to expect at least one strong plasmon peak in a thin sample. However, if the sample is thick, a number of individual losses

should occur. Hence, there is thickness information in the energy-loss spectrum since the amount of all inelastic scattering increases with sample thickness.

Table 4.2: Plasmon loss data for 100eV electrons of several elements [29]

Material	Ep(calc.)	Ep(exp.)	λ_p (calc.)
	(eV)	(eV)	(nm)
Li	8.0	7.1	233
Be	18.4	18.7	102
Al	15.8	15.0	119
Si	16.6	16.5	115
K	4.3	3.7	402

In principle, the probability of a single inelastic scattering event is given by:

$P = \frac{t}{\lambda}$ (t: thickness, λ : inelastic mean free path)

For multiple scattering of *n* events, the probability follows the Poisson distribution and is expressed:

$$P_n = \frac{I_n}{I_t} = (\frac{t}{\lambda})^n \frac{\exp(\frac{-t}{\lambda})}{n!},$$

where I_n is the *n*-th scattered intensity, I_t is the total intensity.

For *n=0*, $\frac{I_0}{I_t} = \exp(\frac{-t}{\lambda})$ where I_0 is the elastic scattered electrons. Therefore, we can obtain a relationship between the thickness and the inelastic MFP (mean free path) versus elastic scattered electrons and total intensity:

$$\frac{t}{\lambda} = \ln(\frac{I_t}{I_0}).$$

This gives us a relative thickness. Finally, the relative thickness multiplies the mean free path and gives absolute thickness. The inelastic MFP is given by:

$$\lambda \approx \frac{106FE_0}{\{E_m \ln(\frac{2\beta E_0}{E_m})\}}$$, λ is nm in unit, E_o is keV, β is collection semiangle, E_m is the average energy loss in eV and F is a relativistic correction factor.

The E_m and F is given by:

$$F = \frac{\{1+\frac{E_0}{1022}\}}{\{1+(\frac{E_0}{511})^2\}}$$, (F=0.618 at E_0=200 keV)

$$E_m = 7.6Z^{0.36}$$

The I_o and I_t are drawn in Figure 4.5.

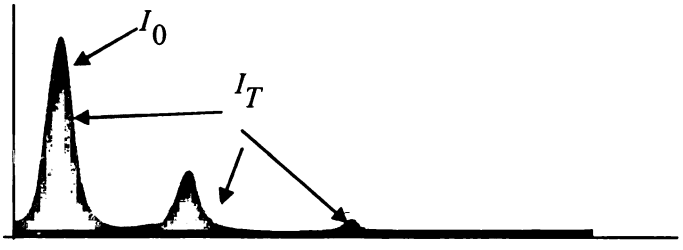

Figure 4.5: Intensity under the zero-loss peak (I_0) and the total intensity.

4.2.3 High Energy Loss Range (>50eV)

The energy needed for ionization processes is transferred from the incoming electron beam to a core-shell electron in the atom. Since the ionization process is characteristic of the atom, the high-loss spectrum provides chemical information.

Electrons with the atoms can excite an empty state by accepting a specific value of energy. The incident fast electrons which provide this energy suffer a loss of the same amount. The minimum energy causing the ionization threshold is called the critical ionization energy (E_c). Of course, if the incident electron is greater than Ec, ionization could be possible. However, the chances of ionization become less with increasing energy above E_c, since the value of the cross section decreases with increasing energy. As a result, the ionization-loss electrons have an energy distribution that ideally shows a sharp rise to maximum at E_c, followed by a slowly decreasing intensity above E_c back toward the background coming from any previous peak. That is the reason we call it an "edge". The edge energy is determined where the first derivative is maximized or the second derivative is zero. In the case of ionization energy of K-shell electron, we call it E_K and E_L for L-shell ionization energy. The presence of certain elements can be determined from the appearance of the edges in the spectrum.

4.3 Energy Filtered TEM (EFTEM)

If we consider a point in a sample, the point is transferred on a point in the TEM image no matter what scattering events occur. That is how a lens works. However, we can select specific electrons which have the same energy using EFTEM. The energy filter component is installed between the intermediate lens and projector lens. This special filter allows for selection of a very narrow window of energies in the EELS spectrum. Using the corresponding electrons for imaging, EFTEM is performed.

CHAPTER 5

HIGH-RESOLUTION TRANSMISSION ELECTRON MICROSCOPY

The HRTEM utilizes phase-contrast imaging and represents interference patterns between the forward-scattered and diffracted electrons from a sample (see Figure 3.6). The phase shift can be created by periodic potentials that the electron sees as it passes through the sample, during image processing. Since a lens is not perfect, the image processing modifies the diffracted wave by the effects of defocus, energy spread, spherical aberration, etc. The phase shift resulting from image processing is represented with a contrast transfer function. This function is described in Section 5.3.

5.1 Fourier Transform

If we consider the wave function $\Psi(r)$ at the exit face of a sample, and $\Psi(g)$ at the back focal plane, then g is the reciprocal vector, and the diffraction pattern, $\Psi(g)$, is the Fourier transform of the wave function at the exit face of the sample. Therefore,

$\Psi(g) = F\Psi(r) \cdot T(g)$

where $T(g)$ is called the contrast transfer function and F is the Fourier Transform operator. The intensity of the diffraction pattern in the back focal plane is $|\Psi(g)|^2$. Consequently, the final image wave function $\Phi(r)$ is the inverse Fourier transform of $\Psi(g)$. The final image wave function will be $\Phi(r) = \Psi(r) \otimes T(r)$. The intensity of the

image is $\Phi(r)\cdot\Phi(r)^{*} = |\Phi(r)|^{2}$.

5.2 Weak-Phase-Object Approximation

A general model of $\Psi(r)$ at the exit face of a sample can be described as below:

$$\Psi(r) = A(r)\exp(i\Phi_t(x,y))$$

where $A(r)$ is the amplitude and $\Phi_t(x,y)$ is the phase, which depends on the thickness of the sample. The $A(r)$ can be set to unity since HRTEM utilizes phase-contrast imaging. When the electron passes through the sample, its wavelength is modified from λ to λ' as given below:

$$\lambda = \frac{h}{\sqrt{2meE}} \text{ and } \lambda' = \frac{h}{\sqrt{2me(E+V(x,y,z))}}.$$

Hence, the phase change is given by:

$$d\phi = \frac{2\pi}{\lambda'}dz - \frac{2\pi}{\lambda}dz = \frac{2\pi}{\lambda}dz\left(\frac{\sqrt{E+V(x,y,z)}}{\sqrt{E}} - 1\right) \approx \frac{\pi}{\lambda E}V(x,y,z)dz = \frac{\pi}{\lambda E}V_t(x,y) = \sigma V_t(x,y)$$

where the $V_t(x,y)$ is the projected potential in the z-direction and σ is the interaction constant. As a result, the wave function at the exit face of the sample, $\Psi(r)$, can be written as $\Psi(r) = \exp[i\sigma V_t(x,y)]$.

If the sample is very thin (*i.e.* $V_t(x,y) << 1$), we can expand the exponential function, resulting in $\Psi(r) = 1 + i\sigma V_t(x,y)$. The final form of the wave function at the exit face of the sample is called the weak-phase-object approximation, such that $\Psi(r)$ is linearly related to the potential of the sample when the sample is very thin. Generally, the TEM sample is thin enough to use the weak-phase-object approximation.

5.3 Contrast Transfer Function

The contrast transfer function describes instrumental instability, defocus, imperfect lens, etc. In real space, the contrast transfer function is a sinc function (*i.e.* point spread function) and it is applied across the image by convolution theorem of the Fourier transform. Hence, it produces a blurring effect limiting the resolution. In the back focal plane, the contrast transfer function multiplies the diffracted wave and limits instrumental resolution. The phase contrast function can be written as:

$$T(g) = 2A(g) \cdot \sin \chi(g)$$

where A(g) is the aperture function and $\chi(g)$ is the phase-distortion function describing phase shift due to spherical aberration and defocus. The $A(g)$ is unity when g's are allowed to pass the aperture and zero when the g's are blocked. The $\chi(g)$ is affected by spherical aberration and defocus given by:

$$\chi(g) = \pi \Delta f \lambda g^2 + \frac{1}{2} \pi C_S \lambda^3 g^4$$

where C_S is spherical aberration, λ is the electron wavelength, g is magnitude of **g**, and Δf is defocus. Figure 5.1 shows a typical transfer function. The transfer function can be optimized by adjusting Δf and C_S. The transfer function is oscillatory and there is a band of good transmission. However the zeros do not contribute to the output signal.

The best transfer function can be obtained by three points of view. Firstly, the first crossover with g axis should be large so that a higher spatial resolution can be obtained. The first crossover is defined as instrumental resolution limit. Secondly, the *T(g)* is large so that information with a periodicity or spatial frequency corresponding to that value of *g* will be strongly transmitted. Thirdly, the different values of g should have the same

contrasts, which means a flat function at band region. As a result, all the atoms at atomic column positions appear as either dark or bright spots. In summary, flat response of the contrast transfer function and beams as many as possible with identical phase transferred through the optical system are fundamental principles of phase-contrast imaging in HRTEM.

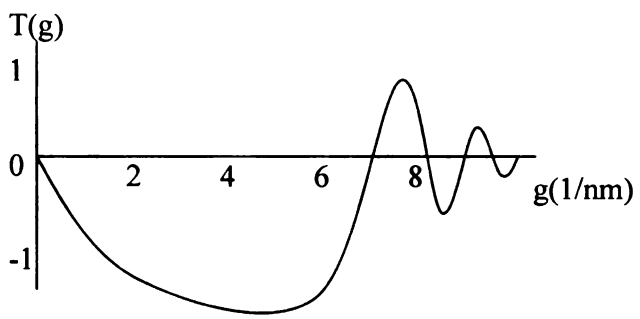

Figure 5.1: An example of contrast transfer function, T(g), versus g.

CHAPTER 6

LITERATURE REVIEWS

6.1 Previous methods for strain analysis

Several methods have been demonstrated for measuring local deformations on HRTEM images. The analysis of local deformations, *i.e.* strain analysis on HRTEM images, can be broadly classified with two types: peak-finding methods based on measuring the spacing of the image intensity between positions of maxima and minima and phase techniques. A detailed description of phase technique is provided in Chapter 7.

The peak-finding method is to simply calculate spacing of the lattice fringes with sub-pixel resolution in a given coordinate system by detecting pairs of intensity maxima. The variation of lattice spacing can give local deformation in a specific direction. Examples of the use of peak-finding methods include calculations of the cumulative sum (CUSUM) [30] demonstrated for a coherently strained $In_{0.82}Al_{0.28}Sb$/InSb superlattice layer and Lattice Fringe Spacing Measurements (LFSM) on the thick layers [31] and delta-doped layers [32] using regressional analysis in a superlattice. An advanced technique using the peak-finding method was demonstrated by Ourmazd *et. al.* [33] [34] and Rosenauer *et al.* [35]. They proposed a method that links both real and reciprocal space using real-space vector pattern recognition, providing a 2D map of local displacement. This method was

demonstrated with a Stranski-Krastanov-island structure to analyze strain on an atomic scale [36].

6.2 Regressional Analysis

Regressional analysis is one of the peak-finding methods and was developed to overcome the artifacts at heterointerfaces on HRTEM images for strain analysis. Regressional analysis utilizes rigid body displacement proposed by Dunin-Borkowski *et al.* [32]. Rigid body displacement is defined as the difference in lattice parameters between a strained layer and a perfect crystal, where measurement of the difference in lattice parameters is chosen far from the heterointerface. Hence, a major drawback of this method is that one can not directly interpret strain information at the heterointerface.

This approach involves extrapolating the lattice fringes from regions on either side of the layer towards it and then measuring the mismatch between them (See Figure 6.1). The specimen thickness, defocus and imaging conditions must be unchanged between the two regions of the image analyzed. Polynomial fits were used to determine the position of each peak. This method gives us rigid body displacement with monolayer accuracy. Figure 6-1 describes an example of the rigid body displacement. If we assume that the lattice constant of the reference regions is known and is 2Å as shown in Figure 6-1 (b), then the lattice constant of the strained layers (shadow region in Figure 6-1) is unknown and it is a value we desire to calculate. In order to utilize regressional analysis we must know the number of strained layers. In this example, we assume two monolayers of strained layers are embedded as shown in Figure 6.1. Dashed lines in Figure 6.1 indicate the positions of lattice planes in a perfect crystal that is extrapolated from the reference

regions toward the heterointerface. If measured mismatch between a dashed line and original lattice position far from the heterointerface is 0.4Å as illustrated in Figure 6.1, then we can conclude that the lattice contraction per each strained layer is 0.2Å because two strained layers contribute the total rigid body displacement (0.4Å), resulting in a lattice constant of each strained layer of 1.8Å.

Recently, groups [32] [37] have demonstrated local displacement at a few monolayers with small lattice-mismatched materials (f<3%) using regressional analysis. They calculated rigid lattice displacement. Dunin-Borkowski *et al.* [32] used silicon doped GaAs for strain analysis. Based on SIMS (Secondary Ion Mass Analysis) data, they used three different samples: 10.1 %, 4.8%, and 2.4% in silicon concentration. For example, the theoretical strain at the silicon doped layer of 10.1% (SIMS concentration) is around 0.74%. Hence, we can expect that strain analysis would not be able to reliably detect the 0.74% strain. In reality, their experimental results were 50~100 times larger than the predicted values. On the other hand, Liu *et al.* [37] investigated local displacement at a few monolayers with an $InAs_xP_{1-x}$/InP superlattice where theoretical strain at the $InAs_xP_{1-x}$ layer was around 1.8%. However, a large error occurred and additional Gaussian smoothing was applied to reduce this large error [37]. Hence, strain analysis using regressional techniques has major challenges in dealing with a few monolayers.

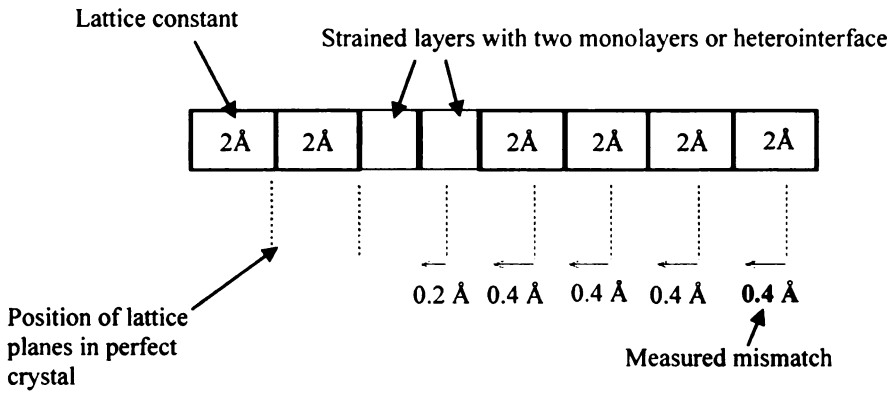

Figure 6.1: Schematic diagram showing a rigid lattice contraction across strained layers.

CHAPTER 7

PHASE TECHNIQUE

Efforts to minimize artifacts at heterointerfaces in HRTEM images, along with digital image processing, have provided the motivation to directly interpret strain information at strained layers or heterointerfaces with monolayer accuracy. Efforts to minimize artifacts in HRTEM images are addressed in Chapter 7.4 and Chapter 10. There have been two methods that show promise for the analysis of strain at heterointerfaces with monolayer accuracy. One is DALI (Digital Analysis of Lattice Images) software using peak-finding method proposed by Ourmazd *et al.* [33] [34] and Rosenauer *et al.* [36], and the other is geometric phase analysis (GPA), using the phase technique proposed by Hytch [38]. The advantage of these two methods is that they rapidly provide 2D mapping of strain information through digital image processing, while regressional analysis can only provide 1D mapping of strain information. In this research, the phase technique is used exclusively to implement strain analysis, as this is a more direct method than using the DALI software. In addition, the phase technique can be completely automated using software capable of digital image processing, such as Matlab®.

The phase technique implemented here utilizes a moiré pattern obtained via Fourier filtering. This approach provides highly sensitive measurement of local deformations on 2D images because the moiré pattern effectively magnifies local deformations, allowing

analysis of deformations with sub pixel accuracy. The phase technique can be separated into two methods: geometric phase analysis (GPA) [38] and Computational Fourier Transform moiré (CFTM) [2].

Fundamental investigations using the GPA method were initially conducted on rubber plates [39]. Subsequently, the GPA method was applied for HRTEM images by Hytch [38]. The theoretical background for applying the GPA method to HRTEM images is explained in Ref. [40], and several applications have been demonstrated on misfit dislocations (MDs) [41] [42]. In addition, it has been used for the determination of Burgers vectors [43], domain walls [40] [44], strained layers [44] [45] [46] [47], antiphase boundaries [48], carbon nanotubes [48], high-angle annular dark-field (HAADF) imaging [49], and strain fields at dislocations [50].

The fundamental work for the CFTM method was conducted on solder ball connect (SBC) assemblies [2]. The application of the CFTM method to HRTEM images has not been previously demonstrated, even though the CFTM method requires less memory for computation than that of the GPA method. This is achieved by avoiding unwrapping algorithms, including line-by-line scanning to detect the 2π discontinuities on the phase image in order to obtain strain distribution. Hence, we demonstrate the use of the CFTM method in this work. Mathematical works are introduced at Section 8.1 for comparison between GPA and CFTM.

7.1 Mathematical description for GPA and CFTM method

A HRTEM image is a discrete periodic image, and it can be expressed as a Fourier series. Under the condition of a perfect crystal, the image intensity with position **r** can be written as below [40]:

$$I(\mathbf{r}) = \sum_{n} H_n \exp(2\pi i \mathbf{g}_n \cdot \mathbf{r}), \tag{7.1}$$

where H_n is the Fourier coefficients of the image and n represents the index of a particular set of lattice fringes. The reciprocal vector, **g**, of a particular set of lattice fringes has a length equal to the reciprocal of the lattice fringe spacing. The direction of the reciprocal vector **g** is perpendicular to the lattice fringe. Subscript, g, represents each reflection, *i.e.* a particular set of sinusoidal lattice fringes. The reciprocal vector, **g**, of the particular set of lattice fringes has a length equal to the reciprocal of the lattice fringe spacing. The direction of the reciprocal vector **g** is perpendicular to the lattice fringe.

When deformations are present in an original image due to a displacement $\boldsymbol{u}(\mathbf{r})$, the following relationship exist [40]:

$$\mathbf{r} = \mathbf{r} - \boldsymbol{u}(\mathbf{r}) \tag{7-2}$$

The expression in Equation (7-1) becomes:

$$I(\mathbf{r}) = \sum_{n} H_n(\mathbf{r}) \exp\{2\pi i \mathbf{g}_n \cdot (\mathbf{r} - \mathbf{u}(\mathbf{r}))\}, \tag{7-3}$$

where the amplitude term, $H_n(\mathbf{r})$, is also position-dependent.

The digital diffractogram, $I(\mathbf{k})$, of the deformed image $I(\mathbf{r})$ can be obtained by Fourier transform:

$$I(\mathbf{k}) = \int_{A} I(\mathbf{r}) \exp\{-i2\pi \mathbf{g}_n \cdot \mathbf{r}\} d\mathbf{r}, \tag{7-4}$$

where A is the region of interest in the deformed image.

The expression in Eq. (7-4) can be expanded as below:

$$I(\mathbf{k}) = \int_A \sum_n H_n(\mathbf{r}) \exp\{i2\pi \mathbf{g}_n \cdot (\mathbf{r} - \mathbf{u}(\mathbf{r}))\} \exp(-i2\pi \mathbf{k} \cdot \mathbf{r}) d\mathbf{r}. \tag{7-5}$$

and then rewritten as follows:

$$I(\mathbf{k}) = \int_A \sum_n H_n(\mathbf{r}) \exp\{i2\pi \mathbf{g}_n \cdot \mathbf{r}\} \exp\{-i2\pi \mathbf{g}_n \cdot \mathbf{u}(\mathbf{r})\} \exp(-i2\pi \mathbf{k} \cdot \mathbf{r}) d\mathbf{r}. \tag{7-6}$$

$$I(\mathbf{k}) = \int_A \sum_n H_n(\mathbf{r}) \exp\{-i2\pi \mathbf{g}_n \cdot \mathbf{u}(\mathbf{r})\} \exp\{-i2\pi (\mathbf{k} - \mathbf{g}_n) \cdot \mathbf{r}\} d\mathbf{r}. \tag{7-7}$$

If a mask function **M(k)**, centered at a reflection in the digital diffractogram $I(\mathbf{k})$, is introduced, then a particular set of lattice fringes can be extracted from the HRTEM image, and displacement along a particular direction can be calculated. For instance, if a Mask function **M(k)** is centered at a reflection located on the *x*-axis in the digital diffractogram, lattice fringes along the *x*-direction are extracted from the HRTEM image, providing calculation of the displacement along the *x*-direction. If the reflection located at the *x*-axis is referred to as *gx*, then the digital diffractogram, $I_{gx}(\mathbf{k})$ is given by:

$$I_{gx}(\mathbf{k}) = I(\mathbf{k})\mathbf{M}(\mathbf{k}), \tag{7-8}$$

where the mask function **M(k)** has a value of one within the mask area and a value of zero outside of the mask area.

Equation 7-8 is equivalent to

$$I_{gx}(\mathbf{k}) = \int_A H_X(\mathbf{r}) \exp\{-i2\pi \mathbf{g}_x \cdot u_x(\mathbf{r})\} \exp\{-i2\pi (\mathbf{k} - \mathbf{g}_x) \cdot \mathbf{r}\} d\mathbf{r}, \tag{7-9}$$

where $\mathbf{g}_x$ and $u_x(\mathbf{r})$ are the reciprocal vector and the displacement located along the *x*-direction, respectively. $H_X(\mathbf{r})$ are the Fourier coefficients inside of the mask area.

If we subtract the factor $2\pi \mathbf{g}_x \cdot \mathbf{r}$, the perfect lattice frequency, from the digital diffractogram $I_{gx}(\boldsymbol{k})$ by substituting

$$\tilde{\mathbf{k}} = \mathbf{k} - \mathbf{g}_x \quad [2]. \tag{7-10}$$

then the expression in Eq. (7-9) can be replaced with

$$I_{gx}(\tilde{\mathbf{k}}) = \int_A H_X(\mathbf{r}) \exp\{-i2\pi \mathbf{g}_x \cdot u_x(\mathbf{r})\} \exp\{-i2\pi \tilde{\mathbf{k}} \cdot \mathbf{r}\} d\mathbf{r}, \tag{7-11}$$

and local atomic displacement $u_x(\boldsymbol{r})$ remains in the form of $2\pi \mathbf{g}_x \cdot u_x(\mathbf{r})$ in the phase term. The tilde $(\tilde{\mathbf{k}})$ indicates that the new digital diffractogram $I_{gx}(\tilde{\mathbf{k}})$ has a reflection (*i.e.* the reciprocal vector $\boldsymbol{g}_x$) that is shifted to the origin with a mask centered at the reflection in the digital diffractogram.

The expression in Eq. (7-11) is equivalent to

$$I_{gx}(\tilde{\mathbf{k}}) = F[H_X(\mathbf{r}) \exp\{-2\pi i \mathbf{g}_x \cdot u_x(\mathbf{r})\}] \tag{7-12}$$

The inverse Fourier transform of both sides of Eq. (7-12) results in a complex image given by

$$F^{-1}[I_{gx}(\tilde{\mathbf{k}})] = H_X(\mathbf{r}) \exp\{-2\pi i \mathbf{g}_x \cdot u_x(\mathbf{r})\} \tag{7-13}$$

If we define the right side of Eq. (7-13) as $M_g(\boldsymbol{r})$, then $M_g(\boldsymbol{r})$ is called the conventional moiré fringe [39] and can be expressed as

$$M_g(\mathbf{r}) = H_X(\mathbf{r}) \exp\{-2\pi i \mathbf{g}_x \cdot u_x(\mathbf{r})\} \tag{7-14}$$

The phase image $P_g(\boldsymbol{r})$ including values for local displacement $u_x(\boldsymbol{r})$ can be obtained by argument of Eq. (7-13) [39].

$$P_g(\mathbf{r}) = Phase\ [M_g(\mathbf{r})] = -2\pi \mathbf{g}_x \cdot u_x(\mathbf{r}) \tag{7-15}$$

$$= -\tan^{-1}\left(\frac{\mathrm{Im}\{F^{-1}[I_{gx}(\tilde{\mathbf{k}})]\}}{\mathrm{Re}\{F^{-1}[I_{gx}(\tilde{\mathbf{k}})]\}}\right) \tag{7-16}$$

The local displacement $u_x(\boldsymbol{r})$ can be defined as

$$u_x(\mathbf{r}) = -\frac{1}{2\pi|\mathbf{g}_x|} P_g(\mathbf{r}) \tag{7-17}$$

A one-dimensional strain distribution e_{xx} can be obtained from the phase image $P_g(\boldsymbol{r})$ by taking the derivative of the displacement, giving

$$e_{xx} = \frac{\partial u_x(\mathbf{r})}{\partial X} = -\frac{1}{2\pi|\mathbf{g}_x|}\frac{\partial P_g(\mathbf{r})}{\partial X} \tag{7-18}$$

This method is called geometric phase analysis (GPA); where the derivative is calculated numerically from the phase image ($P_g(\boldsymbol{r})$). Prior to taking the derivative, an unwrapping process on the phase image, $P_g(\boldsymbol{r})$, is required to remove discontinuities on the strain distribution.

In contrast, for the CFTM method, the gradient is applied to Eq. (7-13), resulting in

$$F^{-1}[i2\pi\tilde{\mathbf{k}} I_{gx}(\tilde{\mathbf{k}})] = -i2\pi\nabla\{\mathbf{g}_x \cdot u_x(\mathbf{r})\} H_X(\mathbf{r}) \exp\{-2\pi i \mathbf{g}_x \cdot u_x(\mathbf{r})\} \tag{7-19}$$

where the following differentiation theorem of Fourier transform was used:

$$F\{M(x)'\} = i2\pi\tilde{\mathbf{k}} M(\tilde{\mathbf{k}}) \tag{7-20}$$

Thus we obtain the expression:

$$\nabla\{\mathbf{g}_x \cdot u_x(\mathbf{r})\} = \frac{-F^{-1}[\tilde{\mathbf{k}} I_{gx}(\tilde{\mathbf{k}})]}{F^{-1}[I_{gx}(\tilde{\mathbf{k}})]} \tag{7-21}$$

Equation 7-21 is equivalent to

$$\nabla\{|\mathbf{g}_x| u_x(\mathbf{r})\} = \frac{-F^{-1}[\tilde{\mathbf{k}} I_{gx}(\tilde{\mathbf{k}})]}{F^{-1}[I_{gx}(\tilde{\mathbf{k}})]}, \tag{7-22}$$

because the reciprocal vector $\boldsymbol{g}_x$, the perfect lattice frequency, is constant.

Therefore, equation 7-22 is equivalent to

$$\nabla\{u_x(\mathbf{r})\} = \frac{F^{-1}[\tilde{\mathbf{k}} I_{gx}(\tilde{\mathbf{k}})]}{|\mathbf{g}_x| F^{-1}[I_{gx}(\tilde{\mathbf{k}})]}. \tag{7-23}$$

The x-direction derivative of the displacement $u_x(\boldsymbol{r})$, using directional derivatives, is e_{xx} and given by:

$$e_{xx} = \mathbf{n}_1 \cdot \nabla\{\mathbf{u}_x(\mathbf{r})\} = \frac{\partial u_x(\mathbf{r})}{\partial x} = \frac{-F^{-1}[\tilde{\mathbf{k}} \cdot \mathbf{n}_1 I_{gx}(\tilde{\mathbf{k}})]}{|\mathbf{g}_x| F^{-1}[I_{gx}(\tilde{\mathbf{k}})]} \tag{7-24}$$

where $\boldsymbol{n}_1$ is a unit vector along the x-axis. Therefore, the CFTM method does not use the phase image, $P_g(\boldsymbol{r})$, and it is a direct method to calculate the strain distribution. Since the CFTM method does not use the phase image, an unwrapping algorithm to remove phase discontinuities on the phase image, $P_g(\boldsymbol{r})$, is not required. (Compare Eq. (7-18) and (7-24)). Similarly, strain tensor of CFTM method can easily be calculated as below:

$$\mathbf{e}=\begin{pmatrix} e_{xx} & e_{xy} \\ e_{yx} & e_{yy} \end{pmatrix}=\begin{pmatrix} \dfrac{\partial u_x(\mathbf{r})}{\partial x} & \dfrac{\partial u_x(\mathbf{r})}{\partial y} \\ \dfrac{\partial u_y(\mathbf{r})}{\partial x} & \dfrac{\partial u_y(\mathbf{r})}{\partial y} \end{pmatrix}, \tag{7-25}$$

where rest of each component is

$$e_{xy}=\mathbf{n}_2\cdot\nabla\{\mathbf{u}_x(\mathbf{r})\}=\frac{\partial u_x(\mathbf{r})}{\partial y}=\frac{-F^{-1}[\tilde{\mathbf{k}}\cdot\mathbf{n}_2 I_{gx}(\tilde{\mathbf{k}})]}{|\mathbf{g}_x|F^{-1}[I_{gx}(\tilde{\mathbf{k}})]} \tag{7-26}$$

$$e_{yx}=\mathbf{n}_1\cdot\nabla\{\mathbf{u}_y(\mathbf{r})\}=\frac{\partial u_y(\mathbf{r})}{\partial x}=\frac{-F^{-1}[\tilde{\mathbf{k}}\cdot\mathbf{n}_1 I_{gy}(\tilde{\mathbf{k}})]}{|\mathbf{g}_y|F^{-1}[I_{gy}(\tilde{\mathbf{k}})]} \tag{7-27}$$

$$e_{yy}=\mathbf{n}_2\cdot\nabla\{\mathbf{u}_y(\mathbf{r})\}=\frac{\partial u_y(\mathbf{r})}{\partial y}=\frac{-F^{-1}[\tilde{\mathbf{k}}\cdot\mathbf{n}_2 I_{gy}(\tilde{\mathbf{k}})]}{|\mathbf{g}_y|F^{-1}[I_{gy}(\tilde{\mathbf{k}})]} \tag{7-28}$$

where $\boldsymbol{n_2}$ is a unit vector along the y-axis.

The digital diffractogram $I_{gy}(\tilde{\mathbf{k}})$ is obtained by a reflection whose an initial position is *y*-axis before shifting to origin in the digital diffractogram. The "$\mathbf{g}_y$" represents a reciprocal vector located in y-axis at the digital diffractogram.

For calculations with digital images the coordinates, ***r***, refer to the coordinates of pixels in the image. The reciprocal lattice vectors, $\mathbf{g}_x$ and $\mathbf{g}_y$, appear in the equations, are in pixels^{-1}. This means that the coordinates of the reciprocal lattice vectors in the numerical Fourier transform (with respect to the position k=0) must be divided by the size of the original image. Strain tensor equations for digital image processing for Matlab® are

$$e_{xx} = \mathbf{n}_1 \cdot \nabla\{\mathbf{u}_x(\mathbf{r})\} = \frac{\partial u_x(\mathbf{r})}{\partial x} = \frac{-F^{-1}[\frac{k_x}{N} I_{gx}(\tilde{\mathbf{k}})]}{\frac{|\mathbf{g}_x|}{N} F^{-1}[I_{gx}(\tilde{\mathbf{k}})]} \tag{7-29}$$

$$e_{xy} = \mathbf{n}_2 \cdot \nabla\{\mathbf{u}_x(\mathbf{r})\} = \frac{\partial u_x(\mathbf{r})}{\partial y} = \frac{-F^{-1}[\frac{k_y}{M} I_{gx}(\tilde{\mathbf{k}})]}{\frac{|\mathbf{g}_x|}{N} F^{-1}[I_{gx}(\tilde{\mathbf{k}})]} \tag{7-30}$$

$$e_{yx} = \mathbf{n}_1 \cdot \nabla\{\mathbf{u}_y(\mathbf{r})\} = \frac{\partial u_y(\mathbf{r})}{\partial x} = \frac{-F^{-1}[\frac{k_x}{N} I_{gy}(\tilde{\mathbf{k}})]}{\frac{|\mathbf{g}_y|}{M} F^{-1}[I_{gy}(\tilde{\mathbf{k}})]} \tag{7-31}$$

$$e_{yy} = \mathbf{n}_2 \cdot \nabla\{\mathbf{u}_y(\mathbf{r})\} = \frac{\partial u_y(\mathbf{r})}{\partial y} = \frac{-F^{-1}[k_y I_{gy}(\tilde{\mathbf{k}})]}{\frac{|\mathbf{g}_y|}{M} F^{-1}[I_{gy}(\tilde{\mathbf{k}})]}, \tag{7-32}$$

where N and M are size of an original image along x-direction and y-direction respectively with unit of pixel.

7.2 Interpretation of phase image

This section describes the meaning of phase fringes in a phase image so that we can interpret phase fringes in a phase image, $P_g(\boldsymbol{r})$, created from GPA method. The phase term, $\mathbf{g} \cdot \mathbf{u}(\mathbf{r})$, in a phase image varies between 0 and 1, resulting in the term $2\pi\mathbf{g} \cdot \mathbf{u}(\mathbf{r})$ varying between 0 and 2π. This is the reason a phase image $P_g(\boldsymbol{r})$ has 2π discontinuities on the phase image. Given a particular set of sinusoidal lattice fringes, *i.e.* a particular set of atomic planes, a reciprocal vector ($\boldsymbol{g}$) in a perfect crystal and a displacement vector $\boldsymbol{u}(\boldsymbol{r})$ can be drawn within a pair of atomic planes as shown in Figure 7-1. The length of

the reciprocal vector $\boldsymbol{g}$ is equal to 1/d, where d is the lattice fringe spacing in the reference region (*i.e.* perfect crystal). By trigonometry, the projection component of ***u(r)*** along a reciprocal vector $\boldsymbol{g}$ of the perfect crystal (*i.e.* reference lattice) is $|\mathbf{u}(\mathbf{r})|\cos\alpha$ as shown in Figure 7.1 and it can be written with the dot product since this is the projection of one vector on the other as:

$$|\mathbf{u}(\mathbf{r})|\cos\alpha = \frac{1}{|\mathbf{g}|}\mathbf{g}\cdot\mathbf{u}(\mathbf{r}) \tag{7-33}$$

Since the length of the reciprocal vector $\boldsymbol{g}$ is equal to the reciprocal of the lattice fringe spacing, d, in the perfect crystal (*i.e.* reference lattice), Eq. 7-33 is

$$|\mathbf{u}(\mathbf{r})|\cos\alpha = \frac{1}{|\mathbf{g}|}\mathbf{g}\cdot\mathbf{u}(\mathbf{r}) = \frac{1}{\frac{1}{d}}\mathbf{g}\cdot\mathbf{u}(\mathbf{r}) = d\mathbf{g}\cdot\mathbf{u}(\mathbf{r}). \tag{7-34}$$

In equation 7-34, the projection component of ***u(r)*** along a reciprocal vector $\boldsymbol{g}$ of the perfect crystal, varies between 0 and d as below:

$$0 \le d\mathbf{g}\cdot\mathbf{u}(\mathbf{r}) \le d. \tag{7-35}$$

By dividing by the lattice fringe spacing, d, and multiplying by 2π we obtain:

$$0 \le 2\pi\mathbf{g}\cdot\mathbf{u}(\mathbf{r}) \le 2\pi, \tag{7-36}$$

such that a cycle of phase fringes, 2π discontinuity, in a phage image appears whenever displacement on a HRTEM image is equal to the pitch of the reference lattice (*i.e.* lattice fringe spacing, d), if the center of a Bragg reflection is exactly shifted to the origin in the digital diffractogram.

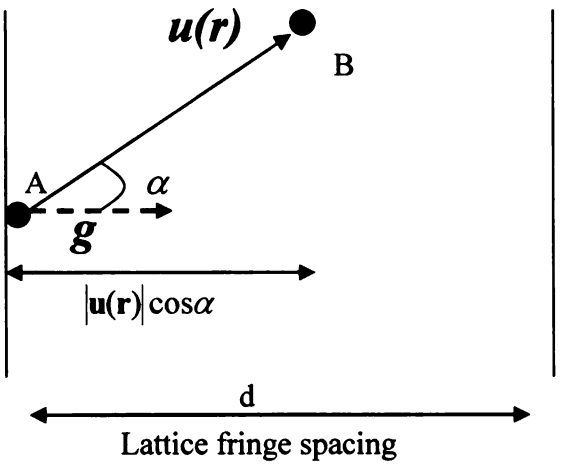

Figure 7.1: Schematic diagram of displacement field within a pair of atomic planes. Position A and B indicates an initial position and its position after deformation, which is represented by a displacement vector ***u(r)***. ***g*** is a reciprocal vector in perfect crystal. Projection component of ***u(r)*** along a reciprocal vector ***g*** of perfect crystal (*i.e.* reference lattice) is $|\mathbf{u}(\mathbf{r})|\cos\alpha$.

7.3 Previous applications with GPA method

The reason that it is called Geometric Phase Analysis is that phase reconstructed from the GPA method from HRTEM images does not correspond to the phase of the beams emerging from the specimen, but corresponds to the information associated with the positions of the fringes in the HRTEM images. In other words, the phase techniques such as the GPA and CFTM methods do not rely on knowledge of the positions of atomic columns in the crystalline specimen. It is based on the assumption of a constant spatial relationship between the positions of fringes in the HRTEM images and the positions of atomic columns in the crystalline specimen. The relationship between phase (P_{g1} and

P_{g2}) and displacement field (u_x and u_y) using two non-colinear Bragg reflections (g1 and g2) is [40]:

$$\begin{pmatrix} P_{g1} \\ P_{g2} \end{pmatrix} = -2\pi \begin{pmatrix} g_{1x} & g_{1y} \\ g_{2x} & g_{2y} \end{pmatrix} \begin{pmatrix} u_x \\ u_y \end{pmatrix} \tag{7-37}$$

$$\begin{pmatrix} u_x \\ u_y \end{pmatrix} = -\frac{1}{2\pi} \begin{pmatrix} g_{1x} & g_{1y} \\ g_{2x} & g_{2y} \end{pmatrix}^{-1} \begin{pmatrix} P_{g1} \\ P_{g2} \end{pmatrix}, \tag{7-38}$$

where g1x and g1y are the x-component and y-component of a reciprocal vector (g1). Similarly, g2x *and* g2y are the x-component and y-component of a reciprocal vector (g2). The strain field using the displacement field is expressed [40]:

$$\mathbf{e} = \begin{pmatrix} e_{xx} & e_{xy} \\ e_{yx} & e_{yy} \end{pmatrix} = \begin{pmatrix} \frac{\partial u_x}{\partial x} & \frac{\partial u_x}{\partial y} \\ \frac{\partial u_y}{\partial x} & \frac{\partial u_y}{\partial y} \end{pmatrix} = -\frac{1}{2\pi} \begin{pmatrix} g_{1x} & g_{1y} \\ g_{2x} & g_{2y} \end{pmatrix}^{-1} \begin{pmatrix} \frac{\partial P_{g1}}{\partial x} & \frac{\partial P_{g1}}{\partial y} \\ \frac{\partial P_{g2}}{\partial x} & \frac{\partial P_{g2}}{\partial y} \end{pmatrix}, \tag{7-39}$$

where the derivative is calculated numerically. Before taking the derivative, an unwrapping process is required to obtain the strain field.

Phase techniques can be used for various applications as well as determination of local displacement at strained layers [44] [45] [46] [47]. Strain field analysis on the domain wall in $PbTiO_3$ [40] demonstrated interchanging of lattice planes and rotation angles between two domains. Asymmetric abruptness of the interfaces at a GaAs/AlAs superlattice [45] was also demonstrated. It is also valuable to detect misfit dislocations, since abrupt phase changes in a phase image appear due to an additional lattice plane starting at the dislocations [50]. Other applications include calculating strain field on threading dislocations [42], edge dislocation [41], and boundaries of a quantum dot [51].

The dislocation core distribution tensor ($\tilde{\alpha}$) [43] can be calculated by further differentiation of the lattice distortion tensor (β) as below:

$$\tilde{\alpha} = -curl\ \beta = -curl \begin{pmatrix} \frac{\partial u_x}{\partial x} & \frac{\partial u_x}{\partial y} \\ \frac{\partial u_y}{\partial x} & \frac{\partial u_y}{\partial y} \end{pmatrix}$$

The tensor ($\tilde{\alpha}$) vanishes in the whole region except inside of the dislocation core where it forms characteristic peaks. Integration of the $\alpha_{ij}(x,y)$ values gives us calculation of in-plane Burgers vector, $b_i = -\int_{Sc} \alpha_{ij} ds$, where Sc is dislocation core surface. The determination of the Burgers vector can be used to calculate interaction of dislocations and information about the position of the maximum of the distortion at dislocations to determine the character of the dislocation core [43].

7.4 Efforts to minimize error for strain analysis

The phase technique and peak-finding methods such as cumulative sum (CUSUM) [30], Lattice Fringe Spacing Measurements (LFSM) [31], regressional analysis [32], and DALI (Digital Analysis of Lattice Images) [36] extract strain information based on positions of lattice fringes on a HRTEM image. However, the positions of fringes in the image do not have to correspond to atomic plane positions in a specimen. For instance, image contrast on HRTEM images depend on specimen thickness, spherical aberration, and lattice constant, etc. In order to minimize the difference between positions of atomic planes in a specimen and lattice fringes in the image, several efforts are suggested. An electron beam as large as possible is suggested to minimize electron-beam tilt [52]. A flat

response of the contrast transfer function (CTF) is required to transfer the identical phase. Achieving a flat response for the contrast transfer function (CTF) will also minimize inversion of contrast at interfaces where the structure varies rapidly. The best way to minimize delocalization [53] is to use spherical aberration corrected (Cs-corrected) transmission electron microscopy [54]. Contamination or amorphous surface layers at a specimen must be minimized. It should be noted that precise alignment of the electron microscope including current and voltage centering of the objective lens and correction of astigmatism at high magnification should also be performed. The efforts to minimize artifacts mentioned above will provide high-quality HRTEM images such that the atomic column positions on HRTEM images correspond to those of the crystal at a specimen.

CHAPTER 8

EXPERIMENTAL RESULTS

The primary objective of this chapter is strain analysis at the heterointerface of III-V ternary alloys with ultra-thin GaAsP/GaAs superlattices, which can be used for optical devices operating under the visible and IR spectrum. The motivation for strain analysis on the GaAsP/GaAs heterointerface is that strain analysis for this system has not been previously demonstrated due to the small strain value present. Such small lattice-mismatches increase the critical thickness of the films, which is the thickness above which dislocations are likely to occur. In this research effort, we address issues associated with strain measurement for small strain (f<3%) at heteroepitaxial films using the phase techniques known as the GPA and CFTM methods.

8.1 MBE growth and TEM studies

A superlattice with GaAsP/GaAs (190Å) was grown on a GaAs (001) substrate by MBE. The experimental details are provided in Ref. [55]. The results of HRXRD dynamical simulations revealed that the composition of the ultra-thin GaAsP was $GaAs_{0.86}P_{0.14}$. This sample was grown at 520°C with an As beam equivalent pressure (BEP) of 4×10^{-6} Torr and a Ga BEP of 1.5×10^{-7} Torr. The $GaAs_{0.86}P_{0.14}$ layer was

grown by exposing an As-stabilized GaAs surface to phosphorous for 50 seconds at a P_2 BEP of 4×10^{-6} Torr, producing a few monolayers. This process was repeated, resulting in a strained layer superlattice.

A TEM sample was prepared using the conventional cross-sectional method: grinding, dimpling, and Ar ion milling. Low angle (3°) Ar ion milling was used to obtain a comparatively uniform thickness over the superlattice. For the HRTEM imaging, a JEOL 2200FS equipped with double-tilt specimen holder, operating at 200kV, was used with Cs=0.5 mm, where the point resolution is 0.19nm.

8.2 Ultra thin $GaAs_{0.86}P_{0.14}$ layer embedded in GaAs: Theoretical values of strain

The lattice constant parallel to the growth direction for the $GaAs_{0.86}P_{0.14}$ layer can be calculated using the Vegard's law approximation:

$$a_{GaAs_{0.86}P_{0.14}} = a_{GaAs} - x_P(a_{GaAs} - a_{GaP}), \tag{8-1}$$

where x_p is phosphorus composition and equal to 0.14. The lattice constants a_{GaAs} and a_{GaP} are 0.565nm 0.545nm, respectively. Hence, the lattice constant parallel to the growth direction for the $GaAs_{0.86}P_{0.14}$ layer is 0.5622nm. Lattice distortion components parallel to the growth direction, *i.e.* theoretical strain e_{xx}, can be defined as below:

$$e_{xx} = \frac{a_2 - a_1}{a_1} = \frac{a_{Ga0.86As0.14} - a_{GaAs}}{a_{GaAs}} = \frac{a_{\perp} - a_{GaAs}}{a_{GaAs}}, \tag{8-2}$$

where a_2 and a_1 are the lattice constants parallel to the growth direction for the $GaAs_{0.86}P_{0.14}$ layer and GaAs, respectively.

Under the assumption of pseudomorphic growth, the $GaAs_{0.86}P_{0.14}$ layer is further constrained to match the host lattice at GaAs in the plane parallel to the interface as predicted by elasticity theory. Thus the lattice parameter of the $GaAs_{0.86}P_{0.14}$ layer in a direction parallel to the growth direction is given by:

$$a_{\perp} = a_{GaAs} - \frac{1+\upsilon}{1-\upsilon}(a_{GaAs} - a_{GaAs_{0.86}P_{0.14}}), \tag{8-3}$$

where υ is Poisson's ratio and $(1+\upsilon)/(1-\upsilon)$ is a factor of contraction (or extension) of the unit cell in a direction parallel to the growth direction when the unit cell parallel to the interface direction is extended (or contracted) due to coherent strain[56]. The reason that we include the factor, $(1+\upsilon)/(1-\upsilon)$ is that the biaxial in-plane tensile strain, due to the GaP bonding, results in a uniaxial compressive stress along the growth direction at the $GaAs_{0.86}P_{0.14}$ layer, such that we can presume that the superlattice is deformed tetragonally [57]. Poisson's ratio for both GaAs [58] and GaP [59] is 0.31. In Eq. (8-3), we ignored surface relaxation of the strained layer for cross-sectional TEM because the strained layer we investigated was one period of a 10-period superlattice grown near the substrate and capped with a GaAs layer. Furthermore, the thickness of the $GaAs_{0.86}P_{0.14}$ layer is very small (< 6Å) with respect to that of the GaAs superlattice. Consequently, the lattice constant parallel to the growth direction of the $GaAs_{0.86}P_{0.14}$ layer is 0.559nm

when considering elasticity theory. Hence, the lattice distortion component parallel to the growth direction e_{xx} is given by -1.0% using Eq. (8-2).

8.3 Strain analysis using the CFTM method

A low magnification image of a superlattice with GaAsP/GaAs (190Å) grown on a GaAs (001) substrate is shown in Figure 8-1 (a). The cross-sectional HRTEM image taken along [110] zone axis is given in Figure 8-1 (b). The resolution is 7 pixels/ (002) lattice fringe. The ultra-thin $GaAs_{0.86}P_{0.14}$ layer is located in the middle of this image. By comparing the HRTEM image with electron microscopy software (EMS) [60], where EMS is software for simulation and analysis of HRTEM images, the white spots in the HRTEM image were determined to be columns of Ga and As pairs. Arrows on the HRTEM image depict the growth direction (x-direction) and the interface direction (y-direction). The heterointerface was grown coherently with strained layers because the lattices are well aligned. Hence, we can assume that the strained layer is tetragonally distorted, *i.e.* a pseudomorphic layer [57] [61]. In addition, we can expect that the profile of phosphorus will affect local deformations at the strained layer, since phosphorus will be diffused into the GaAs layers.

As can be judged from Figure 8-1 (b), the HRTEM system at our disposal cannot provide chemical contrast for $GaAs_{0.86}P_{0.14}$ on GaAs because the difference in projected potential between $GaAs_{0.86}P_{0.14}$ and GaAs is small and structural variation does not take place across $GaAs_{0.86}P_{0.14}$ layers. Since contrast in Figure 8-1 (b) does not directly relate to the presence of phosphorus, the phase technique independent of the image contrast can

be used to detect $GaAs_{0.86}P_{0.14}$ and obtain strain distribution through the difference of lattice constants across the layers.

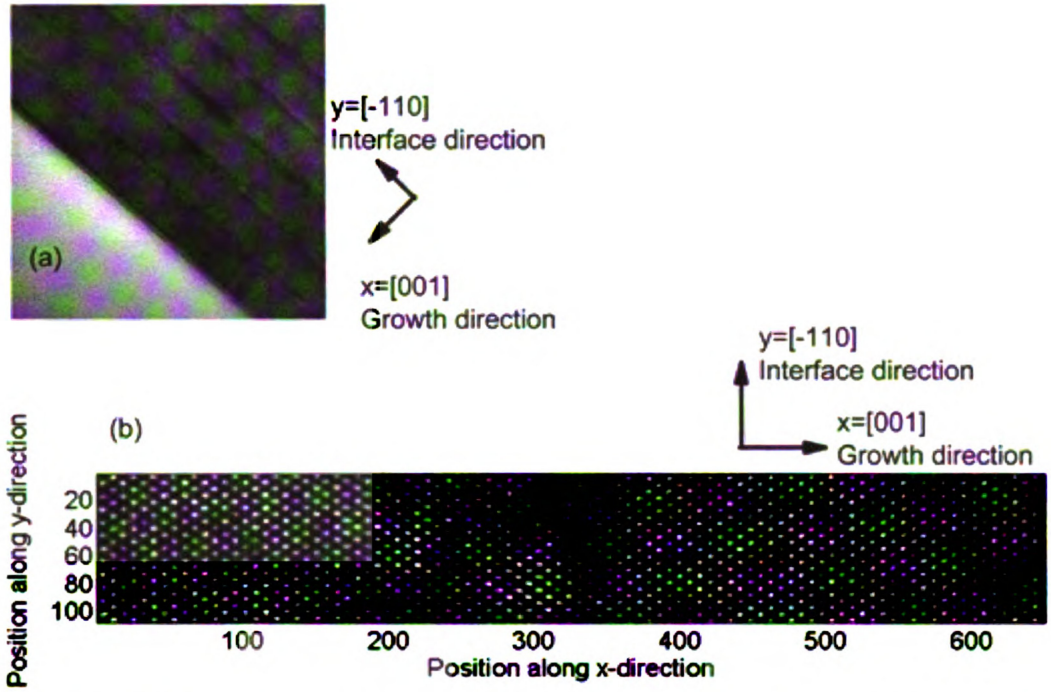

Figure 8.1: TEM images viewed on [110] ZA. (a) A cross-sectional TEM image with low magnification of a strained $GaAs_{0.86}P_{0.14}$/GaAs superlattice. (b) A cross-sectional HRTEM image (XTEM) of a strained $GaAs_{0.86}P_{0.14}$ /GaAs heterointerface taken along [110] zone axis. Image size is 108 by 650 pixels and magnification is 0.031nm/pixel (Instrumental magnification of 600,000×).

The CFTM method was applied to evaluate strain on the HRTEM image. All work related with strain analysis in this research has been implemented using Matlab®. In the first stage, the original image was Fourier-transformed to obtain the digital diffractogram $I(\boldsymbol{k})$ as shown in Figure 8-2. Since in practice, local deformations along the growth direction (x-direction) are the primary concern, an (002) reflection should be chosen, as it is the first harmonic along the x-direction and has the largest intensity.

In the second stage, Fourier filtering using a Gaussian mask centered at the (002) reflection was performed. The Gaussian mask [40] we used is below,

$$M(\tilde{\mathbf{k}}) = \exp\{-4\pi \frac{k^2}{g^2}\} \tag{8-4}$$

and the mask size is $g_{002}/3$.

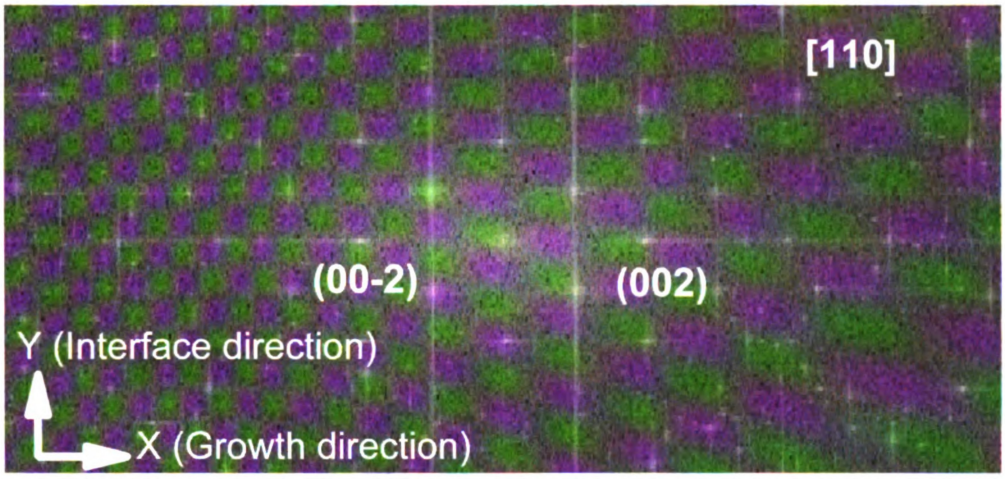

Figure 8.2: A digital diffractogram of the original HRTEM image in Figure 8-1(b).

Figure 8-3 shows the strain profile (e_{xx}) obtained using Eq. (7-24). This profile was vertically averaged along the direction parallel to the interface from a 2D strain image (not shown here). Vertical averaging from a 2D strain image allows randomly distributed noise on the image to be minimized. In Figure 8-3, we can clearly see two regions where overshoot occurs. These overshoots are exhibited as a rippled appearance [46] and provide evidence of the presence of a strained layer [46] because overshoot and undershoot are typical phenomena that occur at strained layers. In addition, fluctuations are present in the reference regions (GaAs layers). It is not feasible to determine what

created the fluctuations in the reference regions. However, we consider fluctuations of ±0.7 % to be within an acceptable range for the reference region.

The results of Figure 8-3 show a lattice contraction of -4.9% at the strained $GaAs_{0.86}P_{0.14}$ layers in the (001) direction. This is around five times larger than the theoretical value (-1%) determined in the Chapter 8.2. To understand what causes this large error from the initial estimate, we can assume that error comes from the phase technique because accuracy of the phase technique at ultra-thin layers with small strain has not been demonstrated. Error from the phase technique is address in Chapter 9.

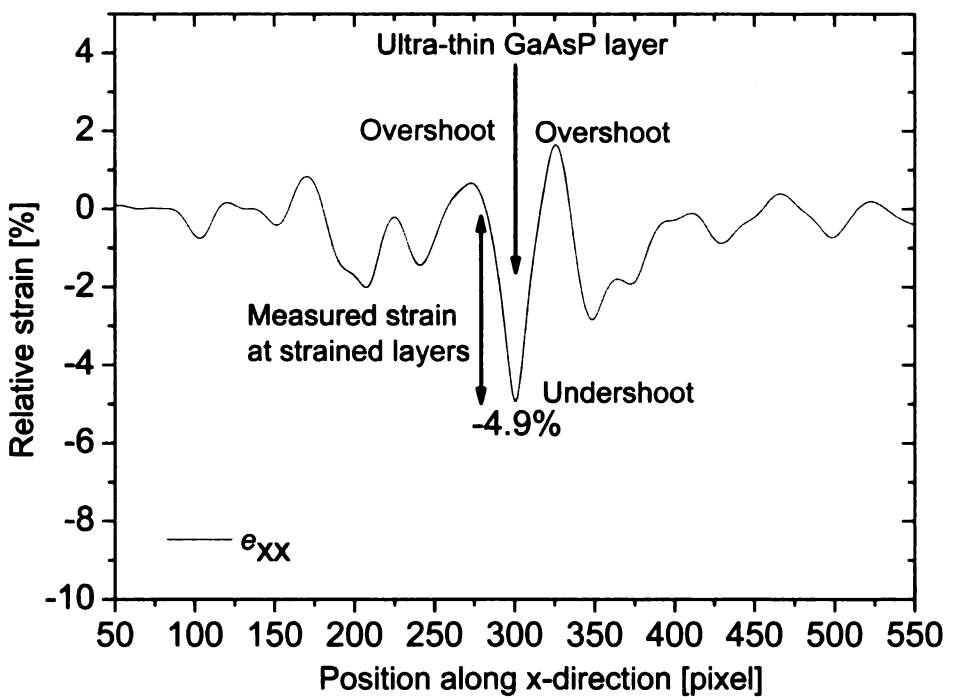

Figure 8.3: Strain profile (e_{xx}) using the CFTM method of the experimental HRTEM image with mask size ($g_{002}/3$).

Before investigating error from the phase technique, strain at the $GaAs_{0.86}P_{0.14}$ layers of the HRTEM image was measured as a function of mask size. During the Fourier filtering, mask size will determine the rippled appearance (overshoot and undershoot) of the strain profile because the mask size is related with the effective spatial and spectral resolution. Therefore, smoother strain profiles can be obtained with reduced mask size; thus we gain spatial information but at the cost of lost spectral resolution [46]. However, it should be noted that we are primarily concerned with the strain at the center of the strained layers instead of sharpness of the strain profile across the strained layers. Hence, we do not have to be concerned with the spectral resolution in this research. It is worth restating that the strain at the center of the strained layers can be studied by reducing the mask size in order to remove error in the form of rippled appearance such as overshoot and undershoot. One weakness to this approach is that we may not detect asymmetry of the strain profile due to the small mask size, if it exists at the strained layers. Asymmetry of the strain profile is plausible due to asymmetry of the phosphorous composition along the growth direction, which occurs when phosphorus is primarily diffused into the GaAs.

Characterization of error at $GaAs_{0.86}P_{0.14}$ strained layers has been investigated according to mask size. Figure 8.4 (a) shows the measured strain at $GaAs_{0.86}P_{0.14}$ strained layers according to mask size, where the radius of a Gaussian mask was varied (See *x*-axis of Figure 8.4 (a)). A mask size of g/3 and g/2 corresponds to a radius of 30 and 45 pixels, respectively. The radius of the Gaussian mask is plotted from 3 to 40 pixels. It was observed that the magnitude of the measured strain is linearly increasing with mask size in region-3. The discrepancy of measured strain at GaAsP strained layers

(*i.e.* -4.9% at g/3 mask size) is caused by undershoot (See Figure 8.3). We can assume then that region-3 is primarily due to error in the form of a rippled appearance.

In addition, Figure 8.4 (a) shows that the measured strain gradually approaches -1.5% at region-1 and saturates for a while at region-2. The cause of saturation (region-2) in Figure 8.4 (a) can be explained by the following observation: measured strain at strained layers is saturated when the radius of the Gaussian mask is close to the actual radius of the (002) reflection, *i.e.* around 12~15 pixels in this case. The cross-sectional profiles of the (002) reflection are shown in Figure 8.4 (b) for estimate of size of the (002) reflection. This implies that the strain information ranges over the width of the (002) reflection. Therefore, the assumption that error occurred and contributed to the result of Figure 8.3 is valid, and the error could be removed using a smaller mask size. The resulting measured strain at $GaAs_{0.86}P_{0.14}$ strained layers would be around 1.5% lattice contraction. We emphasize here that error in the form of rippled appearance, which is linearly dependent on mask size, has not been previously reported. We suggest that this error is related to the Fourier leakage effect, which is demonstrated through image simulations at Chapter 9.

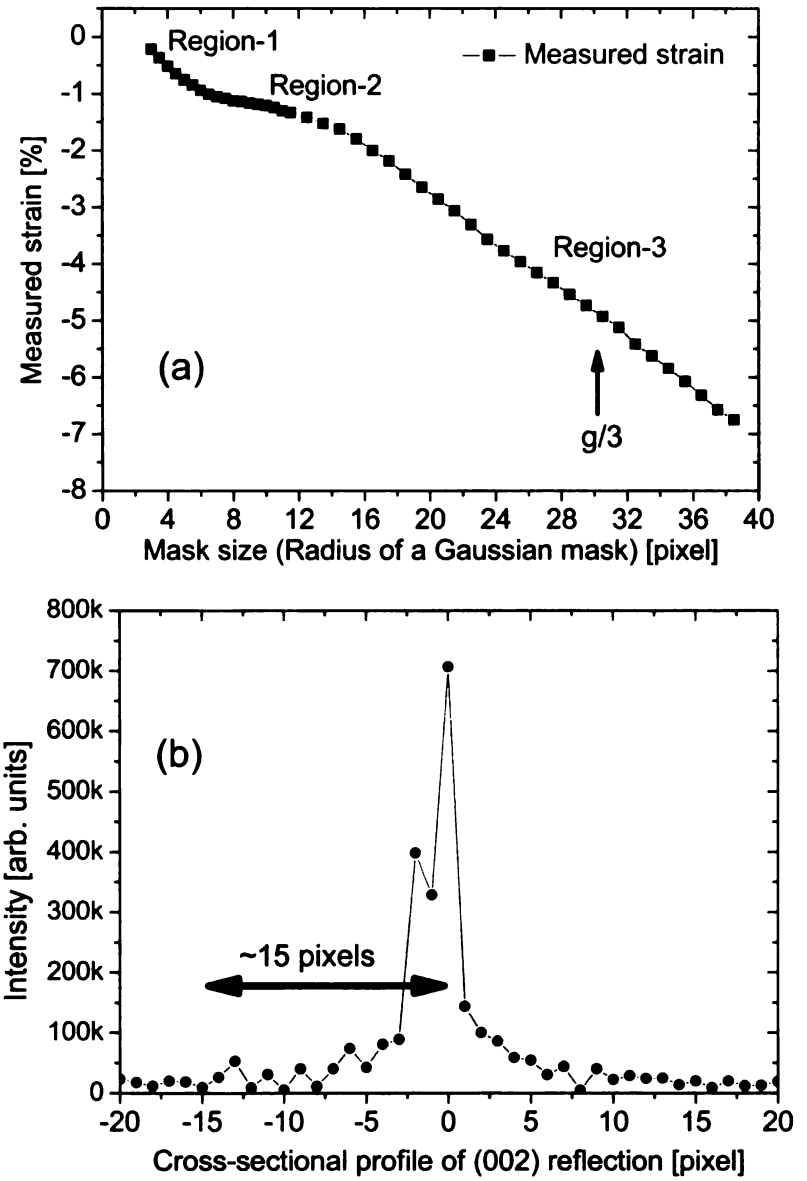

Figure 8.4: (a) Measured strain at the $GaAs_{0.86}P_{0.14}$ layers according to mask size. The x-axis is the radius of the Gaussian mask. (b) A cross-sectional profile of the (002) reflection along the x-direction. The radius of the (002) reflection, along the x-direction is around 15 pixels.

CHAPTER 9

IMAGE SIMULATIONS

Our experimental results revealed that the measured strain linearly increases with increasing mask size. Further details on error, when the phase technique is applied, can be divided into two types: alias effect and leakage effect. The alias effect is related with sampling. The phase technique starts with a digitized image that is taken using a Charge Coupled Device (CCD) in the image plane of a microscope. Therefore, lattice planes in a specimen are sampled with a CCD camera, resulting in lattice fringes on HRTEM images. Typical resolution of the CCD camera is 1024 by 1024 pixels in the field of view. When the sampling frequency during digitization of a CCD camera is smaller than the Nyquist frequency, the alias effect can occur. However, we found that the alias effect does not occur if fringe spacing is larger than three pixels. Therefore, the reason for error linearly increasing with increasing mask size can be related with the leakage effect, since the leakage effect cannot be avoided when the phase technique is applied.

9.1 Leakage effect

The leakage effect is associated with the Fourier transform and cannot be avoided. Therefore, the leakage effect limits accuracy of the phase technique since the phase technique utilizes Fourier transform. The leakage effect occurs when the size of an image

is not an integer multiple of the pitch of the periodic crystal structure in the original image. Since most HRTEM images are not commensurate, where commensurate means an integer number of periods of the crystal structure fit within the field of view. The leakage effect causes a spectral "smear" located about a center frequency, along with spurious high frequency noise in the spectral space that results in rippled appearance such as overshoot and undershoot, where the lattice constant abruptly changes in the spatial domain. We demonstrate the rippled appearance caused by the leakage effect using computer-generated images to investigate error from the phase technique. We have simulated and measured the strain as a function of mask size for two cases of lattice contraction: 2% and 10%.

9.2 Impact of the leakage effect

Figure 9.1 shows a one-dimensional lattice fringe constructed using a sinusoidal function, where the image resolution is the same as Figure 9-1 (*i.e.* 7 pixels per fringe spacing). In addition, the image size for all simulations in Chapter 9.2 is the same as the experimental image in Figure 9-1 (108 by 650 pixels). The pitch along the x-direction is different at unstrained and strained layers. The pitch of unstrained layers (reference region) and strained layers are 7 pixels and 6.86 pixels, respectively. This represents a 2% lattice contraction at the strained layers along the *x*-direction. The strained layers have two monolayers and are placed in the middle of the image as shown in Figure 9-1.

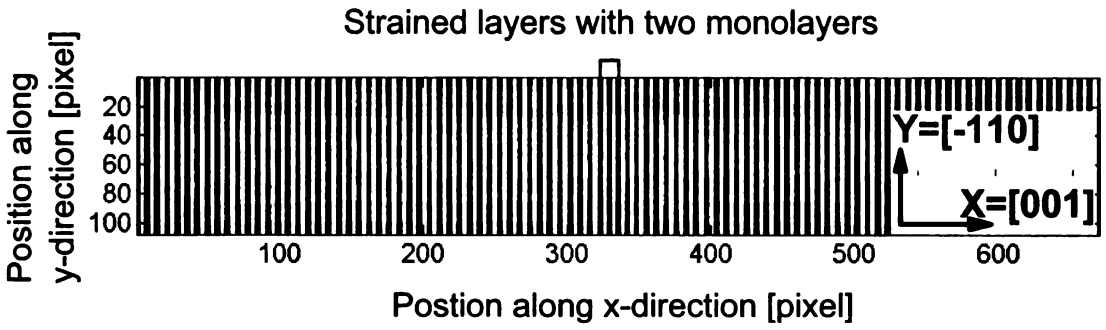

Figure 9.1: Computer-generated lattice fringes using sinusoidal functions. Arrows indicate coordinate system of x and y axes, corresponding to growth and interface directions of Figure 1. A digital diffractogram is shown in the inset. The inset shows the first harmonic on the x-axis that can be used for strain analysis using the phase technique.

In implementing the phase technique for strain analysis, the same procedures have been conducted using the first harmonic shown in the inset of Figure 9.1. Figure 9.2 shows e_{xx} profiles using the CFTM method according to different mask sizes when the lattice constants of strained layers positioned in the middle of an original image are 2% and 10% smaller than the reference region. The mask size was varied up to g/2 for a Gaussian mask. We observed a large discrepancy for the measured strain in the case of 2% lattice contraction as shown in Figure 9.2 (a) in the form of undershoot. In order to clearly see the measured strain as a function of mask size, strain was measured with different mask sizes for 2% and 10% lattice contraction.

Figure 9.3 and Figure 9.4 show the measured strain in the case of 2% and 10% lattice contraction, along with the effects of different image resolutions. The mask size was varied up to g/2 with a Gaussian mask. Different image resolutions (number of pixels per fringe spacing) were plotted together. It should be noted that as we increase

magnification of a microscope, *i.e.* enlargement of the fringe spacing or improvement of image resolution on HRTEM images, reflections will move towards the origin in reciprocal space for images having the same size. Therefore, the magnitude of a reciprocal vector $\boldsymbol{g}$ (distance between origin and a reflection in reciprocal space) is smaller and smaller as we improve image resolution of the HRTEM images. In fact the magnitude of a reciprocal vector $\boldsymbol{g}$ is equal to the reciprocal of the fringe spacing. Therefore, the magnitude of $\mathbf{g}/2$ gets smaller and smaller with increasing image resolution (number of pixels per fringe spacing) as shown in Figure 9.3 and Figure 9.4, where the mask size (Gaussian radius) was varied from 4 pixels to g/2.

First, we observed that the linear dependence of error as a function of mask size occurs only for the small strained (2% lattice contraction) systems as shown in Figure 9.3 (a). Error in the form of undershoot should be caused by phase technique because artifacts from an electron microscope are not included in the simulated images. It verifies that the leakage effect during digital image processing creates error when the phase technique is applied for strain analysis of small-strained systems at ultra-thin layers.

One way to minimize the leakage effects linear dependence on mask size is to increase the image resolution. We can clearly see that the error is reduced with increasing resolution of the image, as shown in Figure 9.3 (a). This demonstrates that the spurious high frequency term in the spectral domain due to the leakage effect can be minimized with an increase of image resolution.

Second, we can see that saturation occurs in region-2 when the mask size is close to the size of the first harmonic, *i.e.* 15 pixels, as shown in Figure 9.3 (a) and (b). The cross-sectional profiles of the first harmonic are shown in Figure 9.3 (b) for estimate of size of

the first harmonic. This implies that the strain information is mainly positioned at or near the center of the first harmonic.

From comparative analysis of Figure 9.3 (a) and Figure 8.4 (a), it is observed that the leakage effect at the $GaAs_{0.86}P_{0.14}$ strained layers contributed to the linearly dependent error for mask sizes in region-3 of Figure 8.4 (a). Clearly, the leakage effect dominates for small-strained systems (f<3%) when the image resolution is 7 pixels per fringe spacing. In order to reduce error at the strained layers, one can increase the image resolution. Otherwise, only higher strained systems can use a resolution of 7 pixels per fringe spacing for reliable analysis as shown in Figure 9.4 (a). At 10% lattice contraction of the strained layers, reliable results were obtained with an image resolution of 7 pixels per fringe spacing. An alternate way to interpret small strain values for HRTEM images with 7 pixels per fringe spacing is to reduce the mask size until mask size is close to the size of the first harmonic used for phase technique because the strain information is mainly positioned at or near center of the first harmonic. To sum up, we conclude that strain of the $GaAs_{0.86}P_{0.14}$ strained layers would be around -1.5% at Figure 8.4 (a) using the alternate way (*i.e.* reducing mask size until it reaches size of (002) reflection) to eliminate spurious high frequency term caused by leakage effect. However, more work is needed to determine accuracy of the phase technique when mask size is reduced until size of the first harmonic in reciprocal space. This is the best way to increase image resolution to determine small strain at ultra-thin layers when the phase technique is applied.

Now we compare strain analysis between the CFTM method and the GPA method on the $GaAs_{0.86}P_{0.14}$/GaAs heterostructure. In order to directly compare the CFTM and

GPA methods, strain profiles from both techniques are plotted together as shown in Figure 9.5. From Figure 9.5, we can clearly see that the two profiles are exactly matched such that the CFTM method is confirmed experimentally by excellent agreement between the CFTM and GPA methods.

9.3 Reliability of phase technique

Strain analysis at heterointerfaces that generally are composed of a few monolayers requires methodology having capability to interpret monolayer accuracy. Therefore, after the phase technique for HRTEM images was developed in 1993, the primary concern has been the reliability of the phase technique in monolayer accuracy for strain analysis at heterointerfaces. However, reliability of the phase technique in monolayer accuracy has not been investigated yet. In this research, error of the phase technique is quantified for monolayer accuracy. Two monolayers of strained layers were constructed using Matlab® assuming that in-plane lattice constant (y-direction) is matched and lattice constant of growth direction (x-direction) is strained such as coherent growth. Strained layers of two monolayers are inserted in the middle of an image (See Figure 9.6). The procedures used to produce the image simulations are provided in the following Section 9.3.1.

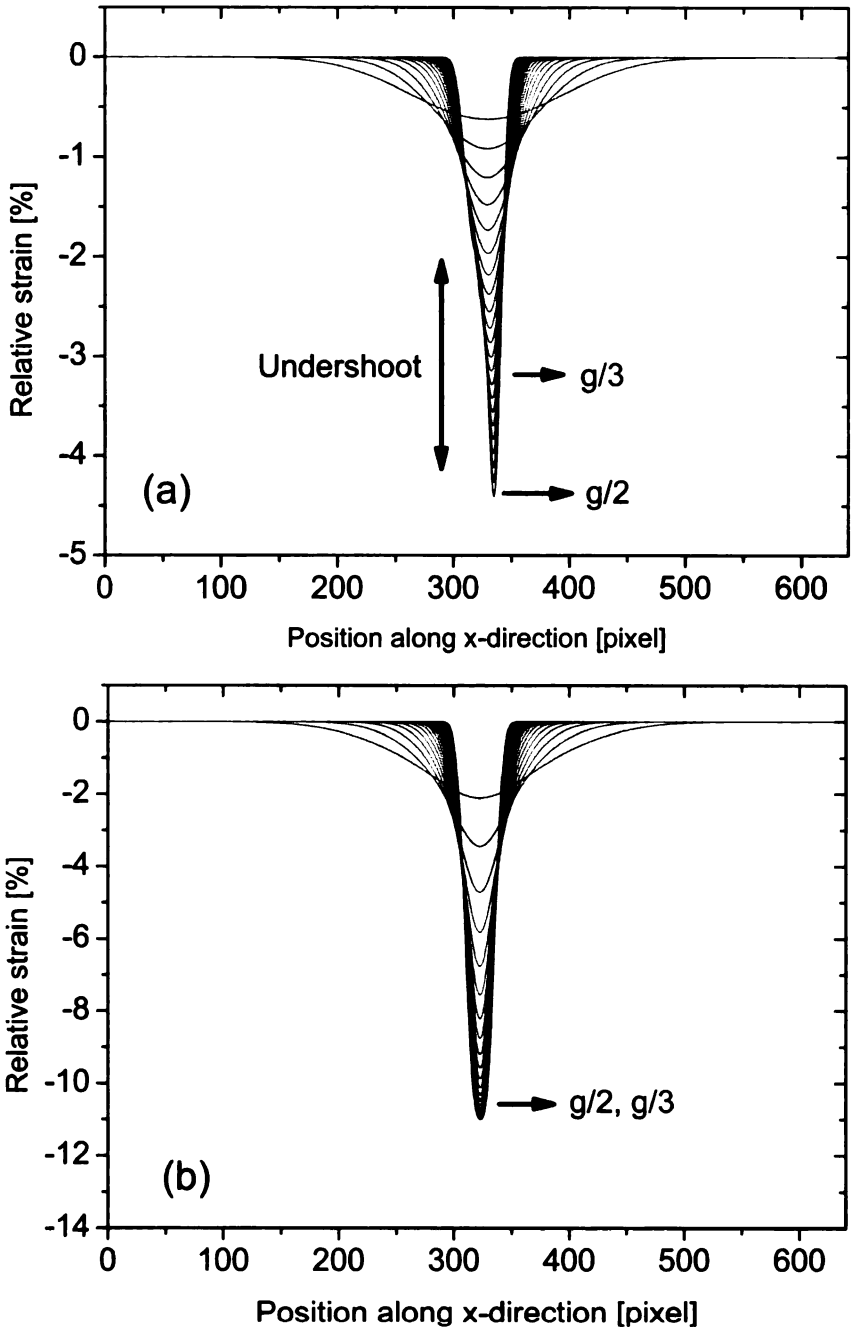

Figure 9.2: Strain profile, e_{xx}, of the simulations for (a) 2% and (b) 10% lattice contraction at strained layers with two monolayers. Image resolution is 7 pixels per lattice fringe spacing.

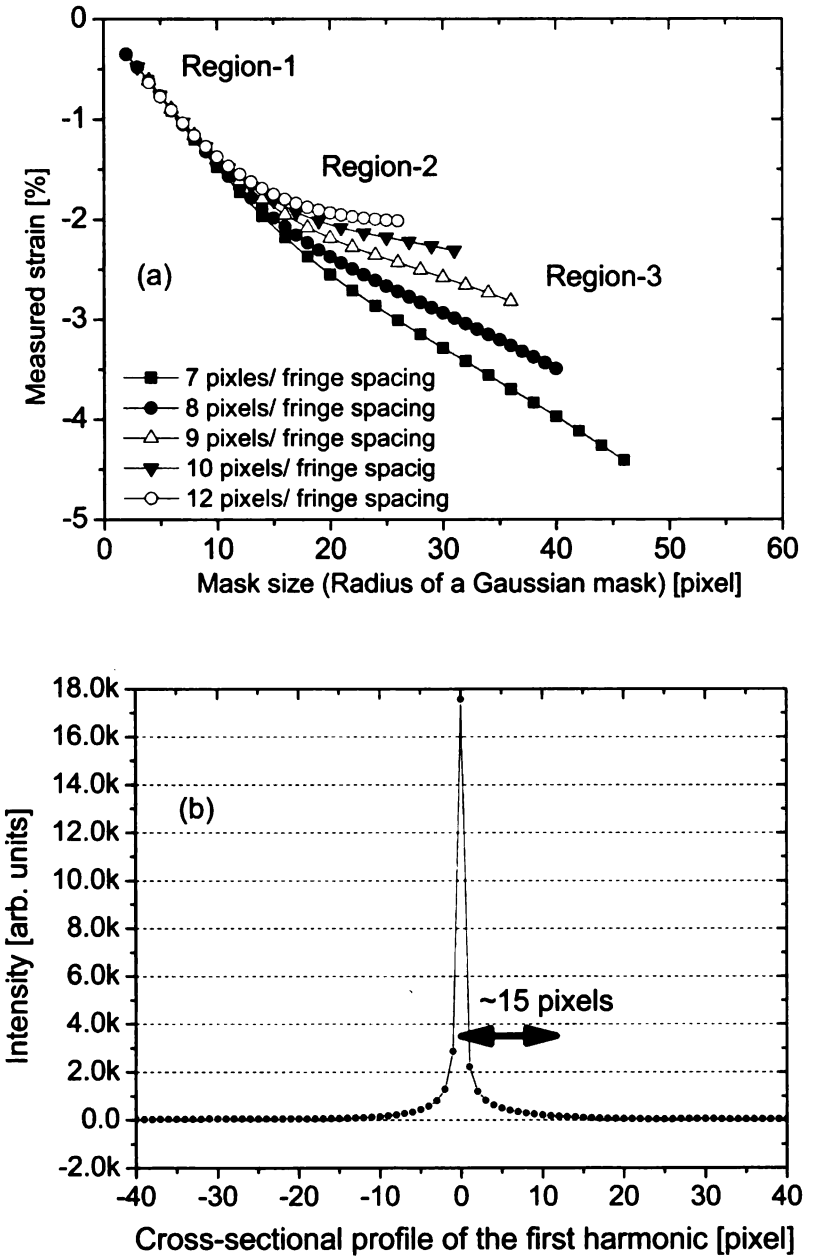

Figure 9.3: (a) Measured strain according to mask size and image resolution (number of pixels per fringe spacing) when applied strain at two monolayers of strained layers is -2%. (b) A cross-sectional profile of the first harmonic used for phase technique.

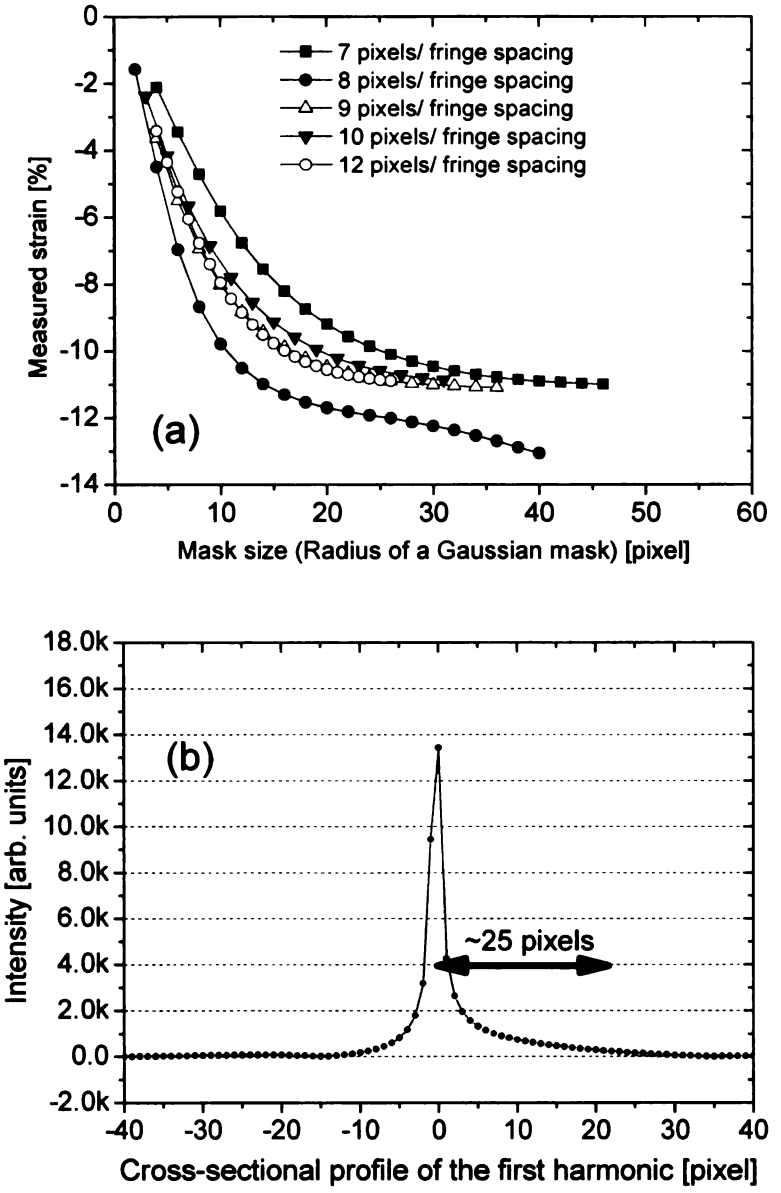

Figure 9.4: Measured strain according to mask size and image resolution (number of pixels per fringe spacing) when applied strain at two monolayers of strained layers is -10%. (b) A cross-sectional profile of the first harmonic used for phase technique.

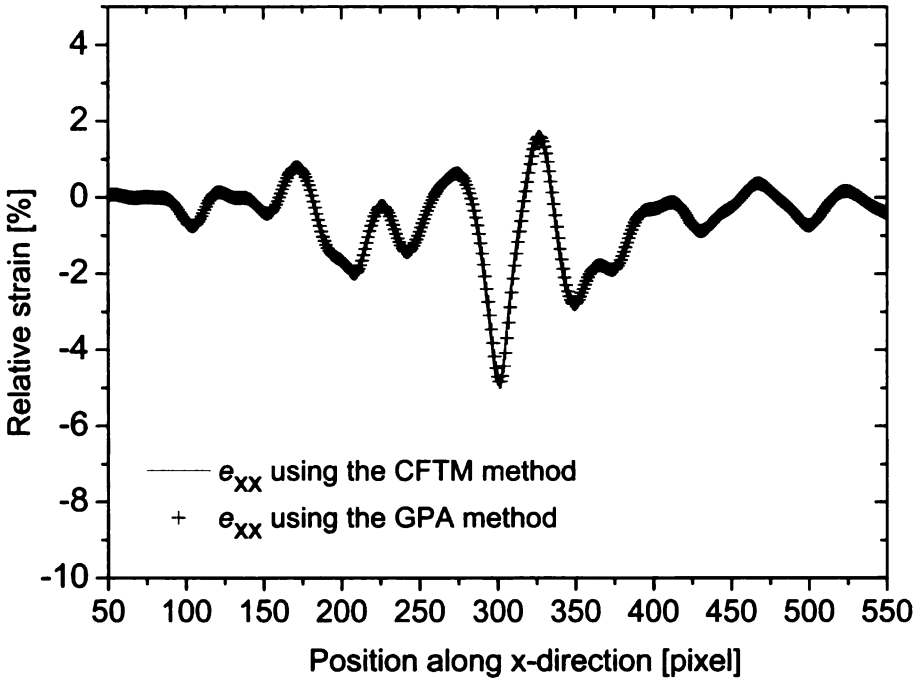

Figure 9.5: Comparison of strain profiles on the GaAsP/GaAs heterostructure using CFTM and GPA method.

9.3.1 Procedures of image simulations

In this research, a simulation method using Matlab® for determining errors of the strain values when the phase technique is applied has been proposed and the error of phase technique was quantified. While the image size of all images for simulations was maintained with around 620 by 620 pixels, two parameters are applied on a 2D lattice image generated with Matlab® for simulations to determine errors of the strain values with phase technique. One is a value of applied strain at strained layers with respect to the reference regions on a 2D lattice image and the other is image resolution (pixels per fringe spacing). In these simulations, the parameter of image resolution was applied between 7 and 12 pixels because, in practice, the resolution (number of pixels per fringe

spacing) of a HRTEM image depends upon the lattice constant of the crystal structure and is generally between 7 and 12 pixels per fringe spacing (See Table 9.1). The following procedures describe steps for the simulation method and coding of the simulation method is provided at appendices B and C.

Step 1: An image with a 2D lattice was generated using a sinusoidal function along both x and y directions, resulting in crossing lattice fringes displaying dot contrast (See Figure 9.6 (a)). Pitches along the y-direction are constant over the image. Pitches along the x-direction are different at unstrained and strained layers. The pitch of unstrained layers (reference region) and strained layers are 20 pixels and 18 pixels respectively. This represents a 10% lattice contraction at strained layers along the x-direction. The strained layers are placed in the middle of the image as shown in Figure 9.6 (a). The image size is 620 by 620 pixels.

Step 2: Fourier transform was performed on the original image, resulting in a digital diffractogram shown in the inset of Figure 9.6 (a).

Step 3: Fourier filtering on the diffractogram was performed using a Gaussian mask centered on the first harmonic placed along x-direction for e_{xx}. The first harmonic was marked with rectangular box.

Step 4: The Bragg-filtered lattice fringe, shown in Figure 9.6 (b), was obtained by inverse Fourier transform using the first harmonic without shifting the first harmonic to the origin in the diffractogram. An unwrapped phase image $P_g(X)$ was obtained using GPA method as shown in Figure 9.6 (c).

Step 5: Strain profile e_{xx} shown in Figure 9.7 was obtained using Eq. 7.24 where g/3 was

selected for mask size of a Gaussian function in reciprocal space. A Gaussian mask provides a smoothing effect in real space such that the strain profile is not sharp compared with a theoretical profile (See Figure 9.7). The ringing effect or rippled appearance that occurs in the spatial domain when we use the phase technique is caused by abrupt spectral truncation in the frequency domain such as circular, rectangular or diamond mask with sharp edges. It can be eliminated by use of a more gradual attenuation such as a Gaussian mask, resulting in no rippled appearance in Figure 9.7. A Gaussian mask loses high-frequency detail, leading to rounded edges; however, a Gaussian mask is suggested to remove ring effect or rippled appearance for monolayer accuracy.

Step 6: Finally, values of measured strain were determined through various simulations in terms of applied strain at strained layers and image resolution (*i.e.* number of pixels per fringe spacing) and summarized in Figure 9.10 and Table 9.2.

Table 9.1: Estimate of (002) fringe spacing when a GaAs specimen is viewed along [110] direction with Jeol 2200FS. Field of view is also provided.

Instrumental magnification (Jeol 2200FS)	(002) fringe spacing (pixels)	Field of view with 1024 by 1024 CCD (nm)
300,000	~3 pixels	61nm by 61nm
400,000	~5 pixels	47nm by 47nm
500,000	~6 pixels	37nm by 37nm
600,000	~7 pixels	31nm by 31nm
800,000	~10 pixels	24nm by24nm
1,000,000	~11 pixels	19nm by 19nm

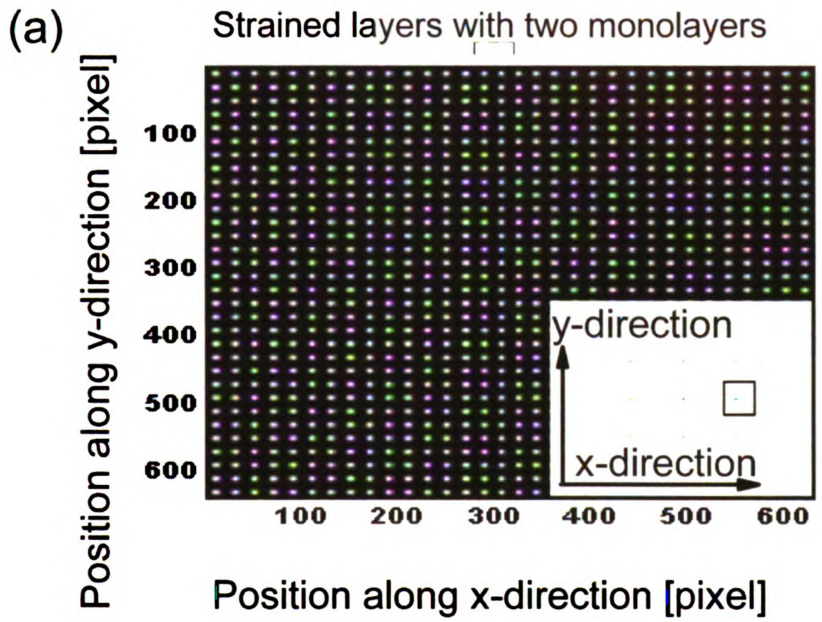

Figure 9.6: (a) A computer-generated 2D lattice using Matlab software. Arrows indicate coordinate system of x and y axes. A digital diffractogram is shown at inset. Rectangular region indicates the first harmonic required for strain analysis along x-direction. (b) Bragg- filtered lattice fringe using a g/3 Gaussian mask centered on the first harmonic. (c) An unwrapped phase image by removing phase jump from $-\pi$ to π. Notable change in phase at strained layers indicates displacement at strained layers.

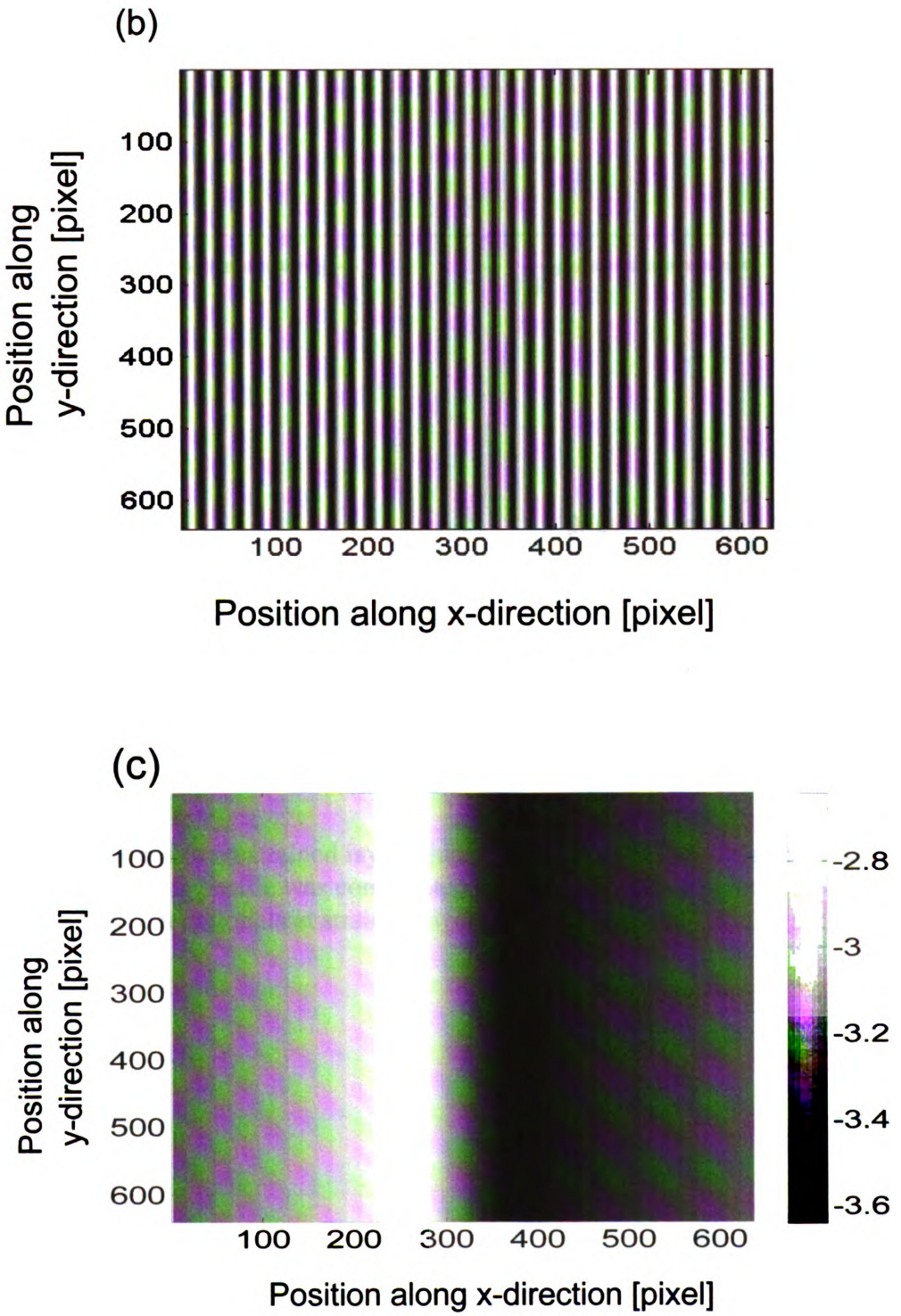

Figure 9.6: Continued.

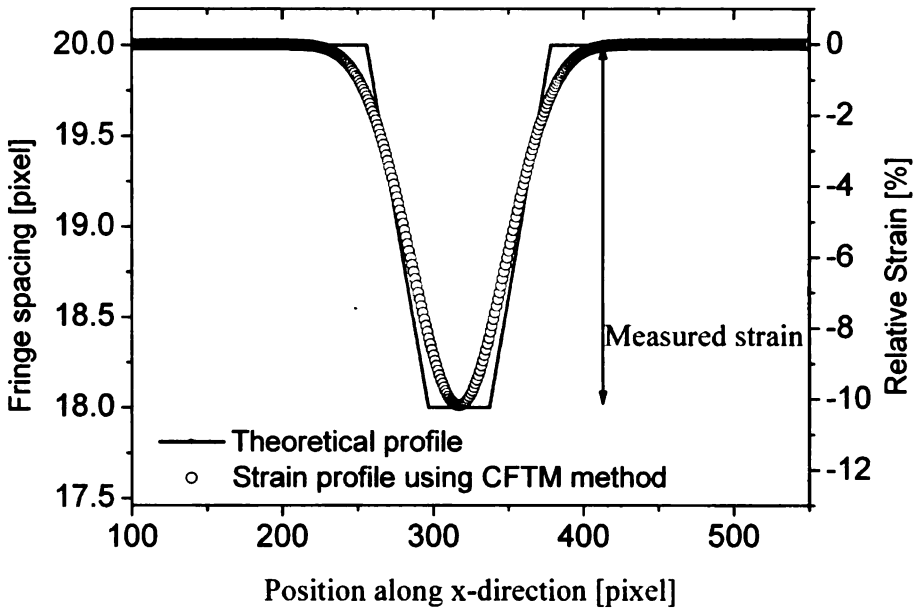

Figure 9.7: Strain profile on strained layers that is composed of 2 monolayers. An askance step profile was constructed for simulations, considering diffusion of constituent materials at strained layers.

9.3.2 Error quantification of the phase technique

Figure 9.8 shows a result of simulations where two parameters are -4% (a value of applied strain at strained layers with respect to reference regions on a 2D lattice image) and 7 pixels per lattice fringe spacing (image resolution). Each e_{xx} profile was plotted with different radius of a Gaussian mask and the mask size was varied up to g/2 for a Gaussian mask. Undershoot is observed due to the leakage effect similar to Figure 9.3 (a). In other words, linear dependence of error due to spurious high frequency noise from the leakage effect on mask size occurs. This results in measured strains of -7.03% and -9.33% at g/3 and g/2 Gaussian mask sizes, having errors of 76% and 133%, respectively.

The measured strain according to the mask size (Gaussian radius) is simulated using 2D lattice image (See Figure 9.6), where a strained value at strained layers is -4%, and shown in Figure 9.9. The result is similar to previous simulations using 1D lattice image as shown in Figure 9.3 (a). The simulation results shown in Figure 9.9 demonstrate again that error due to leakage effect can be notably reduced with increasing image resolution of an original image. For example, the measured strain was -3.76 with a g/3 Gaussian mask in the case of image resolution of 12 pixels per fringe spacing while measured strain was -7.03 with a g/3 Gaussian mask in the case of image resolution of 7 pixels per fringe spacing. Therefore, we conclude that leakage effect causes undershoot at strained layers, implying that resolution (number of pixels per fringe spacing) has to be increased to minimize error for reliability of phase technique as shown in Figure 9.3 (a) and Figure 9.9.

Finally, error has been quantified in terms of two parameters: the strained value we applied in the middle of an original image and image resolution (number of pixels per

fringe spacing). Error quantification is shown in Figure 9.10 and summarized in Table 9.2 where the procedures of image simulations are described in Chapter 9.3.1. All strains were measured at a g/3 Gaussian mask. From Figure 9.10, error due to the leakage effect is apt to become worse with small strain and poor resolution of an original image as shown in Figure 9.10 (a), (b), and (c). The error can be minimized with increased fringe spacing. From Table 9.2, we concluded that the phase technique can be exploited to determine strain information with two monolayer accuracy and less than 25% error for the values bounded with the thick line in Table 9.2. In the case of outside regions of the bounded region of Table 9.2, values within 25% error and values exceeding 25% error were sporadically positioned.

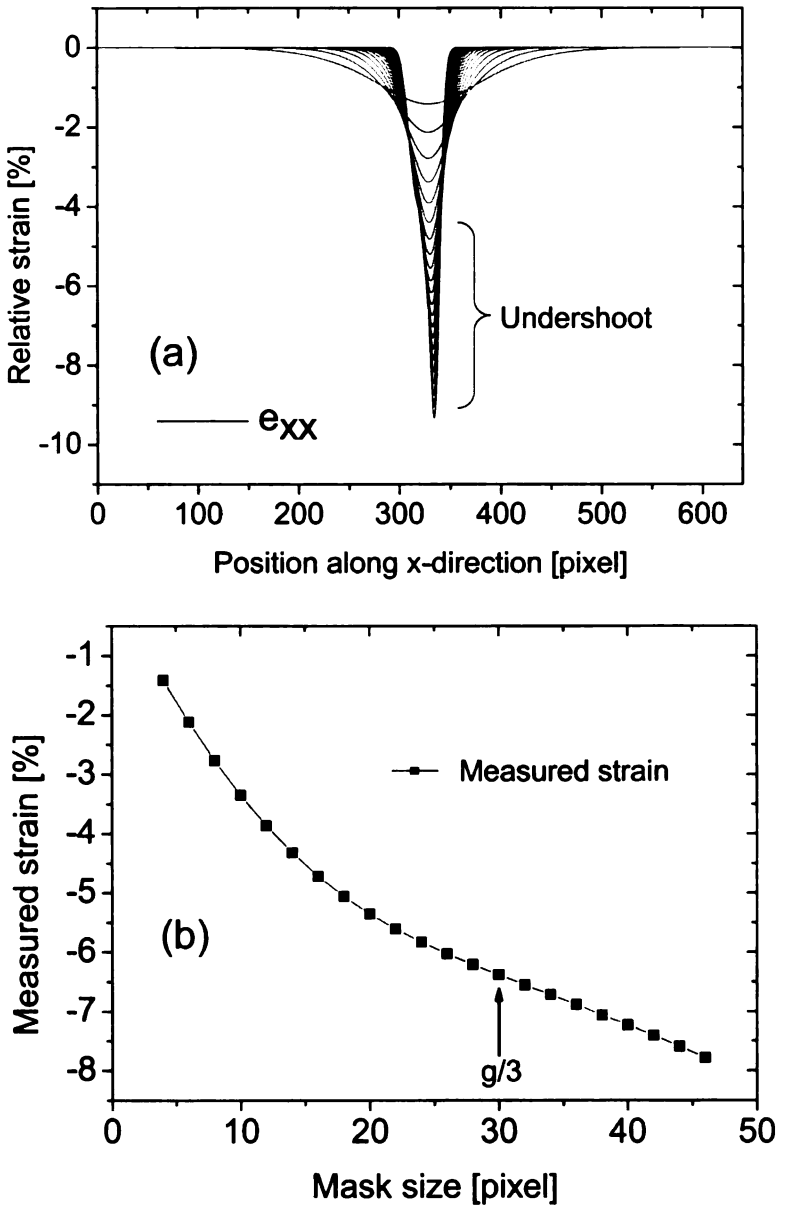

Figure 9.8: Strain profile on strained layers composed of two monolayers with 4% lattice contraction on strained layers. (a) Each profile was plotted with different size of a Gaussian function. Undershoot at strained layers becomes larger and larger with increasing mask size of a Gaussian function (b) Strain was measured with mask size of a Gaussian function where g/2 and g/3 correspond to 30 and 46 pixels respectively at x-axis.

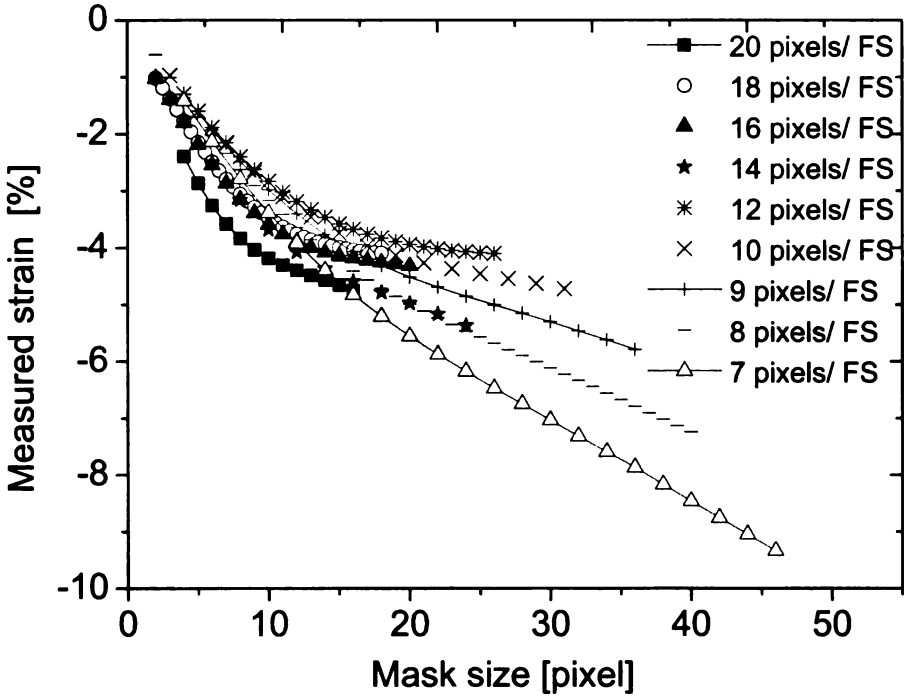

Figure 9.9: Measured strain in the case of -4% strain at strained layers we applied on an original image. Mask size (Gaussian radius) was varied from 4 pixels to g/2 for each resolution. Each graph represents resolution (number of pixels per fringe spacing) where FS represents fringe spacing in legend.

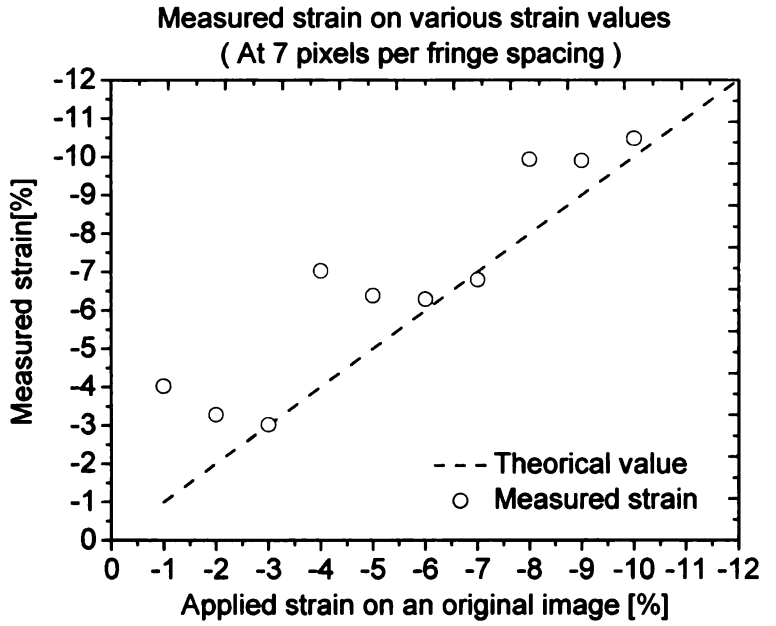

(a)

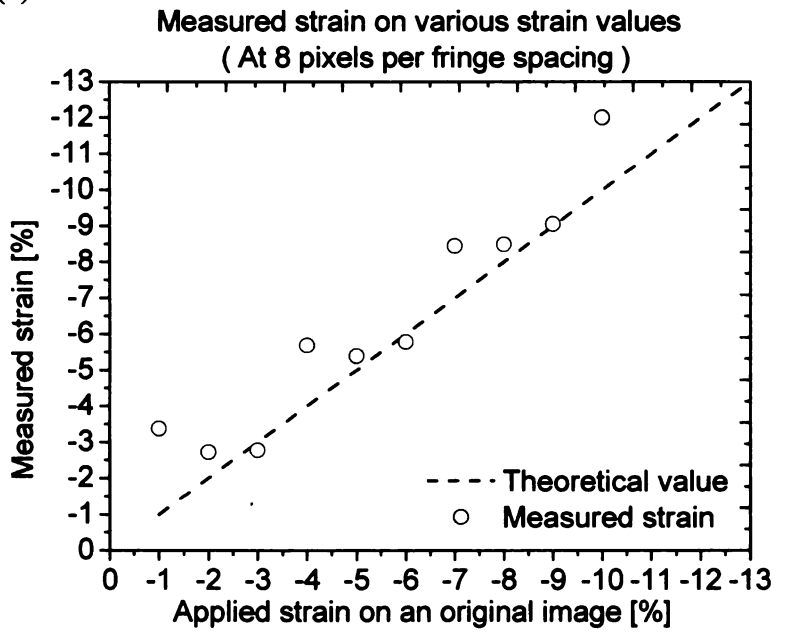

(b)

Figure 9.10: Measured strain with different image resolutions (number of fringe spacing) with given strain values at strained layers. Image resolutions of (a) 7 pixels of fringe spacing (b) 8 pixels of fringe spacing (c) 9 pixels of fringe spacing (d) 10 pixels of fringe spacing (e) 12 pixels of fringe spacing (f) 14 pixels of fringe spacing (g)16 pixels of fringe spacing (h) 18 pixels of fringe spacing (i) 20 pixels of fringe spacing

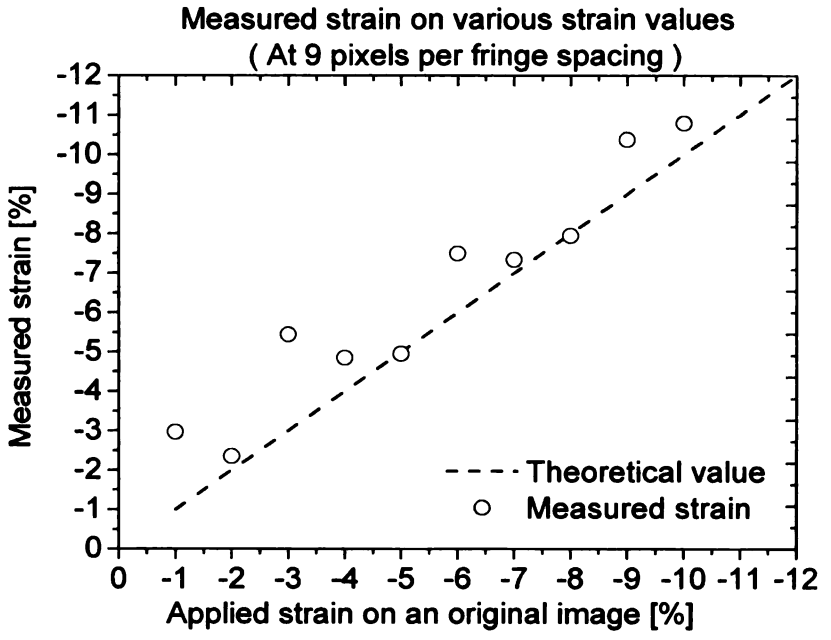

(c)

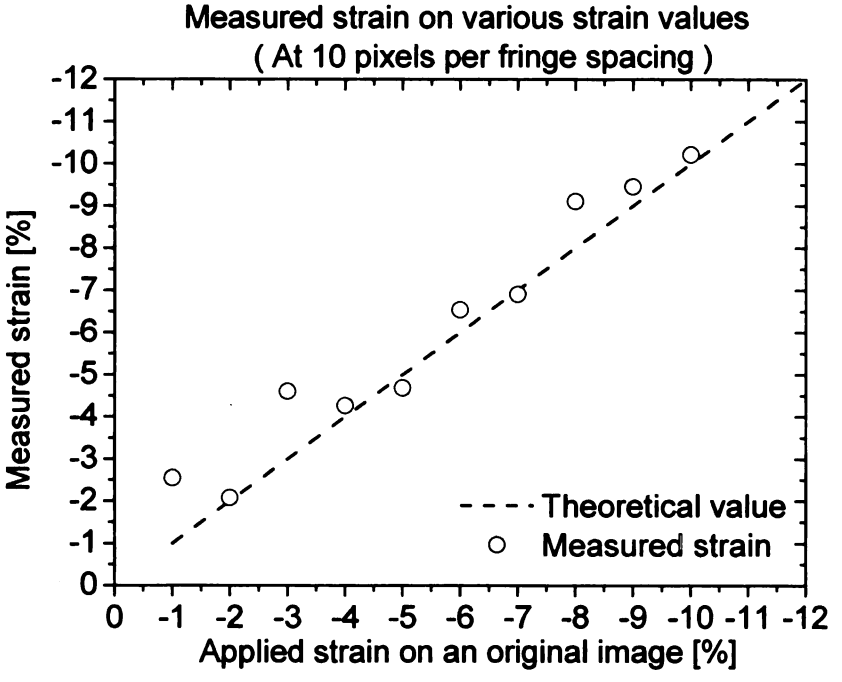

(d)

Figure 9.10: Continued.

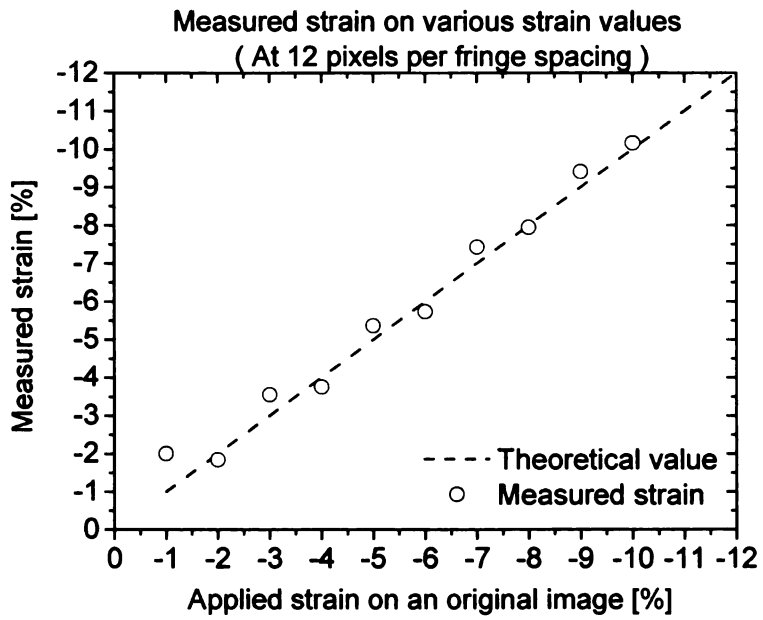

(e)

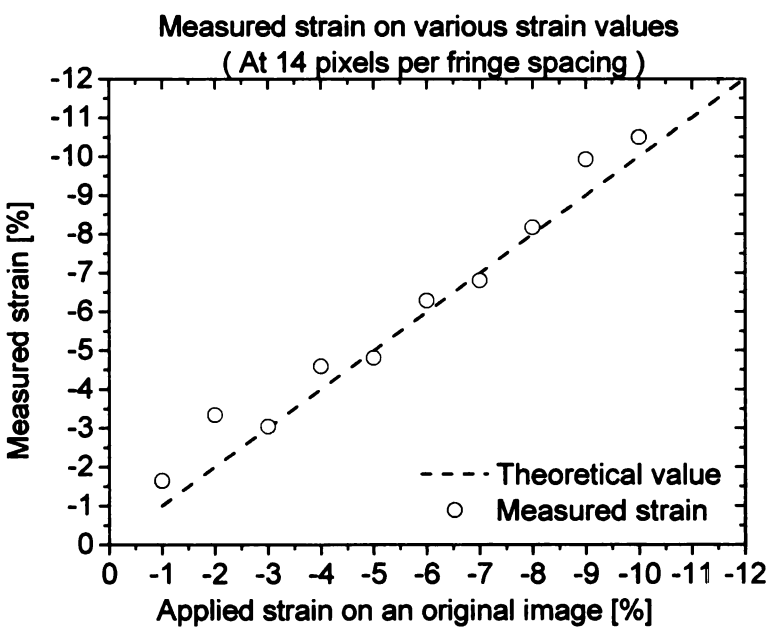

(f)

Figure 9.10: Continued.

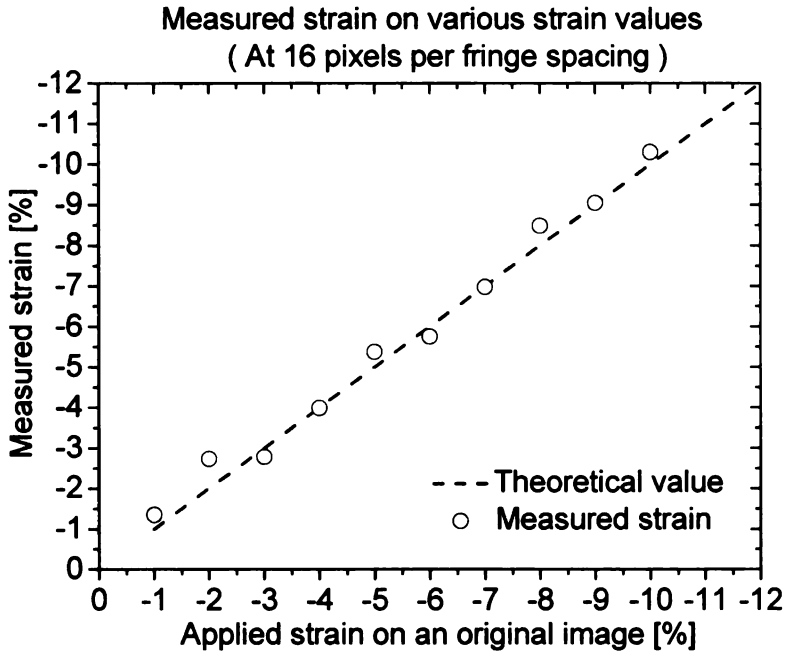

(g)

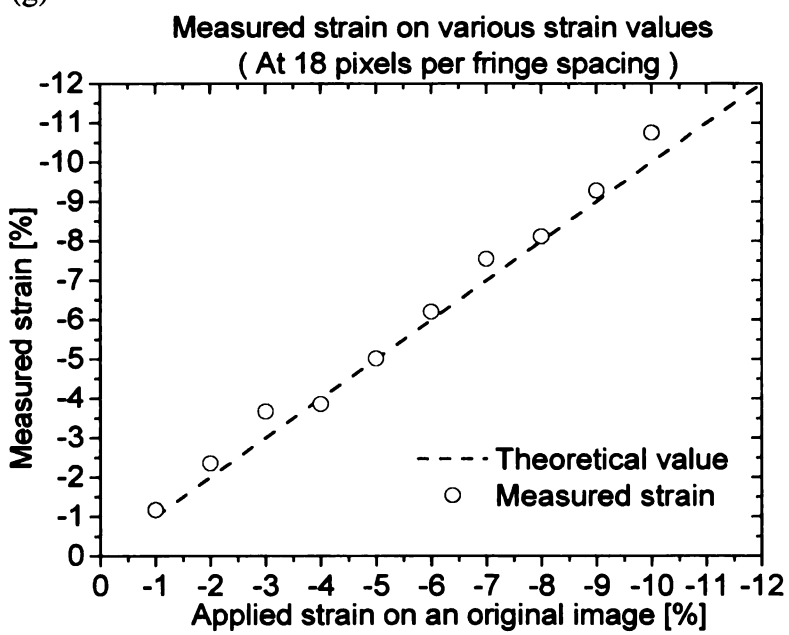

(h)

Figure 9.10: Continued.

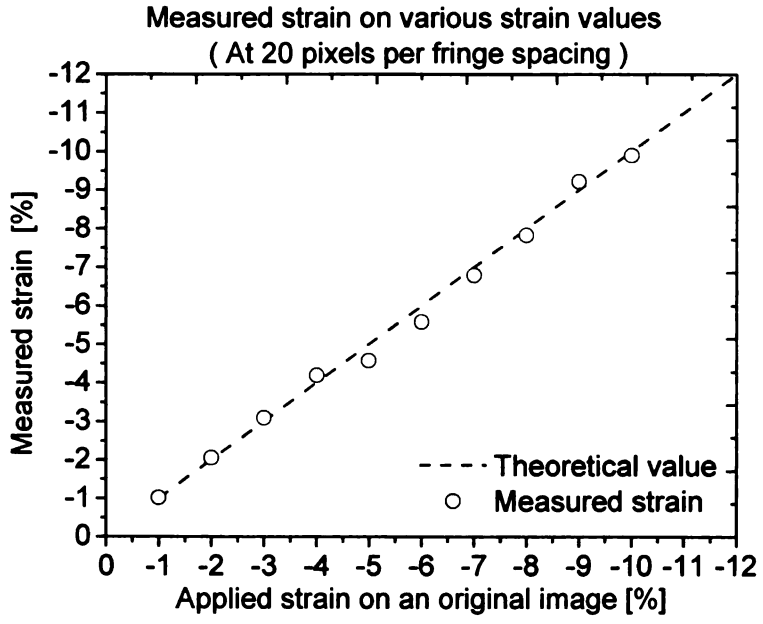

(i)

Figure 9.10: Continued.

Table 9.2: Measured strain at two monolayers of strained layers with g/3 Gaussian mask in terms of resolution (number of pixels per fringe spacing) and a strain value we applied on an original image. Error within 25% is bounded with thick line.

Given strain		Fringe Spacing [pixel]								
		7 pixels	8 pixels	9 pixels	10 Pixels	12 pixels	14 pixels	16 pixels	18 pixels	20 pixels
-1%	Strain	-4.02	-3.38	-2.97	-2.55	-2	-1.64	-1.35	-1.17	-1.02
	Error (%)	302	238	197	155	100	64	35	17	2
-2%	Strain	-3.28	-2.72	-2.35	-2.08	-1.84	-3.34	-2.73	-2.36	-2.05
	Error (%)	64	36	17.5	4	8	67	36.5	18	2.5
-3%	Strain	-3.02	-2.78	-5.44	-4.6	-3.55	-3.04	-2.78	-3.67	-3.09
	Error (%)	0.67	7.33	81.33	53.33	18.33	1.33	7.33	22.33	3
-4%	Strain	-7.03	-5.68	-4.85	-4.26	-3.76	-4.59	-3.99	-3.86	-4.19
	Error (%)	75.75	42	21.25	6.5	6	14.76	0.25	3.5	4.75
-5%	Strain	-6.38	-5.39	-4.95	-4.68	-5.36	-4.81	-5.37	-5.02	-4.57
	Error (%)	27.6	7.8	1	6.4	7.2	3.8	7.4	0.4	8.6
-6%	Strain	-6.29	-5.78	-7.5	-6.54	-5.73	-6.29	-5.75	-6.21	-5.58
	Error (%)	4.83	3.67	25	9	4.5	4.83	4.17	3.5	7
-7%	Strain	-6.8	-8.44	-7.34	-6.9	-7.43	-6.81	-6.97	-7.55	-6.79
	Error (%)	2.86	20.57	4.86	1.43	6.14	2.71	0.43	7.86	3
-8%	Strain	-9.93	-8.49	-7.95	-9.11	-7.95	-8.17	-8.48	-8.12	-7.83
	Error (%)	24.13	6.13	0.63	13.88	0.63	2.13	6	1.5	2.13
-9%	Strain	-9.9	-9.05	-10.38	-9.46	-9.41	-9.93	-9.05	-9.28	-9.22
	Error (%)	10	0.56	15.33	5.11	4.56	10.33	0.56	3.11	2.44
-10%	Strain	-10.47	-12	-10.79	-10.22	-10.16	-10.5	-10.3	-10.75	-9.9
	Error (%)	4.7	20	7.9	2.2	1.6	5	3	7.5	1

CHAPTER 10

COMPOSITION EVALUATION BY LATTICE FRINGE ANALYSIS (CELFA)

High-Resolution Transmission Electron Microscopy (HRTEM) involves the interference of the unscattered and scattered beams and does not use the objective aperture to obtain high resolution. These images usually have little contrast compared to dark or bright field images. However, the Composition Evaluation by Lattice Fringe Analysis (CELFA) method is a composition evaluation procedure based upon a chemically sensitive beam. For example, the (002) beam is the chemically sensitive beam for zincblende structures. The chemically sensitive beam depends strongly on the chemical composition. Hence, it is well suited for composition analysis and DALI software [53] provides measurement of chemical composition based on amplitude of the HRTEM images taken with the procedures for the CELFA method. In order to use the CELFA method, HRTEM images should be formed using two-beam or three-beam conditions [53], which generate a lattice fringe image on the HRTEM image. Hence, it is called Composition Evaluation by Lattice Fringe Analysis (CELFA) method.

However, accurate strain information on HRTEM images, especially at heterointerfaces, is also suggested by the CELFA method. The reason is that HRTEM images include artifacts influencing the positions of the atom columns in the HRTEM images. The artifacts are mainly caused by delocalization [53] and the composition

dependence of the phases of the beams contributing to the image formation. When a microscope is not equipped with Cs-corrector, the delocalization effect and chemical shift of the phases are minimized using the (002) and (000) beams and a strong excitation of the (004) beam [53], where the (002) beam is centered to the optical axis and the objective aperture is centered around the (000) and the (002) beams. The reason that the (002) beam is centered at the optical axis is to minimize aberrations and astigmatism. This is called a two-beam centered dark-field (CDF) image when two-beam conditions are used, and one diffracted beam such as the (002) beam is centered to the optical axis. The image with these two beams (*i.e.* (000) and (002) beams) interfering does not include artifacts from a microscope such as delocalization and chemical shift, the lattice fringe image will accurately correspond to the atomic columns in the crystalline specimen, resulting in accurate determination of strain information. The accurate determination of stain information using the CELFA method provides accurate composition evaluation using DALI software. Details about optimized imaging conditions to minimize artifacts from a microscope are discussed on Ref. [53].

However, the procedure of the CELFA method mentioned above is not very simple. Firstly, the specimen should be tilted from ZA to make systematic row condition, which shows only (00n) beams at selected area diffraction pattern. Secondly, the specimen should be tilted again to make two-beam conditions to obtain good diffraction contrast, where two-beam conditions is that only one diffracted beam and the (000) central beam are strong. In this case of the CELFA method, the (002) chemical sensitive beam is used for one diffracted beam in the case of the zincblende structure. Thirdly, the specimen should be titled again to obtain a non-zero deviation parameter, **S**, producing a strong

excitation of (004) beam as well as the (000) and (002) beams. This is shown in Fig. 10.1 with the $GaAs_{0.86}P_{0.14}$/GaAs superlattice. The **S** is a vector and a measure of how far we deviate from the exact Bragg condition. The value of **S,** amount of deviation from the exact Bragg condition, is different in different material systems. Rosenauer *et al.* [53] provides the value, **S,** because they developed software to determine the best value of **S** for different material systems, and the software is not commercially released yet. Finally, the (002) beam is centered to the optical axis as shown in Fig. 10.2, and the objective aperture is centered around the (000) central beam and the (002) beam, resulting in chemical sensitivity and minimized-artifacts in the lattice fringe image as shown in Fig. 10.3 (c). Figure 10.3 (b) shows a low resolution image with the CELFA method, where the procedure of the CELFA method is described above. We can clearly see that the interface is clearer at Fig. 10.3 (b) than Fig. 8.1 (a) or energy-filtered TEM (EFTEM) shown in Figure 10.4. Figure 10.3 (c) shows a high resolution image with CELFA method, which shows chemical lattice fringe at heterointerface of the $GaAs_{0.86}P_{0.14}$/GaAs superlattice due to the (002) chemical sensitive beams. As shown in Figure 10.3 (c), we can see that the number of monolayers of $GaAs_{0.86}P_{0.14}$ is around 2~3 with bright contrast.

In order to compare chemical contrast at the interface, energy-filtered TEM (EFTEM) was performed, and it is shown in Figure 10.4. Figure 10.4 shows a relatively rough surface with bright contrast compared to the CELFA image; however, it is evident from Figure 10.4 that phosphorus is mainly incorporated at the interface that is similar to

Figure 10.3 (c). To sum up, the CELFA image shown in Fig. 10.3 (c) shows clearer and sharper chemical contrast at the interface compared to energy-filtered TEM (EFTEM).

However, in practice, the $GaAs_{0.86}P_{0.14}$/GaAs heterostructure is not well suited for the CELFA method to determine strain information at the $GaAs_{0.86}P_{0.14}$layers because the lattice fringe is not clear. Hence, more work is needed to determine strain information at the $GaAs_{0.86}P_{0.14}$/GaAs heterostructure when the CELFA method is applied. If we can obtain nice and high-resolution images with the CELFA method, we can apply the phase technique on the image also for strain analysis, thus it will be valuable to compare results from the phase technique with results from the DALI software, since the DALI software also provides strain analysis on HRTEM images. Finally, the structure factor of $GaAs_{1-x}P_x$ was calculated at Appendix D.

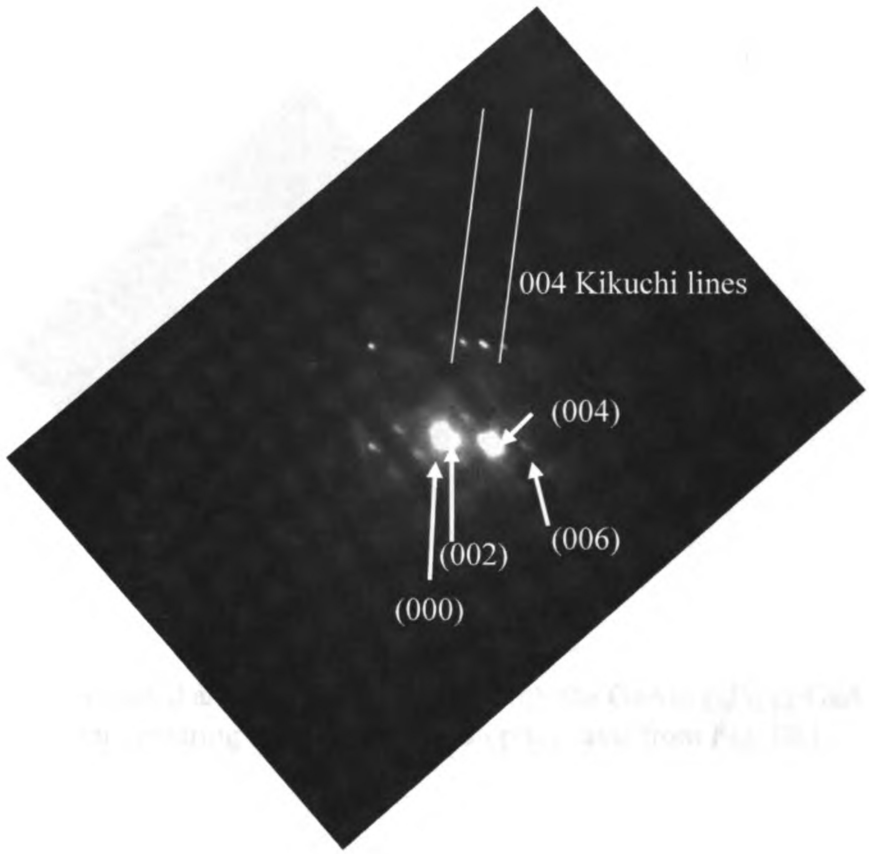

Figure 10.1: Selected area diffraction pattern with the $GaAs_{0.86}P_{0.14}$/GaAs superlattice, showing only (000), (002), (004) beams are strong.

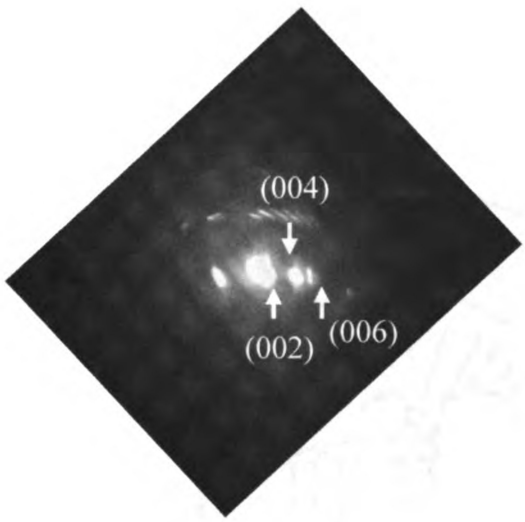

Figure 10.2: Selected area diffraction pattern with the $GaAs_{0.86}P_{0.14}$/GaAs superlattice after centering the (002) beam to optical axis from Fig. 10.1.

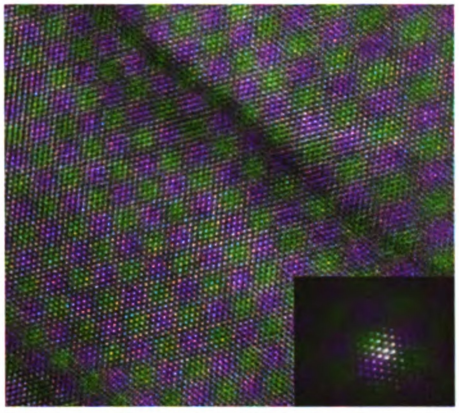

(a)

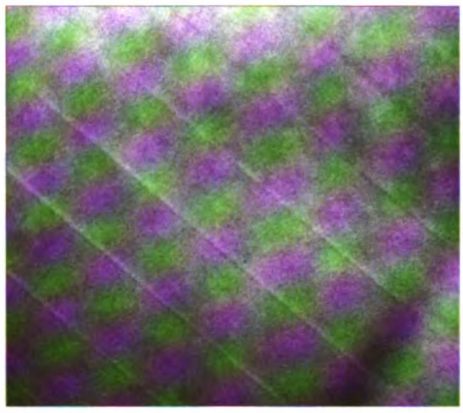

(b)

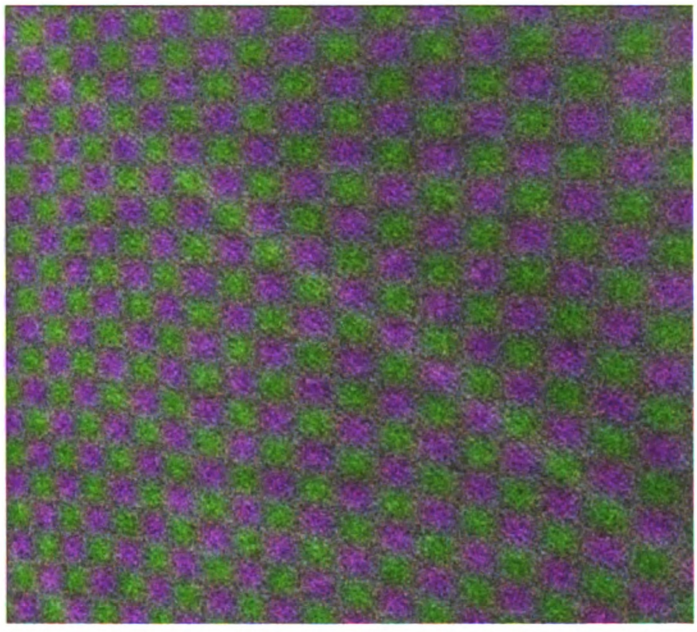

(c)

Figure 10.3: (a) A HRTEM image of the $GaAs_{0.86}P_{0.14}/GaAs$ superlattice. Inset shows symmetric SAD pattern for HRTEM imaging. (b) A low resolution image with procedures of CELFA method. (c) A High resolution image with procedures of CELFA method, showing lattice fringe.

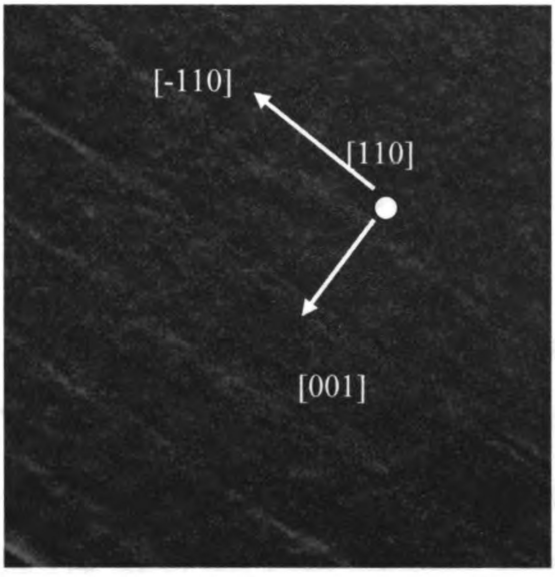

Figure 10.4: Elemental (phosphorus) map of the 5-period superlattice using energy-filtered TEM (EFTEM).

CHAPTER 11

SUMMARY AND DISCUSSTION

The primary research focus was strain analysis on heterointerfaces using the phase techniques such as the GPA and the CFTM method. The CFTM method, developed on solder ball connect (SBC) assemblies was not previously demonstrated on HRTEM images. Here we demonstrated the use of the CFTM method for strain analysis of ultra-thin layers from HRTEM images.

The advantage of the CFTM method with respect to the GPA method is that the CFTM method requires less memory for computation than that of the GPA method. The computational advantage is due to the fact that the CFTM method does not require a phase unwrapping process to remove discontinuities. The unwrapping process involves line-by-line scanning of the phase image to detect discontinuities; a process that requires considerable memory for computation. Moreover, the unwrapping algorithm depends on the configuration of the phase fringes in the phase image. The process becomes very complex if the phase fringes have a winding or irregular form. Therefore, the primary advantage of the CFTM method is that it does not require the unwrapping process.

Strain using the phase technique has been performed on ultra-thin layers of GaAsP on GaAs and the experimental results are introduced in Chapter 8. Our results revealed that error, linearly dependent on mask size, exists in the HRTEM image. This error appears to

be caused primarily by the leakage effect at strained layers. We demonstrated that the leakage effect dominates for small-strained systems (f<3%) with an image resolution of 7 pixels per fringe spacing, using computer-generated images. The image simulation results were introduced in Chapter 9. Therefore, the resolution (number of pixels per fringe spacing) of the HRTEM image must be improved in order to remove the leakage effect from the $GaAs_{0.86}P_{0.14}$ strained layers, regardless of quality of the HRTEM image. Alternatively, we can reduce the mask size used to filter out spurious high frequency terms due to the leakage effect at the cost of spectral resolution.

The leakage effect could be the principle limitation for interpreting strain using the phase technique, where lattice constant abruptly changes such as at heterointerfaces or a few monolayers. When the leakage effect exists at an interface with a few strained monolayers and higher resolution (larger number of pixels per fringe spacing) HRTEM images are not available, then mask-size optimization provides an alternative way.

Our initial estimate of an experimental strain analysis using g/3 mask size of a Gaussian mask revealed that the measured strain was around five times larger than the theoretical value. However, based on mask-size optimization, we determined that a quantitative value of measured strain at the $GaAs_{0.86}P_{0.14}$ /GaAs heterointerfaces would be -1.5%. The calculated value (-1.5%) was reached by eliminating error from the phase technique. Since the phase techniques such as GPA and CFTM methods do not rely on knowledge of the positions of atomic columns in the crystalline specimen, accuracy between the calculated value (-1.5%) and actual strain at the $GaAs_{0.86}P_{0.14}$ /GaAs

heterointerfaces depends on quality of HRTEM imaging. The suggestions to minimize artifacts from a microscope were summarized in Chapter 7.4.

A simulation method using Matlab® for determining error of the strain values when the phase technique is applied has been proposed, and the error of the phase technique was quantified for reliability of the phase technique with monolayer accuracy at Chapter 9.3. The image size of 2D lattice images generated with Matlab® are maintained at 620 by 620 pixels, and two monolayers of strained layers are placed in the middle of the 2D lattice images. Two parameters were applied to the 2D lattice images for image simulations. One is a value of strain at the strained layers and the other is the image resolution of the original image. We observed that a Gaussian mask in reciprocal space can remove the rippled appearance at the reference region with a computer-generated image, and error due to the leakage effect is apt to become worse with small strain and poor image resolution of an original image. The error was quantified with g/3 mask size of a Gaussian function in terms of two parameters in this research: a value of strain at strained layers and image resolution. Based on image simulations, we concluded that the phase technique can be exploited to determine strain information with monolayer accuracy within 25% error and this region is bounded with a thick line in Table 9.2.

Efforts to minimize artifacts from a microscope and chemical contrast were investigated using the CELFA method. Chemical contrast was compared with energy-filtered TEM. Two or three layers of $GaAs_{0.86}P_{0.14}$ with bright contrast were identified using CELFA method. However, in practice, the $GaAs_{0.86}P_{0.14}$ /GaAs superlattice is not well suited for CELFA method to determine strain information at $GaAs_{0.86}P_{0.14}$ layers

because the lattice fringe is not clear. If nice and high-resolution images with CELFA method can be obtained, we can apply the phase technique. Thus comparison of results for strain analysis between the phase technique and DALI software could be future research work.

APPENDIX A

MATLAB CODE OF AN EXPERIMENTAL IMAGE

```
close all
clear all

im=imread ('HR600K.tif'); % Loading of image
[sz1 sz2 sz3]=size(im);

%Original image
figure(1);colormap(gray(256));imagesc(im); axis image

%Rotation of image to exactly align growth and interface direction to x-and y- direction
ro=imrotate(im,-52.3);

%Rotated image of the original image
figure(2); colormap(gray(256));imagesc(ro);axis image

%Crop of original image
a2=ro(689:796,543:1192);
a2=a2(1:108,1:650);
%Display cropped image for original image
figure(3); colormap(gray(256));imagesc(a2);axis image

a2=double(a2);
[M,N]=size(a2);

%Fourier transform of an original image
fi1=fftshift(fft2(a2));
a3=fftshift(abs(fft2(a2)));
% Display of digital diffractogram of an original image
figure(4);
imagesc(log(a3));

% Length of (002) reciprocal vector
shiftu=94;

%Define mask function
```

```
[x y]=meshgrid(-N/2:N/2-1,-M/2:M/2-1);
y=flipud(y);
maska=zeros(M,N);
maskb=zeros(M,N);

%Meshgrid for mask function
[X,Y]=meshgrid(1:N,1:M);

for radius=90:1:90 %For loop for different mask sizes, radius=mask size

% Define mask function
a=4*pi;
maska=exp(-a*((X- ((N/2+1)+shiftu) ).^2+(Y-(M/2+1)).^2)/(radius^2));
maskb=exp(-a*((X- ((N/2+1)-shiftu) ).^2+(Y-(M/2+1)).^2)/(radius^2));

%Display of Gaussian mask function
figure(5);
subplot(1,2,1);imagesc(maska); title(' maska (002)');
subplot(1,2,2);imagesc(maskb); title(' maskb (00-2)');axis tight;

ufi_1=maska.*fi1;
ufi_2=maskb.*fi1;

g=abs(ufi_1);
h=abs(ufi_2);

%Display selected positive and negative harmonics
figure(6);
subplot(1,2,1);imagesc(g); title('FFT shift U');
subplot(1,2,2);imagesc(h);title('FFT shift -U');

ufi2_1=zeros(size(a2));
ufi2_1=ufi_1;
ufi2_2=zeros(size(a2));
ufi2_2=ufi_2;
dofr=ufi2_1+ufi2_2;

%Lattice Fringe image
cc=real(ifft2(fftshift(ufi2_1)));
layer_02=real(ifft2(fftshift(dofr)));

% Shifting (002) reflection to origin
ufi3=circshift(ufi_1, [0, -94]);


uf_1=ifft2(fftshift(ufi3)); % Conventional Moire Fringe
```

```
[M,N]=size(uf_1);

%Phase map
u=-angle(uf_1);

%Unwrapping process
WU=zeros (size(uf_1));

 for i=1:10
 for  j=2:N
if u(i,j)-u(i,j-1)<-pi
      WU (i,j)=WU (i,j-1)+1;
  else
       WU (i,j)=WU (i,j-1);
  if u(i,j)-u(i,j-1)>pi
     WU (i,j)=WU (i,j-1)-1;
  else
       WU (i,j)=WU (i,j-1);
  end

  end

end
 end

 for j=1:10
 for  i=11:M
if u(i,j)-u(i-1,j)<-pi
      WU (i,j)=WU (i-1,j)+1;
  else
       WU (i,j)=WU (i-1,j);
  if u(i,j)-u(i-1,j)>pi
     WU (i,j)=WU (i-1,j)-1;
  else
       WU (i,j)=WU (i-1,j);
  end

  end

 end
 end


for i=11:M
for j=10+1:N
```

```
  if u(i,j)-u(i,j-1)<-pi
     WU (i,j)=WU (i,j-1)+1;
  else
      WU (i,j)=WU (i,j-1);
  if u(i,j)-u(i,j-1)>pi
     WU (i,j)=WU (i,j-1)-1;
  else
      WU (i,j)=WU (i,j-1);
  end

  end

end
end

 unwrap_u=u+WU*2*pi;

 % Strain using numerical derivative
fx33=(6.91/(2*pi))*(1/6)* [-1,0,1; -1,0,1; -1,0,1];
fx3number_u=conv2(u,fx33);
fx3number_unu=conv2(unwrap_u,fx33);

% Covstrain3: strain using numerical derivative on phase image
Covstrain3=-1*fx3number_u';

% Covstrain3unwrap: strain using numerical derivative on unwrapped phase image
Covstrain3unwrap(:,:,radius)=-1*fx3number_unu';

 % Display phase image
figure(7);
imagesc(u); xlabel('Position along x-direction [pixel]');ylabel(' Position along x-direction
[Pixel]'); colorbar
% Display unwrapped phase image
figure(8);
imagesc(unwrap_u); xlabel('Position along x-direction [pixel]');ylabel(' Position along x-
direction [Pixel]'); colorbar

[k1,k2]=meshgrid(-N/2:N/2-1,-M/2:M/2-1);
k2=-k2;

%Strain using CFTM method
dudx(:,:,radius)=real(ifft2(fftshift(ufi3.*k1/N))./(-shiftu/N*uf_1));

end
```

APPENDIX B

MATLAB CODE OF IMAGE SIMULATIONS

```
clear all
close all

 % For loop for different mask sizes, B=mask size
for B=4:10:64

 % PITCHES AT REFERENCE REGIONS [Unit:pixel]
%p0=Pitch along y-direction, q0=Pitch along x-direction,
%m0=Number of periods along y-direction,  n0=Number of periods along x-direction
p0=20; q0=20;
m0=32; n0=15;

 % Define sinusodal function at reference regions
[x,y]=meshgrid(0:q0*n0-1,0:p0*m0-1);
r=4;
f0=zeros(size(x));  % x: size: 320 by 160
f0=sin(2*pi/q0*x).^r.*sin(2*pi/p0*y).^r;

 % PITCHES AT STRAINED REGIONS (2 MONO LAYERS) [Unit:pixel]
%p3=Pitch along y-direction, q3=Pitch along x-direction,
%m3=Number of periods along y-direction,  n3=Number of periods along x-direction
p3=20; q3=18; % In this example, 10% lattice contraction is applied.
m3=32; n3= 2;

% Define sinusodal function at reference regions
[x,y]=meshgrid(0:q3*n3-1,0:p3*m3-1);
d0=zeros(size(x)); % x: size: 320 by 34
d0=sin(2*pi/q3*x).^r.*sin(2*pi/p3*y).^r;

 % Combine reference regions with strained layers in one image.
g=[f0 d0 f0];
f=g(:,1:end);
 [M N]=size(f);

 % An Original image
 figure(1);
```

```
imagesc(f);axis image; colormap gray

 % Digital diffractogram of the image "f"
fi1=fftshift(fft2(f));
a3=fftshift(abs(fft2(f)));
figure(2);
imagesc(a3);
 [z1,z2]=meshgrid(-N/2:N/2-1,-M/2:M/2-1);
z2=-z2;
 ff=fft2(f);
aff1=abs(ff(1,:));

 %Find out lenght of a reciprocal vector of the first harmonic.
peaku1=find(aff1(1:round(end/2))==max(aff1(2:end)));
peaku=peaku1-1;
peak_u1=-1*peaku1;
peak_u=peak_u1+1;

 % Function of Computational Fourier Transform Moire (CFTM)
[u,unwarp_u,dudx,ufi_1,ufi_2,dofr,ufi2_1,cc,layer_02,k1,k2,fi1,ufi3]=cftm_Gau(B,f,pea
ku,peak_u);
 g=abs(ufi_1); % Diffractogram showing only positive first harmonic using an mask
h=abs(ufi_2); % Diffractogram showing only negative first harmonic using an mask
figure(3);
subplot(1,2,1);colormap(gray(256));imshow(g)
subplot(1,2,2);colormap(gray(256));imshow(h)
 figure(4);
imshow(abs(dofr)); % Diffractogram for Bragg-filtered lattice fringe
 figure(5);
imshow(log(abs(ufi3))); % Diffractogram for CFTM method
 figure(6); %Strain mapping using contour function
[C,h] = contour(k1,k2,dudx);
clabel(C,h);title('dudx');colorbar
 dudxmasksize(:,B)=dudx(M/2+7,:);
dudxmasksize_B=dudxmasksize';

 %Plot strain using CFTM method
figure(7);plot(dudx(M/2+7,:),'.-'); xlabel('Pixel');ylabel('du/dx (Strain) ');title('Strain
profile');axis tight;grid on;axis([1 643 -0.15 0.1 ]);
end
```

APPENDIX C

MATLAB CODE OF CFTM FUNCTION USED FOR IMAGE SIMULATIONS

```
function
[u,unwarp_u,dudx,ufi_1,ufi_2,dofr,ufi2_1,cc,layer_02,k1,k2,fi1,ufi3]=cftm_Gau(B,f,pea
ku,peak_u)

[M N]=size(f);

% Fourier transform of an original image (Digital diffractogram)
fi1=fftshift(fft2(f));
radius=B; %Mask radius

[X,Y]=meshgrid(1:N,1:M);
% Define Gausian mask function
% maska=> Mask function for positive harmonic
% maskb=> Mask function for negative harmonic
a=4*pi;
maska=exp(-a*((X- ((N/2+1)+peaku) ).^2+(Y-(M/2+1)).^2)/(radius^2));
maskb=exp(-a*((X- ((N/2+1)+peak_u) ).^2+(Y-(M/2+1)).^2)/(radius^2));

% Selecting the first harmonic using masks
ufi_1=maska.*fi1;
ufi_2=maskb.*fi1;

ufi2_1=zeros(size(f));
ufi2_1=ufi_1;

ufi2_2=zeros(size(f));
ufi2_2=ufi_2;

dofr=ufi2_1+ufi2_2;
cc=real(ifft2(fftshift(ufi2_1)));
layer_02=real(ifft2(fftshift(dofr)));
% Shifting the first harmonic to origin for CFTM method
ufi3=circshift(ufi_1,[0,peak_u]);

uf_1=ifft2(fftshift(ufi3)); % Conventional Moire Fringe
%Phase image
```

```
u=-angle(uf_1);
% Unwrapping algorithm on phase image
WU=zeros (size(f));

 for i=1:10
 for  j=2:N
if u(i,j)-u(i,j-1)<-pi
      WU (i,j)=WU (i,j-1)+1;
  else
       WU (i,j)=WU (i,j-1);
  if u(i,j)-u(i,j-1)>pi
     WU (i,j)=WU (i,j-1)-1;
  else
       WU (i,j)=WU (i,j-1);
  end

  end

end
 end

 for j=1:10
 for  i=11:M
if u(i,j)-u(i-1,j)<-pi
      WU (i,j)=WU (i-1,j)+1;
  else
       WU (i,j)=WU (i-1,j);
  if u(i,j)-u(i-1,j)>pi
     WU (i,j)=WU (i-1,j)-1;
  else
       WU (i,j)=WU (i-1,j);
  end

  end

 end
 end

 for i=11:M
for j=10+1:N
  if u(i,j)-u(i,j-1)<-pi
     WU (i,j)=WU (i,j-1)+1;
  else
       WU (i,j)=WU (i,j-1);
  if u(i,j)-u(i,j-1)>pi
     WU (i,j)=WU (i,j-1)-1;
```

```
  else
     WU (i,j)=WU (i,j-1);
  end

  end

end
end
 unwarp_u=u+WU*2*pi;

[k1,k2]=meshgrid(-N/2:N/2-1,-M/2:M/2-1);
k2=-k2;
 %Strain tensor of CFTM method
dudx=real(ifft2(fftshift(ufi3.*k1/N))./(-peaku/N*uf_1));
dudy=real(ifft2(fftshift(ufi3.*k2/M))./(-peaku/N*uf_1));
```

APPENDIX D

STRUCTURE FACTOR FOR GALLIUM ARSENIDE PHOSPHIDE

In the kinematical approximation, the amplitude of a diffracted beam $\mathbf{g}_{hkl}$ is proportional to structure factor. The structure factor is to consider a unit cell of a crystal containing N atoms with atomic scattering factors $f_e^{(i)}$ at positions r_i (i=1,.....N). The structure factor of a beam for a binary material GaAs, given by

$$F_{hkl} = 4\{f_e^{Ga} + f_e^{As} \exp(\frac{i\pi}{2}(h+k+l))\}. \quad \text{(D-1)}$$

In the case of a ternary material $GaAs_{1-x}P_x$, we assume a random d0istribution of As and P on the metal sublattice. The structure factor of the ternary material is then obtained to a good approximation by assuming, that the atomic scattering amplitude of the metal site is a linear combination of the scattering amplitudes of the two types of metal atoms under consideration:

$$F_{hkl} = 4\{f_e^{Ga} + (1-x)f_e^{As} \exp(\frac{i\pi}{2}(h+k+l)) + xf_e^{P} \exp(\frac{i\pi}{2}(h+k+l))\}. \quad \text{(D-2)}$$

structure factors of $GaAs_{1-x}P_x$ with major reflections are shown in Table D.1.

Table D.1: Structure factors of GaAs1-xPx with major reflections.

Structure factors	(100)	(110)	(200)
GaAs (F_{S_GaAs})	0	0	$4\{f_{Ga} - f_{As}\}$
GaAsP (F_{S_GaAsP})	0	0	$4\{f_{Ga} - (1-x)f_{As} - xf_P\}$
$I = \lvert F\rvert^2$	0	0	$16\{f_{Ga} - (1-x)f_{As} - xf_P\}^2$
X=0	0	0	$4\{f_{Ga} - f_{As}\}$
$\frac{F_{S(x)}}{F_{S(0)}}$	0	0	$\frac{f_{Ga} - f_{As} + (f_{As} - f_P)x}{f_{Ga} - f_{As}}$

Structure factors	(220)	(400)
GaAs (F_{S_GaAs})	$4\{f_{Ga} + f_{As}\}$	$4\{f_{Ga} + f_{As}\}$
GaAsP (F_{S_GaAsP})	$4\{f_{Ga} + (1-x)f_{As} + xf_P\}$	$4\{f_{Ga} + (1-x)f_{As} + xf_P\}$
$I = \lvert F\rvert^2$	$16\{f_{Ga} + (1-x)f_{As} + xf_P\}^2$	$16\{f_{Ga} + (1-x)f_{As} + xf_P\}^2$
X=0	$4\{f_{Ga} + f_{As}\}$	$4\{f_{Ga} + f_{As}\}$
$\frac{F_{S(x)}}{F_{S(0)}}$	$\frac{f_{Ga} + f_{As} + (f_P - f_{As})x}{f_{Ga} + f_{As}}$	$\frac{f_{Ga} + f_{As} + (f_P - f_{As})x}{f_{Ga} + f_{As}}$

LIST OF REFERENCES

[1] N.P. Ekins-Daukes, K.W.J. Bamham, J.P. Connolly, J.S. Roberts, J.C. Clark, G. Hill, and M. Mazzer, "Strain-balanced GaAsP/InGaAs quantum well solar cells," Appl. Phys. Lett., Vol. 75, No. 26, pp. 4195-4197, December, (1999).

[2] H.C. Choi, Y. Guo, W. Lafontaine, and C.K. Lim, "Soler Ball Connect (SBC) assemblies under thermal loading: II. Strain analysis via image processing, and reliability considerations," IBM J. Res. Dev., Vol. 37, No. 5, pp. 649-659, September, (1993).

[3] Optoelectronics and Photonics: Principles and practices, S.O. Kasap, Prentice Hall, Upper Saddle River, NJ, (2001).

[4] D. B. Eason, Z. Yu, W. C. Hughes, W. H. Roland, C. Boney, J. W. Cook, Jr., J. F. Schetzina, G. Cantwell, and W. C. Harsch, "High-brightness blue and green light-emitting diodes," Appl. Phys. Lett., Vol. 66 No. 2, pp. 115-117, January, (1995).

[5] R. W. Martin, P. R. Edwards, R. Pecharroman-Gallego, C. Liu, C. J. Deatcher, I. M. Watson, and K. P. O'Donnell, "Light emission ranging from blue to red from a series of InGaN/GaN single quantum wells," J. Phys. D: Appl. Phys., Vol. 35, pp. 604–608, (2002).

[6] H. Y. Ryu, K. H. Ha, S. N. Lee, T. Jang, J. K. Son, H. S. Paek, Y. J. Sung, H. K. Kim, K. S. Kim, O. H. Nam, Y. J. Park, and J. I. Shim, " High-Performance Blue InGaN Laser Diodes With Single-Quantum-Well Active Layers," IEEE Photonics Technology Letters, Vol. 19, No. 21, pp. 1717-1719, November, (2007).

[7] H. Amano, N. Sawaki, I. Akasaki, and Y. Toyoda, "Metalorganic vapor phase epitaxial growth of a high quality GaN film using an AlN buffer layer," Appl. Phys. Lett. , Vol. 48, pp. 353-355, February, (1986).

[8] S. Nakamura, "GaN Growth Using GaN Buffer Layer," J. Jpn. Appl. Phys., Vol. 30, pp. L1705-L1707, (1991).

[9] N. Yoshimoto, T. Matsuoka, T. Sasaki, and A. Katsui, "Photoluminescence of InGaN films grown at high temperature by metalorganic vapor phase Epitaxy," Appl. Phys. Lett., Vol. 59, pp. 2251-2253, October, (1991).

[10] S. Nakamura, T. Mukai, and M. Senoh, "Si-Doped InGaN Films Grown on GaN Films," Jpn. J. Appl. Phys., Vol. 32, pp. L16-L19, (1993).

[11] K. Itoh, K. Hiramatsu, H. Amano, and I. Akasaki, "PREPARATION OF $Al_XGa_{1-X}N$/GaN HETEROSTRUCTURE BY MOVPE," J. Cryst. Growth, Vol. 104, pp. 533-538, (1990).

[12] K. Itoh, T. Kawamoto, H. Amano, K. Hiranatsu, and I. Akasaki, "Metalorganic Vapor Phase Epitaxial Growth and Properties of GaN/$Al_{0.1}Ga_{0.9}$ N Layered Structures," Jpn. J. Appl. Phys., Vol. 30, pp. 1924-1927, (1991).

[13] S. Nakamura, T. Mukai, M. Senoh, S. Nagahama, and N. Iwasa, "$In_XGa_{(1-X)}/In_YGa_{(1-y)}N$ superlattices grown on GaN films," J. Appl. Phys., Vol. 74, pp. 3911-3915, September, (1993).

[14] M. Koike, S. Yamasaki, S. Nagai, N. Koide, S. Asami, H. Amano, and I. Akasaki, "High-quality GaInN/GaN multiple quantum wells," Appl. Phys. Lett., Vol. 68, pp. 1403-1405, March, (1996).

[15] Shuji Nakamura, " Zn-doped InGaN growth and InGaN/ AlGaN double-heterostructure blue-light-emitting diodes," Journal of Crystal Growth, Vol. 145, pp. 911-917, (1994).

[16] J. Xu, L. Chen, L. Yu, H. Liang, B.S. Zhang, and K. M. Lau, "Cathodoluminescence Study of InGaN/GaN Quantum-Well LED Structures Grown on a Si Substrate," Journal of Electronic Materials, Vol. 36, pp. 1144-1148, (2007).

[17] T. Xu, A. Y. Nikiforov, R. France, C. Thomidis, A. Williams, and T. D. Moustakas, "Blue–green–red LEDs based on InGaN quantum dots grown by plasma-assisted molecular beam Epitaxial," phys. stat. sol. (a), Vol. 204, pp. 2098–2102, (2007).

[18] R Armitage and K Tsubaki, "Multicolour luminescence from InGaN quantum wells grown over GaN nanowire arrays by molecular-beam Epitaxial," Nanotechnology, Vol. 21, pp. 195202.1-7, (2010).

[19] Y. L. Chang, J. L. Wang, F. Li, and Z. Mi, "High efficiency green, yellow, and amber emission from InGaN/GaN dot-in-a-wire heterostructures on Si (111)," Appl. Phys. Lett., Vol. 96, pp. 013106.1-3, (2010).

[20] S. Guha and N. A. Bojarczuk, " Ultraviolet and violet GaN light emitting diodes on silicon," Appl. Phys. Lett., Vol. 72, pp. 415-417, January, (1998).

[21] L. A. Reichertz, I. Gherasoiu, K. M. Yu, V. M. Kao, W. Walukiewicz, and J. W. Ager III, "Demonstration of a III–Nitride/Silicon Tandem Solar Cell," Applied Physics Express, Vol. 2, pp. 122202.1-3, (2009).

[22] S. S. Islam and A.F.M. Anwar, "High frequency GaN/AlGaN HEMT class-E power amplifier," Solid-State Electronics, Vol. 46, pp. 1621-1625, (2002).

[23] M. A. Khan, J. N. Kuznia, J. M. Van Hove, N. Pan, and J. Carter, " Observation of a two-dimensional electron gas in low pressure metal-organic chemical vapor deposited GaN-$Al_xGa_{1-x}N$-heterojunctions," Appl. Phys. Lett., Vol. 60, pp. 3027-3029, (1992).

[24] J. Schalwig, G. Muller, M. Eickhoff, O. Ambacher, and M. Stutzmann, " Gas sensitive GaN/AlGaN-heterostructures," Sensors and Acturator B, Vol. 87, pp. 425-430, (2002).

[25] M. Stutzmann, G. Steinhoff, M. Eickhoff, O. Ambacher, C. E. Nebel, J. Schalwig, R. Neuberger, and G. Muller, "GaN-based heterostructures for sensor applications", Diamond and Related Materials, Vol. 11, pp. 886-891, (2002).

[26] S. J. Pearton, B. S. Kang, S. Kim, F. Ren, B. P. Gila, C. R. Abernathy, J. Lin, and S. N. G. Chu, "GaN-based diodes and transistors for chemical, gas, biological and pressure sensing," Journal of Physics: Condensed Matter, Vol. 16, pp. R961-R994, (2004).

[27] K. Yano, T. Ishii, T. Hashimoto, T. Kobayashi, F. Murai, and K. Seki, "Room-Temperature Single-Electron Memory", IEEE Transactions on electron devices, Vol. 41, No.9, pp. 1628-1638, September (1994).

[28] S.J. Pearton, C.R. Abernathy, D.P. Norton, A. F. Hebard, Y. D. Park, L. A. Boatner, and J. D. Budai, "Advances in wide bandgap materials for semiconductor Spintronics," Materials Science and Engineering, Vol. R 40, pp. 137–168, (2003).

[29] Transmission Electron Microscopy, D. B. Williams and C. B. Carter, Plenum Press, New York, NY, (1996).

[30] M. D. Robertson, J. E. Currie, J. M. Corbett, and J. B. Webb, "Determination of elastic strains in epitaxial layers by HREM," Ultramicroscopy, Vol. 58, pp. 175-184, (1995).

[31] C.Quintana, D. Golmayo, M.L. Dotor, and M. Lancin, "Analysis of local deformations in heterostructures containing short period superlattices by high-resolution transmission electron microscopy," Eur. Phys. J. Appl. Phys., Vol. 25, pp. 159-168, (2004).

[32] R.E. Dunin-Borkowski and W. Michael Stobbs, "The determination of rigid lattice shifts across delta-doped layers using regressional analysis," Ultramicroscopy, Vol. 72, pp. 199-211, (1998).

[33] A. Ourmazd, D. W. Taylor, M. Bode, and Y. Kim, "Quantifying the Information Content of Lattice Images," Science, Vol. 246, pp. 1571-1577, December, (1989).

[34] C. Kisielowski, P. Schwander, F. H. Baumann, M. Seibt, Y. Kim, and A. Ourmazd, "An approach to quantitative high-resolution transmission electron microscopy of crystalline materials," Ultramicroscopy, Vol. 58, pp. 131-155 (1995).

[35] A. Rosenauer, T. Remmele, D. Gerthsen, K. Tillmann, and A. Forster, "Atomic scale strain measurements by the digital analysis of transmission electron microscopic lattice images," Optik, Vol. 105, pp. 99-107, (1997).

[36] A. Rosenauer, U. Fischer, D. Gerthsen, and F. Forster, "Composition evaluation of $In_XGa_{1-X}As$ Stranski-Krastanow-island structures by strain state analysis," Appl. Phys. Lett., Vol. 71, pp. 3868-3870, (1997).

[37] C.P. Liu, R.E. dunin-Borkowski, C.B. Boothroyd, P.D. Brown, and C.J. Humphreys, "Characterization of Ultrathin Doping Layers in Semiconductors," Microscopy and Microanalysis, Vol. 3, pp. 352-363, (1997).

[38] M. J. Hytch and M. Gandais, "Quantitative criteria for the detection and characterization of nanocrystals from high-resolution electron microscopy images," Philos. Mag. A, Vol. 72, pp. 619-634, (1996).

[39] Y. Morimoto, Y. Seguchi, and T. Higashi, "Strain analysis by mismatch moire method and grid method using Fouier transform," Comput. Mech., Vol. 6, pp. 1-10, (1990).

[40] M.J. Hytch, E. Snoeck, and R. Kilaas, "Quantitative measurement of displacement and strain fields from HREM micrographs," Ultramicroscopy, Vol. 74, pp. 131-146, (1998).

[41] M.J. Hytch, J. Putaux, and J. Penisson, "Measurement of the displacement field of dislocations to 0.03Å by electron microscopy," Nature, Vol. 423, pp. 270-273, May, (2003).

[42] A.M. Sanchez, J.G. Lozano, R. Garcia, M. Herrera, S.Ruffenach, O. Briot, and D. Gonzalez, "Strain Mapping at the Atomic Scale in Highly Mismatched Heterointerfaces," Adv. Funct. Mater., Vol. 17, pp. 2588-2593, (2007).

[43] S. Kret, P. Dluzewski, P. Dluzewski, and E. Sobczak, "Measurement of dislocation core distribution by digital processing of high-resolution transmission electron microscopy micrograph: a new technique for studying defects," J. Phys.-Condens. Mat., Vol. 12, pp. 10313-10318, (2000).

[44] S.L. Sahonta, G.P. Dimitrakopulos, Th. Kehagias, J. Kioseoglou, A. Adikimenakis, E. lliopoulos, A. Georgakilas, H. Kirmse, W. Neumann, and Ph. Komninou, "Mechanism

of compositional modulations in epitaxial InAlN films grown by molecular beam epitaxy," Appl. Phys. Lett., Vol. 95, pp. 021913.1-3, (2009).

[45] G. Ade, "Characterisation of layered heterostructures by means of HRTEM and digital image processing," Microelectron. Eng., Vol.51-52, pp. 3-9, (2000).

[46] E. Guerrero, P. Galindo, A. Yanez, T. Ben, and S. I. Molina, "Error Quantification in Strain Mapping Methods," Microsc. Microanal., Vol. 13, pp. 320-328, (2007).

[47] A. Delimitis, Ph. Komninou, G. P. Dimitrakopulos, Th. Kehagias, J. Kioseoglou, Th. Karakostas, and G. Nouet, "Strain distribution of thin InN epilayers grown on (0001) GaN templates by molecular beam epitaxy," Appl. Phys. Lett., Vol. 90, pp. 061920.1-3, (2007).

[48] M. J. Hytch, "Analysis of Variations in Structure from High Resolution Electron Microscope Images by Combining Real Space and Fourier Space Information," Microsc. Microanal. Microstruct., Vol. 8, pp. 41-57, February, (1997).

[49] A. M. Sanchez, P.L. Galindo, S. Kret, M. Falke, R. Beanland, and P.J. Goodhew, "Quantitative Strain Mapping Applied to Aberration Corrected HAADF Images," Microsc. Microanal., Vol. 12, pp. 285-294, (2006).

[50] E. Snoeck, B. Warot, H. Ardhuin, A. Rocher, M. J. Casanove, R. Kilaas, and M. J. Hytch, "Quantitative analysis of strain field in thin films from HRTEM micrographs," Thin Solid Films, Vol. 319, pp. 157-162, (1998).

[51] J. G. Lozano, A. M. Sanchez, R. Garcia, S. Ruffenach, O. Briot, and D. Gonzalez, "Strain Relief Analysis of InN Quantum Dots Grown on GaN," Nanoscale Res. Lett., Vol. 2, pp. 442-446, (2007).

[52] M. J. Hytch, "GEOMETRIC PHASE ANALYSIS OF HIGH RESOLUTION ELECTRON MICROSCOPE IMAGES," Scanning Microscopy, Vol. 11, pp. 53-66, (1997).

[53] A. Rosenauer, D. Gerthsen, and V. Potin, "Strain state analysis of InGaN/GaN-source of error and optimized imaging conditions," Phys. Stat. Sol. (a), Vol. 203, pp. 176-184 (2006).

[54] N. Tanaka, "Present status and future prospects of spherical aberration corrected TEM/STEM for study of nanomaterials," Sci. Technol. Adv. Mater., Vol. 9, pp. 014111.1-11, (2008).

[55] T. D. Brown and G. S. May, "Hybrid Neural Network Modeling of Anion Exchange at the Interfaces of Mixed Anion III-V Heterostructures Grown by Molecular Beam Epitaxy," IEEE Trans. Semiconductor Manufacturing, Vol. 18, pp. 614-621 (2005).

[56] M. D. Robertson, J. M. Corbett, J. B. Webb, J. Jagger, and J. E. Currie, "Elastic Strain Determination in Semiconductor Epitaxial Layers by HREM," Micron, Vol. 26, pp. 521-537, (1995).

[57] H. Aoyagi, H. Horinaka, Y. Kamiya, T. Kato, T. Kosugoh, S. Nakamura, T. Nakanishi, S. Okumi, T. Saka, M. Tawada, and M. Tsubata, "Strain dependence of spin polarization of photoelectrons from a thin GaAs layer," Phys. Lett. A, Vol. 167, pp. 415-420, (1992).

[58] http://www.ioffe.ru/SVA/NSM/Semicond/GaAs/mechanic.html (Last accessed August 2010).

[59] http://www.ioffe.ru/SVA/NSM/Semicond/GaP/mechanic.html (Last accessed August 2010).

[60] P. A. Stadelmann, "Ems-a Software Package for Electron-Diffraction Analysis and Hrem Image Simulation in Materials Science," Ultramicroscopy, Vol. 21, pp. 131-145, (1987).

[61] P. Specht, R.C. Lutz, R. Zhao, E.R. Weber, W.K. Liu, K. Bacher, F.J. Towner, T.R. Stewart, and M. Luysberg, "Improvement of molecular beam epitaxy-grown low-temperature GaAs through p doping with Be and C," J. Vac. Sci. Technol. B, Vol. 17, pp. 1200-1204, (1999).